Range Imaging Metrology:
Investigation, Calibration and Development

A dissertation submitted to the

ETH Zurich

for the degree of

Doctor of Sciences ETH Zurich

presented by

TIMO KAHLMANN

Dipl.-Ing., University of Hannover

Date of Birth May 22, 1977

citizen of

Germany

accepted on the recommendation of

Prof. Dr. Hilmar Ingensand, examiner
Prof. Dr. habil. Hans-Gerd Maas, co-examiner

2007

Abstract

In recent years, numerous sensor systems for the capturing of three-dimensional environments and objects have become available. Besides laser scanners and geodetic total stations, stereo vision and triangulation-based systems have to be exemplarily named here. Especially laser scanners have become state-of-the-art regarding speed and accuracy with respect to their ability to acquire objects up to a size of several tens of meters. A main drawback of laser scanners is their sequential mode of operation. They measure point by point. A few years ago, a new technology was developed to full functionality which is able to capture the environment simultaneously with a high resolution. So-called *range imaging* (RIM) or *flash ladar* cameras, which are based on digital imaging technology, merged with the ability to measure the distance to the corresponding object point in each pixel. Distance measurement is either based on the direct or indirect Time-of-Flight principle. Due to its parallel acquisition with up to video frame rate, RIM cameras are even able to capture moving objects. With respect to the optical dependencies, 3-D coordinates of the captured scene are derived. The nominal precision of the distance measurement is a few millimeters. RIM could become the technology of choice for many applications if the properties and characteristics become stable and predictable. Automotive, robotics, and safety systems can be named, for example. Significant deviations between nominal and measured coordinates occur in a range of several centimeters. Only intensive investigations can help to reach the theoretical limitations here.

This thesis deals with several aspects which affect the measurements of RIM cameras. First, a short introduction into the basic technologies that are associated with RIM is presented. Besides imaging and distance measurement methods, two basic principles of RIM are distinguished. Furthermore, the focus is laid on the specific limitations. During this work three different cameras have become available: the SwissRanger SR-2 and the SR-3000 from CSEM / MESA Imaging (Switzerland) and later on the 3k-S from PMDtec (Germany). These three cameras are based on the indirect Time-of-Flight principle and are equipped with different sophisticated features. Besides integrated calibration and correction functionality, the suppression of background illumination is one of the main features. However, these cameras are only intended to be highly developed demonstrators. An adaption to the specific application areas, like automotive or robotics, leads to specialized properties according to the desired claims.

The analysis of the existing camera types helps to understand the technology more closely. The raw data of the analyzed cameras is not more accurate than a few centimeters. In order to investigate the properties of the available cameras, special experimental setups had to be developed. The main part of this work deals with the investigation and calibration of the components of RIM cameras. The geometrical deviations of the optical system are addressed by means of a photogrammetric camera calibration. The distance measurement system is analyzed with respect to the deviations and statistics. Thus, limitations of both precision and accuracy are indicated. Besides the influences of the scattering effect, integration time, emitting system, and angle of incidence, target reflectivity, external and internal temperature, and finally linearity and fixed-pattern noise are discussed. Further on, an approach for a system calibration process is presented. Due to the complexity of the influencing parameters, a complete correction of the measurement data with respect to the diverse influencing parameters has not been reached. But the highly systematic dependencies promise sophisticated calibration routines in the future. This work contributes to the understanding of the sensors.

Nevertheless, the investigated influences of temperature on the distance measurement accuracy, which is indicated as a measure for the deviation between true and nominal value, have been significantly reduced by an uncoupling of the distance measurement and the external and internal temperature by means of a relative measurement setup. The introduction of an internal reference light path helps to reduce the temperature's influence on the distance data to a large degree. The experimental setup and the proof of the functionality complete this work.

The results of the numerous investigations will help to increase the accuracy of RIM cameras, especially vital for several applications, in need of improved accuracies. It has been shown that the theoretical limits lie within reach with help of suitably sophisticated calibration procedures.

Zusammenfassung

In den letzten Jahrzehnten wurden zahlreiche Sensorsysteme zur dreidimensionalen Erfassung der Umgebung entwickelt. Neben Laserscannern und geodätischen Totalstationen gehören Stereo-Vision- und Triangulationsmethoden zu den gängigen Verfahren. Insbesondere Laserscanner stellen bezüglich Geschwindigkeit und Genauigkeit der Erfassung von Objekten bis zu einer Ausdehnung von mehreren Zehnermetern den momentanen Stand der Technik dar. Ihr grösstes Manko ist ihre sequentielle Arbeitsweise: es wird ein Punkt nach dem nächsten gemessen. Vor einigen Jahren wurde eine neue Technologie bis zur vollen Funktionsfähigkeit weiterentwickelt, deren Vorzüge in der schnellen, simultanen und hochauflösenden Erfassung dreidimensionaler Umgebungen liegen. Sogenannte *Range Imaging* (RIM) oder *Flash Ladar* Kameras basieren auf der Fusion von digitalen Bilderfassungsmethoden und berührungsloser Distanzmessung. Dabei wird jedes Pixel befähigt die Distanz zum korrespondierenden Objektpunkt zu messen. Zwei differierende Verfahren werden unterschieden: direkte und indirekte Laufzeitmessung. Wegen der Parallelität der Erfassung in allen Bildelementen, sind RIM Kameras in der Lage, sogar bewegte Objekte zu erfassen. In Abhängigkeit von den geometrischen Gegebenheiten können 3D Koordinaten aus den primären Messelementen abgeleitet werden. Die nominelle Genauigkeit der Distanzmessung liegt bei einigen Millimetern. Damit besteht die Aussicht, dass RIM für viele Anwendungen interssant wird. Dazu ist es aber notwendig, die Eigenschaften dieser Technologie zu beherrschen. Automobilindustrie, Robotik und Sicherheitsanwendungen stehen zurzeit im Vordergrund der Forschungsbemühungen zur Verwendung von RIM Sensoren.

Die vorliegende Arbeit beschäftigt sich mit zahlreichen Aspekten betreffend der Beeinflussung der Messergebnisse von RIM Kameras. Zunächst wird eine kurze Einführung in die Gesamtthematik Range Imaging gegeben, und die wesentlichen technologischen Grundlagen werden dargestellt. Über digitale Bild- und Distanzmessverfahren hinaus werden die beiden Grundmethoden unterschieden. Weiter werden die spezifischen Grenzen der Genauigkeit betrachtet. Im Verlauf der Arbeit standen drei verschiedene RIM Kameras zur Verfügung: die Modelle SwissRanger SR-2 und SR-3000 von CSEM / Mesa Imaging (Schweiz) sowie später die 3k-S von PMD Technologies (Deutschland). Alle diese Kameras basieren auf dem indirekten Laufzeitmessverfahren und sind mit verschiedenen ausgeklügelten Funktionsmerkmalen ausgestattet. Neben integrierten Kalibrier- und Korrekturfunktionalitäten steht bei zwei Modellen die Unterdrückung der Hintergrundstrahlung zur Verfügung. Trotzdem stellen diese Sensoren lediglich Funktionsmuster dar, welche die verschiedenen Möglichkeiten dieser Technologie verdeutlichen sollen. Bei der Adaption in die verschiedensten Anwendungen, wie der Automobilsensorik oder der Robotik, sind spezialisierte Lösungen weitaus geeigneter, die spezifischen Aufgaben zu lösen.

Die Analyse bestehender Kameratypen hilft, diese aufstrebende Technologie besser zu verstehen. Die aus den Rohmessungen (Distanz und Bildpunkt) abgeleiteten 3D-Koordinaten dieser Sensoren sind nicht wesentlich genauer als einige Zentimeter. Für eine Vielzahl von Untersuchungen mussten neue Versuchsaufbauten entwickelt werden. Der Hauptteil dieser Arbeit besteht aus der Darstellung der Untersuchungsergebnisse der Komponentenkalibrierung der genannten Kameramodelle. Die geometrischen Abweichungen des optischen Systems vom Idealmodell wurden von einer photogrammetrischen Kamerakalibrierung erfasst. Das Distanzmesssystem wurde bezüglich der Statistik und Abweichungen vom Soll untersucht. Daher können Aussagen über die Grenzen der Präzision und Genauigkeit gemacht werden. Neben der Analyse des Einflusses von Scattering, Integrationszeit, Beleuchtungseinrichtung und Auftreffwinkel, werden Ergebnisse bezüglich der Einwirkung von Objektreflektivität, externer und interner Temperatur und schliesslich Erkenntnisse über Linearität und Fixed Pattern Noise dargestellt. Darüber hinaus wird ein Ansatz für eine Systemkalibrierung aufgezeigt. Wegen der grossen Komplexität der Abhängigkeiten

der einzelnen Einflussparameter untereinander konnte eine abschliessende Kalibrierung der untersuchten Kamerasysteme nicht erreicht werden. Die hochgradig systematischen Abhängigkeiten zeigen aber, dass eine umfassende Kalibrierung möglich ist. Diese Arbeit stellt einen grossen Schritt in diese Richtung dar und hilft die verschiedenen Bezüge zu verstehen.

Ein wesentliches Ergebnis dieser Arbeit ist die Verbesserung eines bestehenden Systems (SR-3000) in Bezug auf die Empfindlichkeit gegenüber externen und internen Temperatureinflüssen. Dies wurde im Wesentlichen durch den Einbau einer internen Referenzstrecke erreicht, durch welche eine Entkopplung der extern gemessenen Distanzen von etwaigen Temperaturdriften erreicht werden konnte. Dieser relative Messaufbau wurde derart mit einer geeigneten Datenauswertung kombiniert, sodass eine signifikante Reduktion der Temperaturabhängigkeit erzielt wurde. Die Beschreibung des Versuchsaufbaus sowie die Darstellung und Erörterung der Messergebnisse runden diese Arbeit ab.

Die Ergebnisse der zahlreichen Untersuchungen sollen dazu dienen, die Genauigkeit der Messungen derart zu steigern, dass möglichst viele Applikationen davon profitieren. Es wird gezeigt, dass die theoretischen Grenzen betreffend der Genauigkeit der RIM Technologie bei der Anwendung entsprechend ausgereifter Kalibrierprozeduren erreichbar sind.

Contents

List of Tables

List of Figures

Chapter 1

Introduction

Three-dimensional (3-D) measurement techniques have become very popular within the last years, driven by their availability and demand. Besides the determination of position, movement, and orientation of certain objects, also shape and size as well as their short and long-term changes are parameters to be taken into consideration. The complexity of measurements increases with the number of dimensions that have to be considered.

Some tasks are only solvable because of the increased progress in electronics, micro-, and nano-technology. Optical 3-D measurement techniques are highly dependent on improvements in the semiconductor industry. New chip manufacturing and designing processes and decreasing costs are a basis for the ongoing spreading of optical methods for measurement purposes.

1.1 Motivation

A few years ago, a search on the internet gave interesting results concerning a brand new technology. Distance measuring pixels within cameras seemed to be technology of the future, even though the basic principle is very simple. Range imaging (RIM) cameras are able to measure distances to the objects in their field of view in every pixel. Out of this so-called *distance map* or *range image*, 3-D coordinates can be calculated. For the purpose of investigations, one of the first sensors which could be bought was ordered. The first idea was to use the new sensor for geodetic and measurement applications. However, when it was clear that a calibration and investigation could help others (application engineers, researchers), the motivation for this work became to determine and increase the quality of 3-D-range imaging cameras introduced in chapter 2 with exemplary realizations in section 2.3.

At the Institute of Geodesy and Photogrammetry at ETH Zurich, a 3-D camera from the Centre Suisse d'Electronique et de Microtechnique SA (CSEM) was available: the SR-2. After two more years, the follow-up generation camera, the SR-3000, was purchased. Many small improvements were introduced in the meantime. Some of the measurements made with the SR-2 can be found within this thesis. But the main focus is laid on the investigation of the SR-3000. Additionally, a RIM camera from another manufacturer was available, later on: the 3k-S from PMD Technologies. What all systems have in common is that they are relatively new on the market and that some of the performance characteristics are not known very well, so far. Thus, the measured coordinates still suffer in accuracy due to temperature effects, for example.

A measuring result, like a distance measurement, always has two characteristics: first, the quantity, which is the measured value itself, and second, the quality of this value which, can be expressed in several ways. Most common descriptions of the quality of a measurement are the simple offset to the known real value and the standard deviation. To increase the quality of 3-D measurement systems, one could either improve the system's electronics and mechanics, or one could determine the difference

between the measured and the real values to correct the measured data. Therefore, it is necessary to formulate descriptive, sophisticated models and approaches for this correction. This process is also known as calibration.

Many measurement technologies suffer from strong systematic errors. If these errors can be determined, a correction of the measurements leads to better results. Therefore, expensive improvements of the measurement system can be avoided if calibration methods are developed. Many errors stand in close relationship to the sensor's properties. Dependencies between the influencing parameters and the measured values as well as their interdependencies quite complicate the calibration of a 3-D measurement system. It can be seen that a good and, as far as possible, complete knowledge of the properties of a measurement system is vital for good calibration methods.

Figure 1.1 gives an example for the (secondary, derived) output of RIM cameras: three-dimensional point clouds.
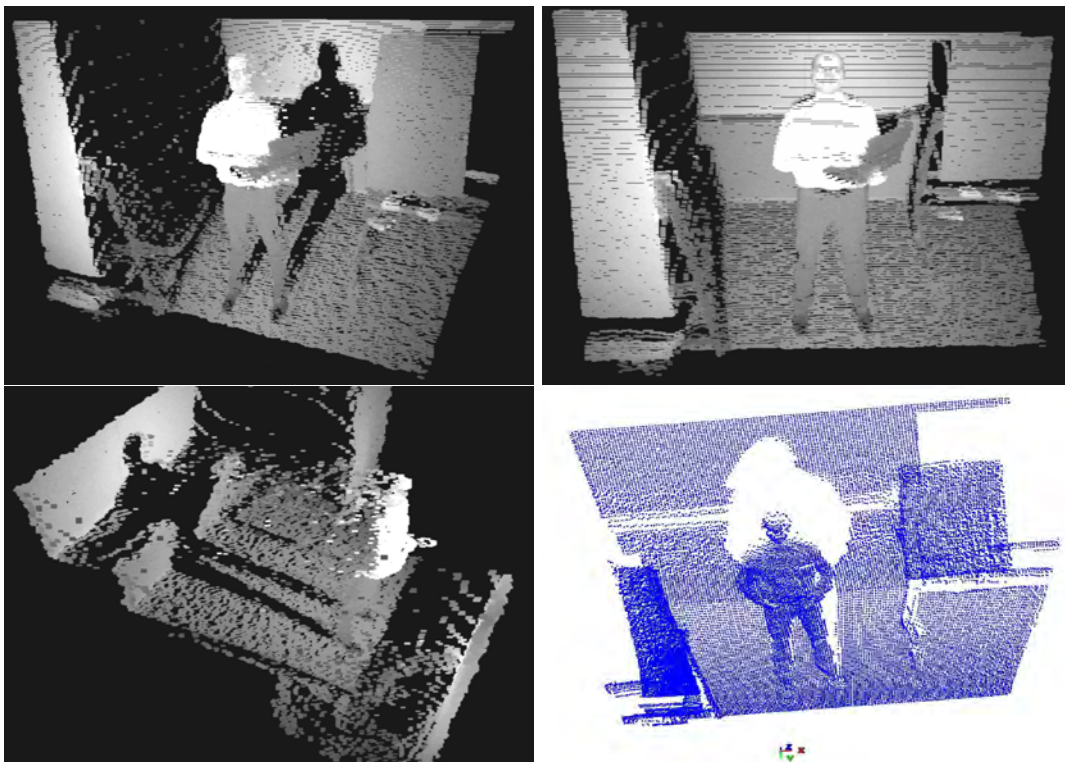
Figure 1.1: *Three-dimensional point cloud acquired by means of a range imaging camera seen from different viewpoints (images 1 to 3) and a second one (image 4). In both cases a person is standing in front of a wall and objects on both sides.*

In the following subsections two possible applications, which can make use of RIM cameras, are introduced. The availability of precise and accurate data is one of the prerequisites for these applications, as well. Thus, a driving factor for motivation of the advancement of the RIM data have been the following examples.

1.1.1   Application: Tracking of People in Indoor Environments

A very interesting application which could benefit from RIM technology is the surveillance of environments including tracking systems for objects or creatures. (Kahlmann & Ingensand 2006) already described the usability for people-tracking by means of a simple threshold filter. Figure 1.2 displays the captured scene on the top, captured by means of a simple CCD camera. Below, the threshold-filtered range images, captured by the SR-2, are shown. Out of the extracted pixels, clusters were calculated. Afterwards, these

clusters were transformed into single 3-D coordinates. The cluster coordinates from a set of images is presented in figure 1.3. It can be seen that the fast acquisition of the SR-2 leads to very dense position data of the tracked person. Besides the path, speed and acceleration can be derived. The used clustering algorithm allows for distinguishing between different spatial disconnected clusters. The main drawback of the implemented tracking is the usage of a centroid operator after the clustering. Because of missing measurements from the back, shadows in the 3-D point cloud occur. In order to generate a suitable setup and analysis, a tracking procedure which integrates a 3-D model is evident.
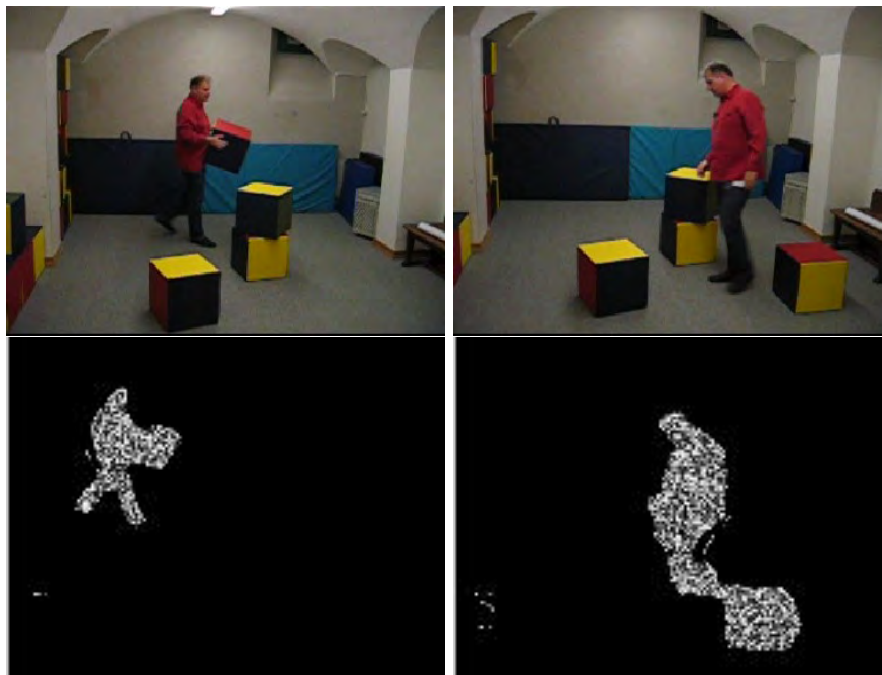
Figure 1.2: *Tracking by means of a threshold filter and clustering. The situation has been captured with a standard digital camera (top). The identified moving pixels (from range images captured by the SR-2) are indicated below.*

Kahlmann et al. (2007) go into detail and even show alternative methods. A bayesian-based CONDENSATION filter was implemented for this purpose. This filter technique was introduced to range imaging by Koller-Meier (2000) based on Isard & Blake (1998). The implementation for use with range images captured by the SR-2 was done by Guillaume (2006) and is not part of this thesis. The particle initialization is depicted in figure 1.4.

Besides the surveillance of indoor and outdoor environments, one idea is to use the RIM technology in the area of psychiatries. Psychiatrists are interested in the behavior and movement of people in order to give diagnosis of certain diseases more credibility. Today's visual diagnosis systems rely upon 2-D video camera systems. Mostly, the inspection of the video material is done manually, image by image. Integration of RIM could ease the professional's work and, thus, could help them to concentrate on other aspects more closely. Motion analysis of extremities is a basic condition for a successful interpretation. This could be achieved by model matching.

1.1.2 Application: Automotive

One of the driving industries for the introduction of RIM sensors in applications, besides robotics, is the automotive industry. Figure 1.5 gives a short overview about the various applications within the automobile. Beyond driving assistance, safety aspects for pedestrians and passengers are in focus. Specifically, sensorics for the intelligent driving of the airbag inflation system can be named here.
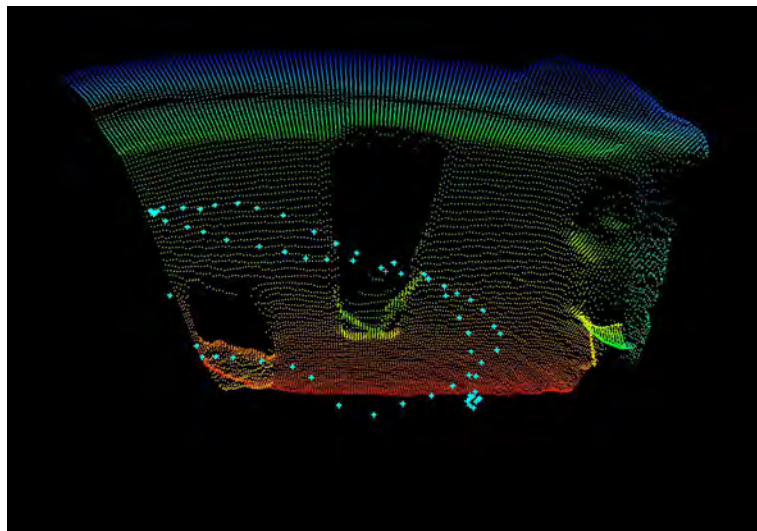
Figure 1.3: *Results of a tracking procedure based on a simple threshold tracker and range imaging. A clustering algorithm has been developed to group all pixels that belong to the same object. The small crosses display the spatial mean position of all indicated moving pixels. Each cross stands for one captured image. A more precise tracking could be reached by fitting a suitable model into the identified 3-D coordinates.*
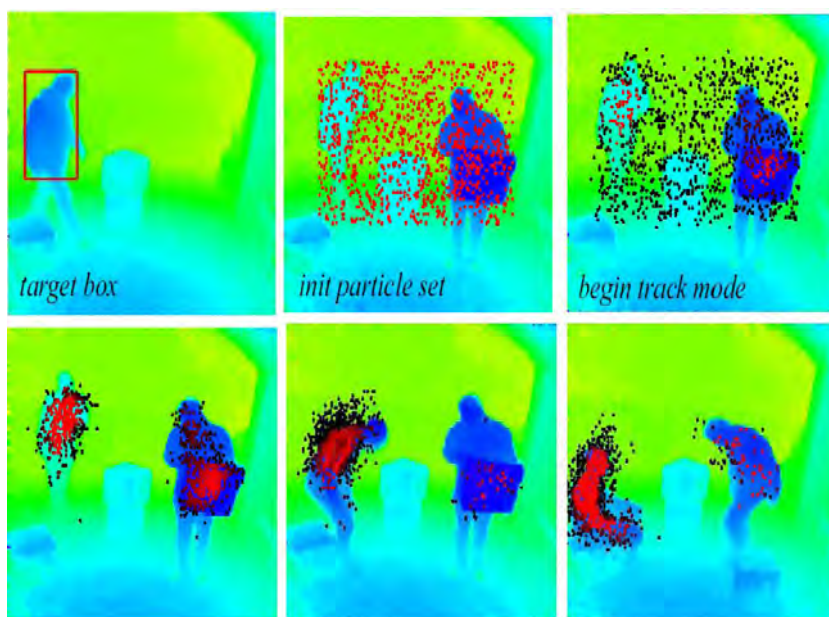
Figure 1.4: *Particle tracking based on CONDENSATION. The initialization process converges very quickly.*

A high number of investigation projects were launched in order to validate the benefit and potential of RIM for the automobile. Some investigations can be found in Reimer et al. (2005) and Zywitza et al. (2005). The main advantages of RIM are the low costs, the fast and accurate data acquisition (after calibration), and the small size of the sensors. One of the main drawbacks can be found within the measurement range with respect to the emitted energy and in the vision problems that occur with fog. Radar has an advantage here with respect to the distance and the fog problem. However, the combination of several sensors will lead to more intelligent and reliable driving assistance systems. Every technology can be used according to its strengths.
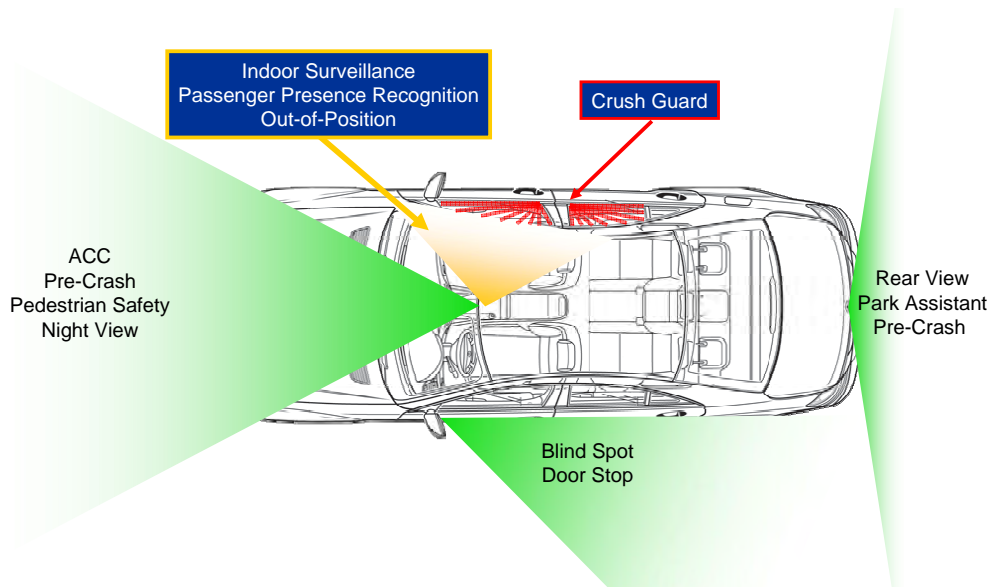
Figure 1.5: *Integration of RIM technology in automotive applications. The various applications of RIM stand in competition with other technologies: ladar, radar, (stereo) vision, and ultrasound (according to Fritzsche (2007)).*

1.2   Aims of This Thesis

Today, most of the available publications writing about RIM deal with the basic micro-electronic construction of the sensors or their application. Only a few have already analyzed the existing systems for the public. Furthermore, the analysis of the precision and accuracy of the diverse systems is still an unsolved task.

With the investigations of a 3-D camera the following goals for this work are aimed. As a basis the sensor properties are to be investigated. In this context special interest is laid on the influencing parameters. Internal as well as external physical influences are to be scrutinized. Besides the determination of the systematic errors, the stochastic characteristics are essential for the investigations. Because of the complexity of such a system, several influencing parameters have to be described and investigated. The goal is to reach a precise understanding of the properties of the investigated 3-D camera.

The second main aspect is to increase the accuracy of the 3-D camera. Therefore, the investigated properties have to be taken into account. Several approaches for the correction of the 3-D data have to be considered and evaluated concerning the ability to increase the accuracy and reliability of the system. This work also shall offer inputs for the calibration as well as comprising the development of a suitable calibration strategy. These aspects are an inevitable task of this thesis.

As investigations have shown, the complete calibration of a sensor was not possible within this work. Even though the first idea was to support the users of RIM cameras with a calibration toolbox, some tasks have become too expensive considering the available research recources to be fulfilled in a single dissertation thesis. Therefore, the presented investigations shall help in better understanding the characteristics of RIM cameras, especially the investigated ones, of course. During this work intensive communication with the manufacturers took place. However, this thesis can be understood as a compilation of a development process toward this new technique.

1.3   Structure

This work is structured as follows. This introduction is followed by an overview of several 3-D measurement technologies in chapter 2. The systems paid attention to in this work are described in detail. The basic principle as well as their specific implementation are explained. Besides a short description of the CMOS/CCD-method used in 3-D cameras, the fundamentals of range imaging are outlined.

The main chapter, chapter 3, deals with the properties of some sensors, mainly the SR-3000. Many different parameters, influencing the measurement results, are described and investigated. For this reason, a distinction between external and internal aspects is made. Often it is not possible to distinguish between several characteristics because of their high correlation. That is why in some cases only a combined effect can be perceived. As mentioned before, it is evident to include the properties of a sensor into the calibration approach. Chapter 3 also gives several proposals for calibration methods. First, the differentiation between the camera-like part (cf. section 3.2) and the distance measurement system (cf. section 3.3) is made. For both, calibration approaches are outlined. in particular, the camera calibration is more or less an extraction out of the large amount of ways for possible photogrammetric camera calibrations, as found in photogrammetric literature. Section 3.4 shows a possibility for a specialized calibration method for 3-D cameras and other 3-D measurement systems. The aim to reach for on the one hand accurate and on the other hand simple calibration methods helps to differentiate the proposed approaches. Accuracy and simplicity of the calibration types stand in foreground.

It has been shown that temperature effects are one of the dominant influences in range imaging. In order to reduce some specific influences, a modification of the existing RIM camera SR-3000 was done. These changes, as well as results of its investigation, are shown in chapter 4. Because these investigations were carried out very late in the progress of this work, an adaption to the previous calibration investigations has not been possible.

This work will close with a conclusion in chapter 5. A brief outlook is given with respect to future development of this tremendous technology.

Chapter 2

3-D Range Imaging Camera Technology

In recent years, several range imaging cameras became available on the market. RIM cameras have the ability to capture their environment fast in three dimensions. These acquired spatial data then are the basis for use in various kinds of applications. This chapter will give an introduction to the implemented 3-D measurement technology. First, the fundamental distance measurement techniques will be shown (section 2.1). Basics of semiconductor imaging are pointed out in section 2.2. In the following, the implementation of distance measurement technology into a semiconductor array will be examined in a more detailed way (section 2.3). The presentation of working realizations of the range imaging principle is included with respect to different methods. In section 2.4, calculation of 3-D coordinates out of the measured elements of the RIM technology will be introduced.

2.1 Distance Measurement

One of the basic functionalities of a range imaging camera is the distance measurement system. Many different ways and methods of electro-optical distance-determination are known. An overview of some of the numerous types can be found in Burnside (1971), Zetsche (1979), Bolsakov et al. (1985), Hennecke et al. (1994), Schwarz (1995), Rüeger (1996), Kahmen (1997), Baumann (1998), Löffler et al. (2002), and Ingensand (2002), to name only a few.

The most current developments about this topic are presented but unpublished in Hinderling (2004). Unfortunately, most of the details of advanced ranging are whether unpublished or give too unspecific in patents. Two of the main patents, according to the range imaging technology, are held by Gächter (1996) and Spirig & Seitz (1996).

2.1.1 Time-of-Flight Distance Measurement

The method used in the 3-D RIM cameras applied in this work to measure distances is the Time-of-Flight measurement principle (ToF). This principle uses the limited propagation speed of light defined implicitly as (NIST 2001):

$$c = 299792458 \quad m \cdot s^{-1} \tag{2.1}$$

A light pulse is considered to travel a certain but unknown distance D with the speed c. Figure 2.1 depicts the situation schematically. If the time elapsed (Δt) that this specific light pulse needs to travel is known, the distance D can be calculated. If the light travels from the emitter to the object, is reflected, and travels the same way back to the receiver, then the distance between emitter/receiver and the object
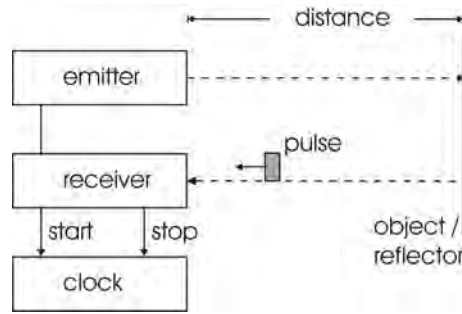
Figure 2.1: *Pulse runtime distance measurement principle according to Zetsche (1979).*

has to divided by 2, because the light has traveled the way D twice:

$$D = \frac{c \cdot \Delta t}{2} \tag{2.2}$$

To determine the distance by time difference, measurement of a single light pulse could be considered to be the basic method of the ToF distance measurement principle. It is used mainly in avalanche photodiode-based 3-D cameras. For a distance resolution of 1 cm, a time resolution of about 67 ps has to be achieved. This principle of distance measurement is used in the range imaging principles and systems as they are introduced in sections 2.2.1 and 2.3.3. It is also known as the *direct Time-of-Flight* method, because the runtime of the light is measured by means of a clock directly.

2.1.2 Phase-Difference Distance Measurement

2.1.2.1 Working Principle

Another variation of the ToF principle is to use not only a single pulse but a more complex, structured radiated signal. Light can be modulated in amplitude, polarization, frequency, or phase. The use of amplitude-modulated light, as done with light pulses (cf. section 2.1.1), also leads to the phase measurement principle. This can also be explained by the runtime of the modulation information over the distance. But more illustrative is to take a closer look at the correlation theory of amplitude-modulated light, which is the method used in the investigated 3-D camera. The ToF phase difference measurement theory is described in detail by Lange (2000), where several influencing parameters are alos analyzed and discussed. Figure 2.2 shows, analog to the ToF distance measurement principle, the phase difference distance measurement principle. This method is also known as the *indirect Time-of-Flight* distance measurement principle.
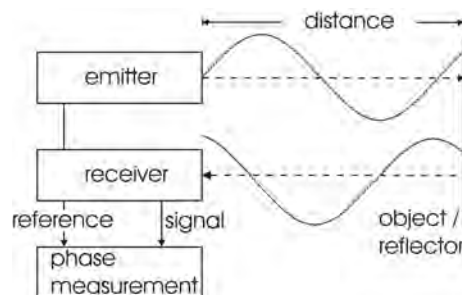
Figure 2.2: *Phase difference distance measurement principle according to Zetsche (1979). The carrier wave is not shown in this case.*

As it can be seen, a periodic signal is sent out by the emitter, is reflected by an object, and partially scattered back to the receiver. The phase difference between the emitted and received signal stands in

relation to the distance D. The kind of modulation used for the investigated 3-D camera is the amplitude modulation. Figure 2.3 shows the detailed signal structure for a sinusoidal amplitude-modulated carrier wave. Only the amplitude of the reflected signal is shown. The reference signal is defined with phase $\varphi = 0$. Therefore, the phasing of the received signal equals the phasing of the difference signal. The distance to the point of reflection is directly proportional to the phasing of the incoming modulation wave (Oggier et al. 2004). Equation 2.3 depicts the relation between phase shift φ and the distance between sensor and reflector:

$$D = L \cdot (\frac{\varphi}{2\pi} + N) \tag{2.3}$$

Where L is the non-ambiguity distance defined by the modulation wavelength λ_{mod}:

$$L = \frac{c \cdot \lambda_{mod}}{2} \tag{2.4}$$

As it can be seen, offset and amplitude of the emitted and received signal have no direct effect on the measured distance. The influence on the accuracy is discussed later. For the full reconstruction of the incoming signal, four parameters are needed: amplitude, offset, angular rate and, of course, the phasing. To determine these parameters, the intensity of the incoming wave is measured. This so-called *demodulation* of the received signal is the main task of distance measurement sensors. The technical implementation is discussed in section 2.3.
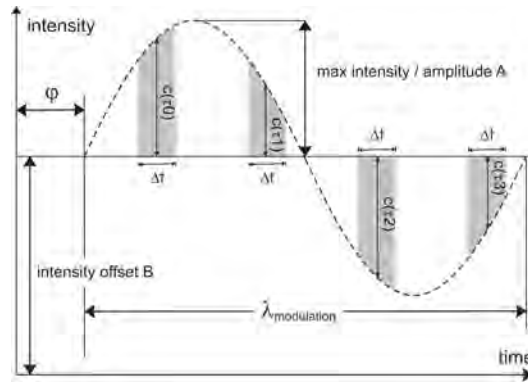
Figure 2.3: *Phase measurement principle (according to Lange (2000)). The incoming wave is shifted in amplitude, offset and particularly in phase to the not shown emitted wave ($\varphi = 0$). The demodulation process can be done by means of four measurements $c(\tau_i)$ of the intensity.*

As figure 2.3 indicates, out of four measured intensity values c, the incoming periodic signal can be reconstructed. For the simplicity of the calculations, these intensity values are measured with a phase shift of $\pi/2$. As Lange (2000) shows, the phasing φ can be calculated out of four intensity measurements $c(\tau_i)$ with $i = 0...3$:

$$\varphi = \arctan \frac{c(\tau_1) - c(\tau_3)}{c(\tau_0) - c(\tau_2)} \tag{2.5}$$

The amplitude A and the intensity offset B also can be determined by (e.g., Oggier et al. (2004) and Büttgen et al. (2004)):

$$A = \frac{\delta}{\Delta t \cdot \sin \delta} \cdot \frac{\sqrt{(c(\tau_3) - c(\tau_1))^2 + (c(\tau_0) - c(\tau_2))^2}}{2} \tag{2.6}$$

$$B = \frac{c(\tau_0) + c(\tau_1) + c(\tau_2) + c(\tau_3)}{4} \tag{2.7}$$

With $\delta = \pi \cdot \Delta t/T$. Δt is the integration interval and T is the modulation period.

2.1.2.2 Characteristics and Limitations

Because of the measurement principle, it is necessary to integrate the intensity over a small period of time Δt (light is quantized and, therefore, there is no continuous flow). Lange (2000) shows that this integration interval which is caused by the limited bandwidth of the sampling system has no influence on the measured phase if the integration time is shorter than the modulation period but it has a direct influence on the demodulation depth.
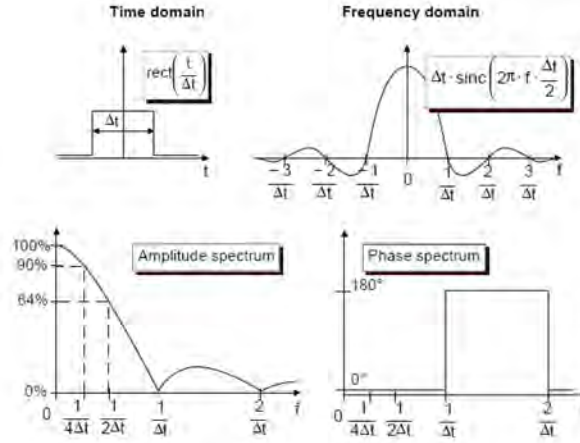
Figure 2.4: *Influence of the sampling interval (see Lange (2000)).*

Figure 2.4 clearly shows that the shorter the integration interval chosen, the better the amplitude can be reconstructed. This also is reflected in the achievable depth resolution ΔD, which is expressed by:

$$\Delta D = \frac{L}{360°} \cdot \Delta\varphi = \frac{L}{\sqrt{8}} \cdot \frac{\sqrt{B}}{2 \cdot A} \tag{2.8}$$

Beyond the limited bandwidth of a sensor, another factor requires Δt to be expanded. One of the limits for the optical distance measurement is photon shot noise.

Another way to describe the distance precision can be found in Lange (2000), wherein the signal to noise ratio (SNR) plays a role:

$$\Delta D = \frac{1}{\sqrt{N_{phase}}} \cdot \frac{1}{k_{tot} \cdot \frac{S}{N}} \cdot \frac{\lambda_{mod}}{\sqrt{8} \cdot \pi} \tag{2.9}$$

where S is the number of signal electrons, N the total number of the different noise electrons, k_{tot} the modulation contrast, N_{phase} the number of measurements carried out for one distance, and λ_{mod} is the modulation wavelength. As expected, the SNR and the modulation contrast play a significant role. Less noise increases precision. What has to be treated carefully is the $\frac{1}{\sqrt{N_{phase}}}$ factor. This implies that if the number of measurements is high enough, the precision increases. It is certain that precision cannot be increased beyond a specific limit. Otherwise every insufficient measurement system could be used even for high- accuracy applications (context dependent). Experience shows that this is unrealistic. Most systems do not fully follow Gaussian distributions. In the past few years especially, the importance of modeling the systematic errors came into awareness. Kutterer & Schön (2004) particularize this aspect.

The statistical behavior of light plays a relevant role in the case of low optical power. It has been shown that photon shot noise is the limiting factor for the presented method of range measurement (Lange 2000, Büttgen et al. 2004, Oggier et al. 2004). Seitz (2005) shows more clearly that because of the Bose-Einstein distribution of thermal-generated light, the reachable accuracy is limited and it is lower than with coherent light, which itself follows the Poisson distribution. Figure 2.5 points out these aspects in detail. In case of the investigated sensors, we deal with emitting systems built on LEDs and, therefore, radiation that follows rules that are placed between both extremes of Bose-Einstein and Poisson.
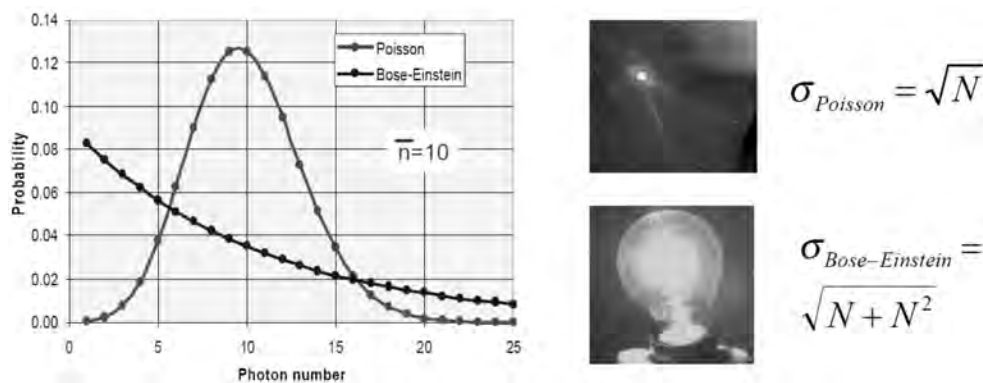
Figure 2.5: *Bose-Einstein and Poisson-distribution of different generated light (Seitz 2005).*

Coherent radiation follows the rules of the Poisson distribution. This means that the number of photons, with respect to radiation and detection, scatter around the mean value (figure 2.5 $\overline{n} = 10$) with the mean value as a maximum. This is due to the more or less uncorrelated generation properties. In the case of thermal-generated light, the several photons are correlated in their formation process. Because of this statistical dependency, they obey the rules of Bose-Einstein (Seitz 2005). As figure 2.5 outlines, even with a mean value of e.g. $\overline{n} = 10$, there are more singular photons that exist. These distributions result in the standard deviations shown in figure 2.6. In most cases the real deviation lies between these extremes.
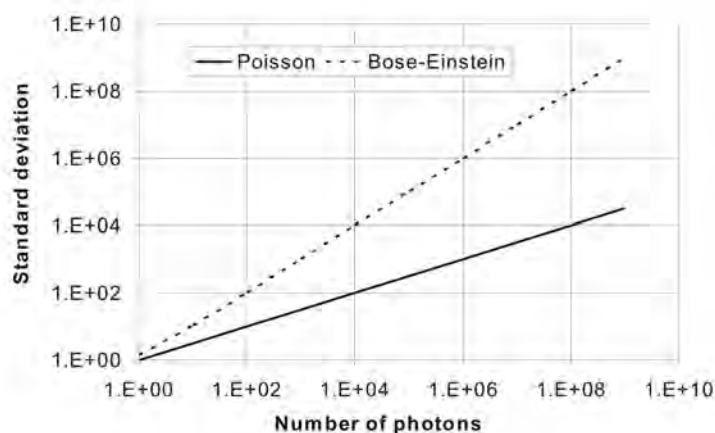
Figure 2.6: *Precision of Bose-Einstein and of Poisson-distributed light (Seitz 2005).*

Equation 2.8 refers to the ideal case where coherent light sources with a dominating Poisson distribution are used. It shows, therefore, the limits of the method indicated here. Oggier et al. (2004) reveal that the distance accuracy limit, determined by the photon shot noise, can nearly be reached with existing technologies in range imaging (figure 2.7; a non-optimized test bench was used for the measurements). It is known that there are several other aspects to be considered which further decrease the reachable accuracy, as there are speckle and diffraction, for example.

For reflectivity-based measuring systems, it is necessary to take a closer look at the principles of reflectivity itself. Several models exist for the description of the reflectance of surfaces. For vision-based measuring systems, lambertian reflectors are optimal. Figure 2.8 shows on the left side the reflectance model of Lambert. According to Gerthsen & Vogel (1993), a lambertian reflector follows the rules of
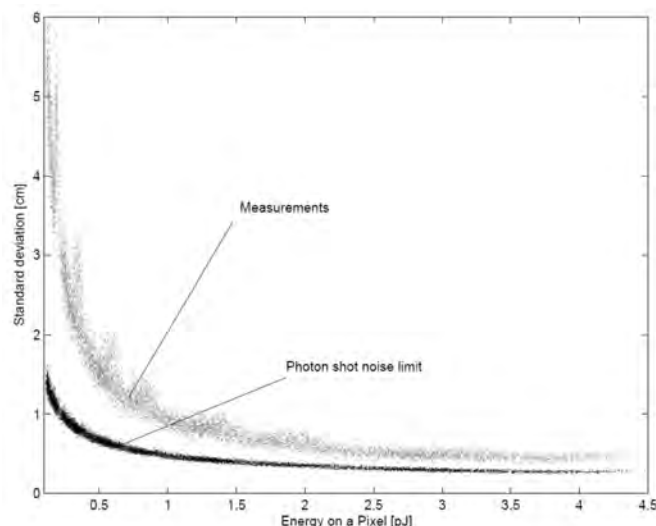
Figure 2.7: *Measured distance accuracy toward theoretical limit of photon shot noise with range imaging technology (Oggier et al. 2004).*

Lambert's law:

$$J = J_0 \cdot cos\theta \tag{2.10}$$

where J is the intensity of radiation and θ is the angle of incidence toward the surface normal. Therefore, the perceived radiation integrated by a solid angular section is equal in every direction. Phong (1975) improved this model through a combination of lambertian and total reflectance. The right side of figure 2.8 shows a typical reflection of Phong's model. The model has been proved by Lomba et al. (1998).
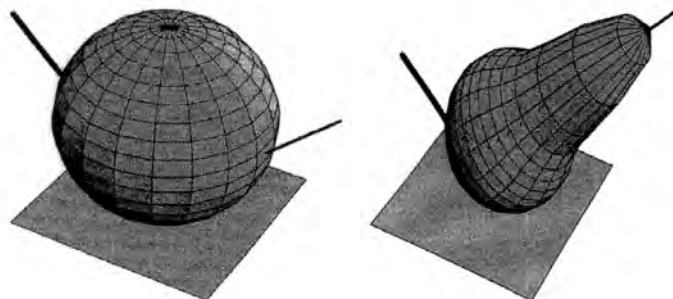
Figure 2.8: *Reflectivity of a lambertian surface (left) according Lomba et al. (1998) and a typical reflectivity (right) after Phong (1975).*

In addition, Bosch & Lescure (1995) showed that there is a high influence of total reflection (figure 2.9). Therefore, it can be concluded that with collinear systems, a decreased amount of reflected light will be acquired if the angle of incidence increases. This fact will be of importance in section 3.3.6.

What remains to be considered is the signal structure of the emitted signal. Lange (2000) showed different possible signal structures and their systematic influence on the measured distance. Because of the properties of the emitting system electronics and the different light sources, there are several possible signal structures that are finally emitted by the emitting system. The signal displayed in figure 2.3 is an optimal cosine. Lange (2000) analyzed different modulation signals concerning their influence. He showed that even harmonics remain without any effect on the distance measurement. Only uneven harmonics play a role. If a square wave modulation (on and off) is used, the uneven harmonics that this function contains have a large influence, which results in a periodic (sinusoidal like) variation of the distance values. This will be of importance in section 3.3.8.
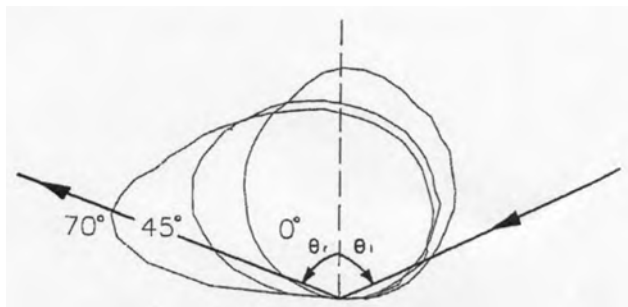
Figure 2.9:   *Reflectivity measurement results of white paper (Bosch & Lescure 1995)*
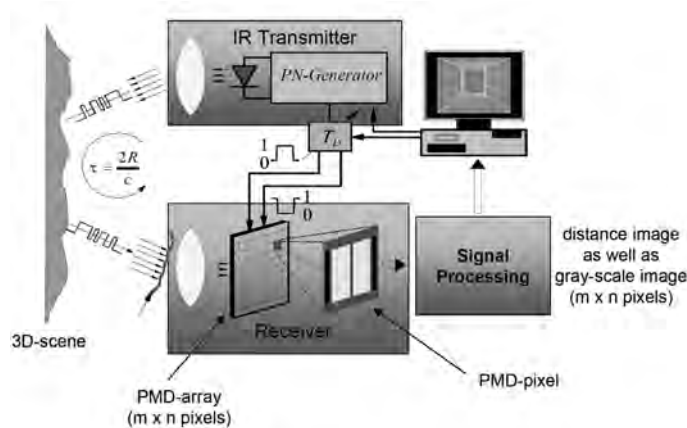
Figure 2.10:   *Pseudo-Noise (PN) amplitude modulation for the use in 3-D cameras (see Zywitza et al. (2005) and Schwarte (2005b)).*

Lange (2000) already has shown an important side effect of the sampling process with respect to its spectral selectivity. It has been shown, that the phase reconstruction (demodulation) algorithm (equation 2.5) is not sensitive to quadratic system non-linearities and even-harmonics of the modulation signal. Uneven-harmonics result in a cyclic effect in the distance offset. A very important effect of this algorithm is the sharp spectral selectivity, which helps with respect to the implementation of multiple cameras in one measurement system. Due to this property, the measurement units (i.e., pixels) are called *Lock-In Pixels*. The functional dependency between the measurement signal f_1 and a spurious signal f_2 is given by

$$A = sinc \left(2\pi \cdot \Delta f \cdot \frac{T_w}{2} \right) \tag{2.11}$$

In case of the use of two similar measurement systems ($f_1 = 20\ MHz$ and $f_2 = 20.1\ MHz$) and a postulated signal suppression of better than $40\ dB$, an integration time of $1\ ms$ is sufficient. This is easily reached in most cases.

Advanced methods use highly structured light. Beyond the shown single-frequency amplitude modulations, several other modulations are possible. To increase the non-ambiguity distance range it is possible to use more than one modulation frequency. As a method state-of-the-art the Pseudo-Noise (PN) modulation can be named. Figure 2.10 depicts this shortly. A detailed description can be found in Klein (1993).

Additionally, an aspect to mention is the type of modulation of the LED-based emitting systems. Burst modulation is mostly used because of the high energetic output. It is assumed that the use of a high number of emitters leads to a nearly sinusoidal-modulated overall signal.

2.2   Imaging Technology

A treated semiconductor has the ability to convert light (which is a form of electromagnetic radiation) into charges. How this internal photoelectric effect proceeds is shown more clearly in Gerthsen & Vogel (1993) and Janesick (2001).

Pure semiconductors (normally silicon or germanium) have poor conductivity. To increase their conductivity they can be doped with neighboring atoms in the periodic table of elements. To reach an increased number of movable electrons in the semiconductor, it is donated with phosphorus or arsenic atoms. The result is an n-doped semiconductor; p-doped semiconductors are missing one electron for covalent bond because of boron, aluminium or indium atoms. The concentration of donators (n-doped) and acceptors (p-doped) in the crystal structure of the semiconductor normally is as high as 10^{15} to $10^{20} atoms/cm^3$ of the semiconductor (Lange 2000).

Well-energized photons with an energy $E = h \cdot \nu$ interact with the material and create free electrons (electron–hole pair). An electron is moved by means of the energy of a photon from the valence band of the crystal structure to the conduction band (figure 2.11). The electron now has a higher energy and is movable. A positive-charged hole remains in the valence band. Without any force that separates the electrons from the remaining holes, the charges will quickly recombine.
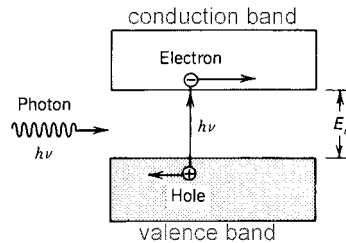
Figure 2.11: *Electron separation within semiconductor (Saleh & Teich 1991). An electron is excited because of absorbtion of photons from the valence band into the conductive band, also known as internal photoeffect.*
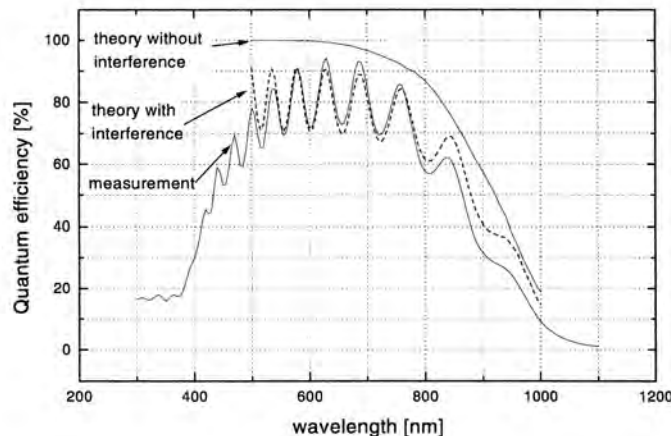
Figure 2.12: *Quantum efficiency of a special semiconductor (Spirig 1997). In the context of this work, the only important aspect is the high efficiency in the bounds of the visible light (about 400 to $700nm$).*

Figure 2.12 displays exemplarily the quantum efficiency of a semiconductor device. It becomes clear that the carrier wavelength has to be chosen somewhere in the range between $400\ nm$ and $900\ nm$ to reach a high output and, therefore, a high energetic efficiency of the system (signal emitter and sensor). Due to prerequisites (no visible light because of irritation potential towards humans) most available RIM

systems use a wavelength at about 850 nm. At this wavelength the spectral sensitivity is still high (about 50%). The avalanche photodiode-based systems use laser pulses in the range of about 530 nm to 640 nm. But it is necessary to have a powerful emitting system. The power budget of systems like RIM cameras also is discussed by Lange (2000).

Besides the limitations of the optical system, the noise limitations concerning the range accuracy are discussed. Thermal noise, which means the generation of charges caused by thermal activity and not by optical radiation, is mentioned as well as quantum noise. Quantum noise is reasoned by the statistical Poisson or Bose-Einstein distributed nature of light, especially photons. This is also known as photon shot noise. Shot noise cannot be eliminated or reduced by any technique. It is within the nature of the light and also is one of the limiting factors for such a system. Oggier et al. (2004) carried out measurements that prove this assumption.

Three independent transport mechanisms for electrons are known (Lange 2000):

- self-induced drift

- thermal diffusion

- influence of an electric field

In case of natural recombination, self-induced drift and thermal diffusion are dominant. Both effects are of stochastical nature. For the purpose of the separation of electrons and holes, electric fields are suitable because of their controllable and systematic characteristics. With specialized structures it is possible to prevent the separated charges from recombination and measure their quantity, which is a measure for the number of photons collected from the semiconductor. Many different approaches can be found in literature. The most important key technologies surely are:

- Charge Coupled Device (*CCD*),

- Complementary Metal Oxide Semiconductor (*CMOS*), and

- Avalanche Photodiode (*APD*).

In the following, the difference between these technologies will be described briefly.

2.2.1   Charge Collection

Basically, three different methods measuring charges which result from the internal photoeffect will be shown here:

- Photodiode,

- Photogate, and

- Avalanche Photodiode.

Photodiode   The basic principle of a diode is shown in figure 2.13. A diode consists of two parts: an n-doped and a p-doped semiconductor. These parts are connected to each other. At the junction of the basically electrical neutral parts, the movable electrons of the n-conductor flow into the movable holes of the p-conductor. This proceeds until the now-increasing electrical field (n-conductor becomes positive and vice versa) hinders more electrons to move to the holes in the p-conductor. The resulting area at the junction is called the *depletion region*. This expresses that no more mobile electrons are available. If a voltage is laid the way that the naturally arisen electrical field is supported, the diode is driven in *reverse biased mode*.

If free electron-hole-pairs are created by means of the internal photoelectric effect due to absorbed, well-energized photons, they will move due to their charge either to the already positive-charged n-conductor (electrons) or the negative-charged p-conductor (holes). This separation due to the external electric field only fully takes place in the depletion area at the p-n-junction (1) because it is only there that an electric field exists (figure 2.14). In the junction-near areas (2), the separation is still possible due to the self-induced and thermal drift of the charges. They can drift into the depletion area (1) and can then be separated. In the remaining non-depleted areas (3), the probability of natural recombination is very high. Finally, the photon-generated charges can be measured either by registration of the direct current or by collection and measurement by means of amplifiers.
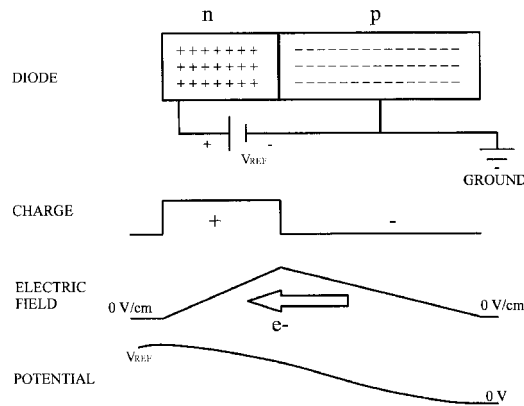
Figure 2.13: *Diode principle (Janesick 2001). Electrons flow from the n-conductor to the holes in the p-conductor until the increasing electrical field stabilizes the situation.*
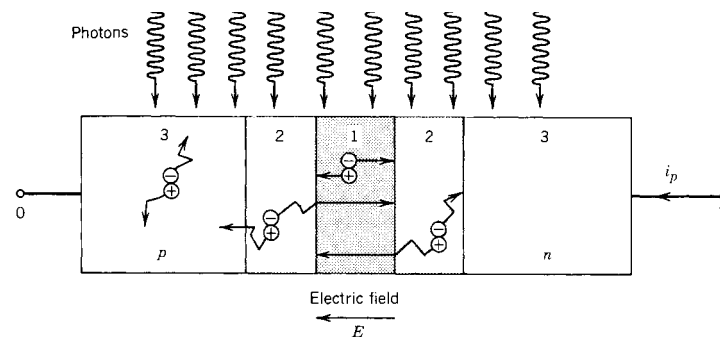
Figure 2.14: *Photon-generated charge-separation in a photodiode (Saleh & Teich 1991).*

Photogate   The photogate collects photon generated charges. As depicted in figure 2.15, different implementations are possible. The ones shown here are just the simplest ones. On the left side, a surface photogate can be seen. This type of photogate is made up of a p-doped semiconductor, an insulator, and the photogate-electrode itself. The gate is thin enough to let impinging light pass through. Well-energized photons then end up in charge separation. Because of the gate's voltage, the charges are separated macroscopically and hindered from recombination. Due to the insulator, the charges moving towards the gate will rest there. They are trapped within a potential well. The left side of figure 2.15 shows such a surface channel photogate. On the right side, a buried-channel photogate is shown. In this case the semiconductor consists of two different doped layers. As a result, the potential well's maximum lies within the semiconductor, not close to the surface as with the surface channel photogate. The advantage of this structure will become clear in section 2.2.2. Photogates can be implemented in both CCD and CMOS sensors.
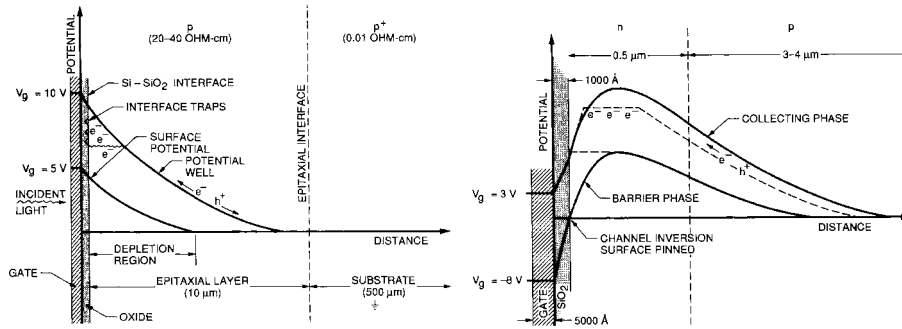
Figure 2.15: *Two kinds of photogates: surface photogate and depleted photogate with buried-channel potential well (Janesick 2001).*

Avalanche Photodiode An avalanche photodiode is a diode run in a strong reverse-biased mode (Saleh & Teich 1991). Therefore, the depletion region is infiltrated with a strong electrical field. Photon-separated charges are accelerated in this field. If their energy becomes high enough, they have the ability to ionize the semiconductor by means of impact and, therefore, to separate secondary charges. This results in another pair of charges accelerated in the field (figure 2.16). The acceleration and multiplication goes on until the charges reach the borders of the electric field. This cascade (or avalanche) effect allows for detection of single photons, due to the increased sensitivity. Even single photons result in a measurable output because of the amplification. In dependency of the reverse voltage, different driving modes are possible. The first way to drive an APD is to use it in *linear mode.* The reverse current is just below the breakthrough current of the diode. Then, the photocurrent is diverted fast enough and the measured current is proportional to the incoming amount of light. The gain is one of the description parameters of such an APD. Within the so-called *Geiger mode*, the reverse bias is high enough to create more electron-
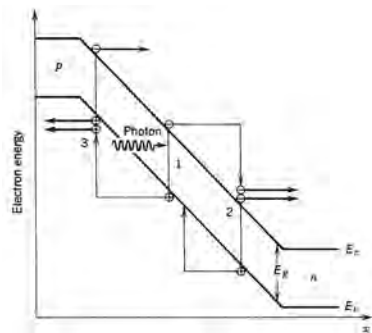
Figure 2.16: *Avalanche photodiode working principle. The photon-generated charge starts the cascade effect. The acceleration in the strong electric field results in a multiplication of the separation of charges initiated by the photoeffect (Saleh & Teich 1991).*

hole-pairs than can be diverted. Therefore, a short current peak can be measured. The disadvantage is that one single photon can cause the breakdown of the diode so that there is no remaining information about the intensity of the incoming light and other photons impinging during the recharge- or dead-time of the diode. All pulses have the same amplitude. If a distance measurement system, as indicated in figure 2.1, is to be implemented, the APD in Geiger mode is a sufficient way to detect the flank of the incoming light pulse. A more detailed description of this topic can be found in Aull et al. (2002), exemplarily. As Niclass et al. (2005) propose, an APD driven in the Geiger mode helps to indicate the intensity of the incoming light by integration and by averaging over time, respectively. The intensity information, as well as noise information, can be derived by the counts-per-time interval ratio and its changes. Figure 2.17 outlines an APD designed in CMOS technology. This APD works in Geiger mode, as well.
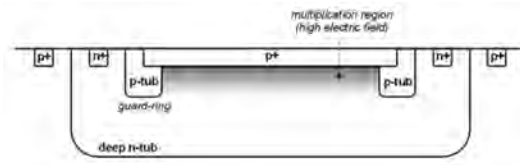
Figure 2.17: *Avalanche photodiode in CMOS technology (Niclass et al. 2005).*

One advantage of single photon avalanche diodes (SPAD) as proposed by Niclass et al. (2005) is their ability to detect even low levels of light. Thus, inexpensive milliwatt laser sources are sufficient for distance measurement up to several meters.

The dead time plays an important role in the classification of SPADs. After a Geiger pulse is triggered, the avalanche has to be quenched. This is done by a short lowering of the bias voltage. After the quenching of the avalanche, the diode has to be charged again. The time needed to recharge the diode up to 90% of the nominal bias voltage is called dead time. For SPAD used in RIM, the dead time is typically less than 40 ns (Niclass et al. 2005).

Another parameter for the characterization of SPADs is the dark count rate (DCR). Due to the characteristics of semiconductors, thermally generated charge-carriers occur. These carriers, as well as carriers tunneled from neighboring SPADs, can trigger avalanche pulses. These false signals are indistinguishable from true distance equivalent signals. The only way is to statistically filter these failure measurements out or to avoid them as far as possible, of course.

Additionally, so-called after pulses may appear. Carriers are possibly trapped after a Geiger pulse in the multiplication region. After a short period they cause a new Geiger pulse and, therefore, wrong measurements.

Another important APD-specific property is the timing resolution or timing jitter. According to the measurement principle, the distance measurement is based on a time measurement. Therefore, an exact determination of the time difference between the emission and the detection of a laser pulse is vital for a high precision. The statistical fluctuation of this time, highly dependent on the time the first generated charge needs to cause an avalanche, has to be small or at least constant and deterministic. Figure 2.18 points out a timing jitter for a demonstration SPAD used in RIM (Niclass et al. 2005). More details about SPADs in RIM can be found in Rochas (2003).
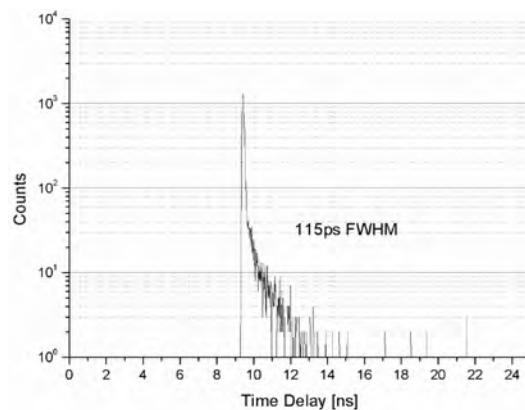
Figure 2.18: *Timing jitter of an SPAD in CMOS (Niclass et al. 2005).*

But even for CMOS SPADs, distance accuracies in the millimeter range can only be achieved by averaging. Figure 2.19 shows 10000 measurements. A significant but low noise level can be seen. Averaging leads to a noise reduced mean with higher precision. To achieve better accuracies, systematics have to be eliminated.
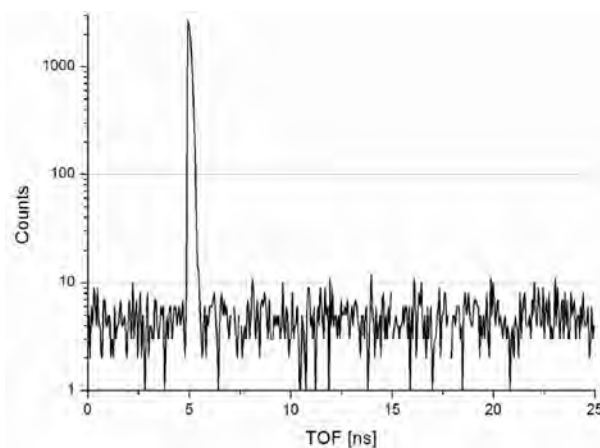
Figure 2.19: *Measurement of the Time-of-Flight with an SPAD.*

2.2.2   Charge Transfer and Quantification

In section 2.2.1, the basic types of charge collection, specifically photon-to-charge conversion techniques, were introduced. In this section the main focus is laid on the charge transfer and the complex implementation of the methods shown above. Three different methods will be pointed out:

- CCD sensors

- CMOS-based sensors

- APD/CMOS-based sensors

These methods are chosen due to their proved utilization in 3-D range imaging sensors.

CCD Principle   For imaging purposes, an array of sensing elements has to be set up. In case of CCDs, photogates are chosen due to their ability to separate and transfer charges within a semiconductor. The basic principle of CCD sensors is outlined in figure 2.20. In 1969 W. Boyle and G. Smith invented a principle: how to move generated charges within a semiconducting device. The main problem is to move charges to an amplification and measuring unit beneath or within the semiconductor. In the case of CCD imaging devices, the charges produced by the internal photoeffect in the semiconductor under a photogate, as shown in section 2.2.1, are moved by means of potential variations within the semiconductor caused by variation of the gate voltage.
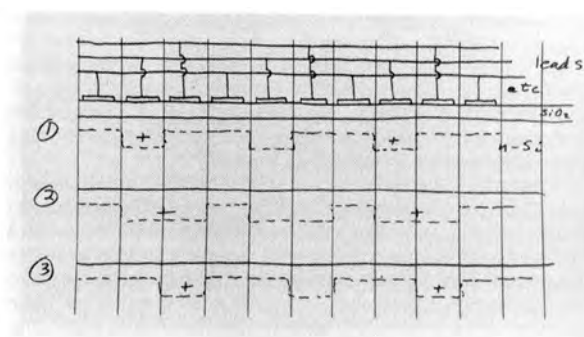
Figure 2.20: *Basic principle of CCD construction and charge transfer according to their first inventors Boyle and Smith (Janesick 2001).*

Figure 2.20 outlines that at least three photogates can work in a serial way to move the charges. Photon-generated charges collected beneath the only active gate of three (compare state 1) are moved

stepwise. In state 2, the gate next to the first one is activated and the charges fill the well, equally
distributed. In the third step, the charges are driven together by deactivating the first gate. The only
active one now is the second gate. Therefore, the charges are moved one gate further.

Figure 2.15 (right) shows a design basically used in scientific CCDs which reduces the problems of
surface channel potential well with their disadvantages in charge-transfer efficiency (CTE). The quota of
transferred charges from one picture element (pixel) to another is referred to be between 0 (no charges are
transferred) and 1 (all charges are transferred loss-free). Normally CTEs of about 99.9999% can be easily
achieved, more or less (Janesick 2001). To reduce traps between the gates they are built overlapping, as
depicted in figure 2.21.
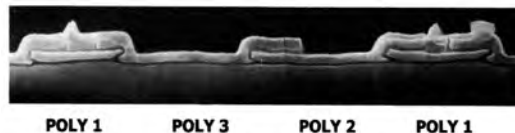
Figure 2.21: *Lateral cut through a CCD photogate (Janesick 2001). The different overlapping gates can
be outlined.*

Therefore, fewer charges are lost between gate switching. The CTE of CCDs has to be very high
because of its operating principle. Every charge is moved across the whole sensor array. In the case
of surface channel devices, some generated charges are trapped in irregularities in the semiconductor–
insulator connection. Therefore, optimal charge transfer is not reached. By means of the buried channel
(figure 2.15), the surface region is avoided with regard to the charge collection and transfer. The n-doped
region beneath the gate works with the p-doted carrier as an diode. The diode's radiation-sensitive area is
the p-n junction. Because of the gate voltage the potential well comes to lie in the n-doped area. Within
the semiconductor, the number of traps and failures is very small. This structure avoids the electrons
to be hindered in their movement by insulator irregularities. Janesick (2001) also describes the different
charge-transfer methods in closer detail. The main errors in semiconductor imaging are addressed in
figure 2.22.
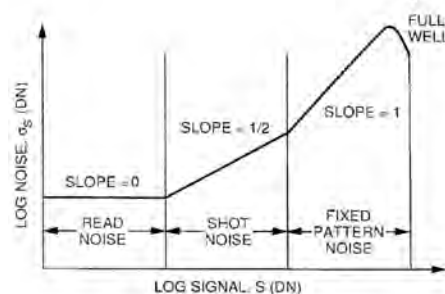
Figure 2.22: *Main Errors in Semiconductor Imaging (Janesick 2001): read noise, shot noise, and fixed-
pattern noise.*

The basic principle of charge measurement in CCDs is to use a single sense node for the whole sensor.
Therefore, all charges are transferred by means of the charge-transfer method described above. Figure
2.23 shows a typical sense node and amplification module used in CCDs. A closer insight is again given
by Janesick (2001). Of importance is the possibility to implement the amplifier within the same silicon
wafer that the charge collection region is built in.

One of the main problems with CCDs is their specialized and expensive production process. Further-
more, the charge transfer cannot be achieved with unlimited speed. It takes a certain time to readout
the whole sensor. In addition, all pixels have to be read whether they are needed or not due to the serial

Figure 2.23: *Output amplifier region for a Hubble CCD and a typical cross-section and schematic (Janesick 2001).*

mode of the transfer operation. It remains time consuming due to inverse correlation of charge-transfer time and CTE (Fossum 1993), which means that a higher CTE results in longer readout time.

CMOS Device   The Complementary Metal Oxide Semiconductor (CMOS) were invented in the 1960s. Basically, this technology is used for integrated circuits like processors and memory chips. But nanomechanical constructions are also possible. The fundamentals of the CMOS process are pointed out in Baker (2005), for example. In the case of imaging devices, the CMOS process is used to integrate a high number of photosensitive elements into an array. As in CCDs, a matrix of pixels is build up out of photogates. Beyond the photon-generated charges by means of photogates as in CCDs, CMOS-based photosensors can make use of all photoconversion processes shown in section 2.2.1. They are integrated into a semiconductor which is n- and/or p-doped. Figure 2.24 outlines some possible solutions about how to construct a CMOS-based photosensor.

Figure 2.24: *Different CMOS image sensor types (Janesick 2004).*

One of the main advantages of this technology is the possibility to integrate circuits into the silicon. In contrast to CCDs where the charges are transferred across the whole sensor array to a single sense node (AD conversion), CMOS sensors integrate a sense node in every single pixel. Therefore, the charge-transfer loss is negligible. As it can be seen in Figure 2.24, the single pixels shown can make use of photodiodes (PD) and photogates (PG) as well as pinned photodiodes (PPD) and charge share (CS). Besides the possibility to integrate the different charge generation methods and the A/D conversion, CMOS technology is able to implement elements of higher abilities as well. This leads to so-called CMOS APS (Active Pixel Sensors). APS stands for the process of the integration of additional abilities into

the single pixel. Beyond advanced A/D conversion, controlled charge separation (sampling) and first processing steps have to be named.

The main disadvantage of CMOS sensors compared to CCDs is their higher fixed-pattern noise (FPN) due to several reasons (Lange 2000). The reduced optical fill factor (ratio of light-sensitive area to total pixel size) also has an impact on the quality of CMOS-captured data. Due to their pixel-integrated circuits, CMOS pixels have an optical fill-factor of typically $30 - 50\%$. CCDs reach nearly 100%. For the use in RIM systems, CMOS is basically preferred due to the ability of integrating smart circuitry.

2.3   Range Imaging Sensors and Realizations

For the distance measurement techniques outlined in section 2.1, a suitable sensor has to be found that combines the 1-D distance measurement with the 2-D coordinate measurement to a 3-D measurement system. Deumlich & Staiger (2002), Burnside (1971), Bolsakov et al. (1985), and Kahmen (1997) briefly mention standard methods for light-detection, whereas Ingensand (2003) describes some important 1-D distance measurement technologies more closely. Further on, the basis for the range imaging technology is to integrate a distance measurement system into an array. Then, it is possible to capture a whole 3-D scene (surface capturing) within a camera-like device. This range imaging principle is outlined in figure 2.25.
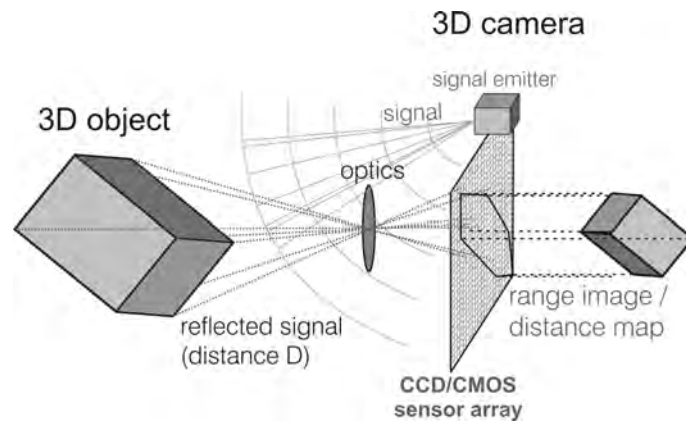
Figure 2.25: *Range imaging camera working principle. Modulated light is sent out by the signal emitter. This light is partly reflected by an object in the field of view back to the camera. The light is mapped onto the sensor array by optics. The distance D towards every object point corresponding to each pixel is calculated. Out of this distance map, the spatial environment (object) can be reconstructed.*

As it can be seen, the camera properties are extended in a way that distances towards object points corresponding to the single pixels are measured. It follows that a 3-D coordinate calculation of the mapped points is possible (see section 2.4). The spatial selectivity of the camera principle enables this. The data to be captured (beside color and/or intensity) have three dimensions. The camera itself, with its planar sensor, is able to capture only two dimensions (section 2.2). The remaining dimension can be introduced by means of measuring the distance to the mapped object point. What has to be carried out, therefore, is the implementation of a distance measurement technology (see section 2.1.1) into an array. A semiconductor array is chosen because of the high sensitivity of treated silicon towards electromagnetic radiation (compare section 2.2). One of the main advantages of RIM cameras besides their simultaneous acquisition mode is the absence of moving parts, as is the case with laser scanners. Moving part always run the risk of damages more than static ones. This section outlines some realizations of 3-D RIM cameras with their properties. In the following, some possible (and already implemented) structures are presented more closely. For a complete description, the referred literature is recommended. The systems

introduced here are civil systems. Military systems exist, but mostly with poor documentation due to strict limitations about their secret. Table 2.1 gives an overview about some of the existing RIM systems.

producer	products	ToF technology	pixel (max)	status
CSEM/Mesa (Switzerland)	SR-3000, SR-2	indirect	176 × 144	demo/user
PMDtec (Germany)	768-S, 1k-S, 3k-S, 19k	indirect ToF	160 × 120	demo/user
EPFL (Switzerland)		direct ToF	64 × 48	research
Canesta (USA)	diverse	indirect ToF	176 × 132	demo/user
ITC-irst (Italy)		dir. and ind. ToF	diverse	research
Shizuoka Univ. (Japan)		indirect ToF	176 × 132	research
3DV Systems (Israel)		dir./shuttered ToF		product
Matsushita (Japan)		indirect ToF	128 × 123	demo

Table 2.1: *Overview RIM sensor manufacturers (incomplete).*

2.3.1 Combined CCD/CMOS Technology

The first, more or less commercial, RIM camera available on the market was the SwissRanger™SR-2 (figure 2.26, left). This RIM camera was developed by Centre Suisse d'Electronique et de Microtechnique SA (CSEM) in Zurich. A closer description of the sensor's working principle can be found in Lange (2000), Spirig (1997), Spirig et al. (1997), Büttgen et al. (2004) and Oggier et al. (2004).
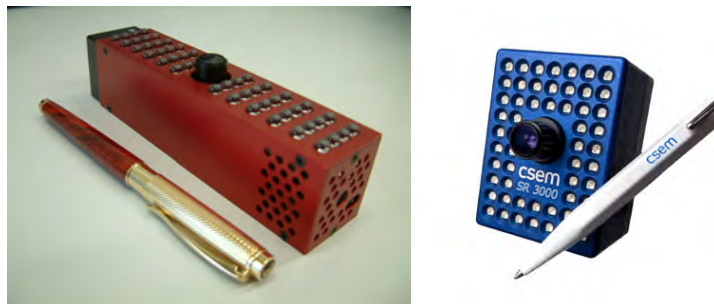
Figure 2.26:   Left*: SwissRanger SR-2. This version was mainly used for the experiments in this work.* Right*: The SwissRanger SR-3000 shown here is the follow-up generation of the SwissRanger SR-2.*

Selected specifications of the SwissRanger SR-2 can be found in table 2.2. The full specifications are listed in appendix A. The SR-2 was built for demonstration purposes. Therefore, different aspects are not fully developed. But, nevertheless, the full functionality of the sensor is available. Only a small number of devices were made.

Modulation Frequency	20 MHz
Non-Ambiguous Distance Range	7.5 m
Measured Demodulation Depth	40 %
Pixelfield	6.27 mm (39.2 μm x 160 $pixels$)
	6.80 mm (54.8 μm x 124 $pixels$)
Number of LEDs	48
Filter: Center Wavelength / Bandwidth	882.5 nm / 65 nm
LEDs: Wavelength of LEDs / Spectral Bandwidth	870 nm / 40 nm

Table 2.2:   *SwissRanger SR-2 Selected Specifications.*

As table 2.2 already indicates, the SR-2's working principle is based on the demodulation of light according to the phase-shift measurement principle pointed out in section 2.1.2 (indirect Time-of-Flight).

According to the number of photo charge storage sites in the semiconductor device, the different sensors can be distinguished. There are three possibilities for a phases difference measurement: 1-tap, 2-tap, and 4-tap working principle. For the full demodulation of the sinusoidal signal, usually four intensity measurements are needed (compare equation 2.5). These measurements are well-chosen when each differ by 90° in phase. For the 1-tap algorithm, the four measurements τ_0, τ_1, τ_2, and τ_3 are carried out sequentially. All these measurements with a certain integration time Δt differ by $90° + x \times 360°$ with $x \in \mathbb{N}$. Therefore, the measurements are distributed in time over more than one cycle. This means that even a slight change in the distance or the illumination results in a significant change in the measurement result. If at least two storage sites are available in the sensor, the 2-tap algorithm is applicable. With this it is possible to measure a series of two intensities in a row. Therefore, the measurements are carried out faster, but an offset remains between the two sets. This again results in a different result if a change in distance or illumination during the measurement exists. The SwissRanger SR-2 has two integrated storage sites and is therefore able to work in the 1-tap or 2-tap mode. Within this thesis, the sensor was operated in the 1-tap mode. The 4-tap algorithm avoids this effect to the greatest possible extent.

a) photogate and charge transfer   b) cross section and ideal charge transfer   c) timing diagram gate contacts
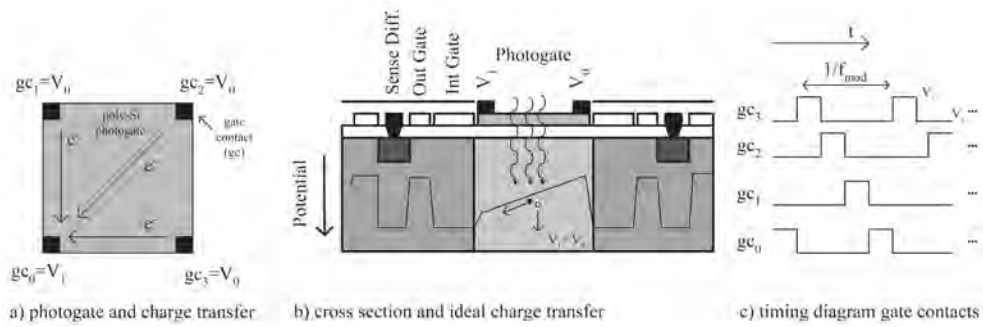
Figure 2.27: *Schematic and functionality of a drift-field pixel. Büttgen et al. (2004) introduced this kind of sensor. Incoming radiation generates charges which are separated into four integration gates. The charges integrated are an equivalent to the distance towards the object point the pixel refers to (section 2.1.1).*

Figure 2.27 outlines one possible realization of such an advanced sensor, proposed by Büttgen et al. (2004). It is a semiconductor structure that has the ability to separate charges very fast by means of *four* integration gates. The working steps are as follows:

- Incoming light separates charges in the depletion region.

- The induced potential field separates the electrons from the "holes".

- Differences in the voltage of the gate's corners cause the electrons to fluctuate to a wanted potential well created by the corresponding integration gate.

- The duration for each of the four in this case is one-fourth of the periodic time (not necessary as seen in figure 2.4).

- If enough charges are collected, the charges are transferred to the sense diffusion nodes.

- Charges are converted and measured in the electronic read out circuitry (CMOS).

- Calculation of the referred distance D (equation 2.5).

With this sequence, each pixel captures a part of the whole 3-D environment. In case of the SwissRanger SR-2, the high frame rate of up to 30 Hz, in combination with the high number of pixels (19840),

allows for a dense gathering of the surface in the camera's field of view. The SR-2 is designed as a slave component to the master computer. Therefore, the frame rate is mostly limited by the speed of the USB interface and the processing speed of the master.

Besides the ability to capture and to measure radiation with respect to a modulation frequency, the property to integrate the photo-generated charges over a certain integration time interval is decisive for the range measurement. As shown in section 2.1.2.2, the measurement interval Δt has to be defined. Beyond this, it is evident to integrate over a number of Δt to increase the number of charges and thereby increase the sensitivity of the system. As Lange (2000) has shown, the repetitive accumulating sampling increases the Signal-to-Noise Ratio. But in case of a highly dynamic scene, the possibility of saturation of the sensor has to be taken into consideration. The SR-2 samples the measurands with 16 *bit*. This gives a distance resolution of:

$$res_{dist} = 7.5 \; m/16bit = 0.1 \; mm \tag{2.12}$$

Investigations on the distance accuracy and the calibration of the distance measurement system can be found in section 3.3. The emitting system of the SR-2 consists of 48 NIR-LEDs. The specifications can be found in appendix A. NIR was chosen due to the invisibility. Especially in everyday applications like in-car and robot safety, visible flickering lights are not desired.

One of the main problems in RIM, especially in phase-shift-based methods, is the influence of the background illumination. A high background illumination (e.g. sunlight) very quickly results in a saturation of the pixels. A saturated pixel does not give any more information about the distance. To reduce the overall sum of impinging radiation power, an optical bandpass filter is mounted in front of the sensor. The center wavelength is chosen according to the radiation wavelength of the emitting system (compare table 2.2). In this way, most of the background radiation can be avoided to reach the sensor and, therefore, decrease the total amount of generated electrons without any distance depending information. However, according to Büttgen et al. (2005), the background illumination still reaches a ratio of 100 : 1 compared to the signal power.

In order to reduce the background illumination, several different circuits were implemented on the different RIM camera chips. In the case of the SR-2, no such methods were implemented. The follow-up version, the SwissRanger SR-3000, is equipped with such a system. As it can be seen in equation 2.5, only differences are needed for the calculation of the phase shift. Therefore, the background light does not have any impact upon the distance evaluation, except the precision. Background adds electrons to all storage sites equally (Oggier et al. 2005). This can be assumed due to the fact that there is no difference between the photoactive pixel sites with respect to the incoming light. This is true if the light is distributed without any systematics (e.g. without modulation near the modulation frequency). But due to the photon shot noise depicted in figure 2.6, the precision will become worse with increased background radiation. To avoid background illumination is therefore a better alternative than all the methods used to increase its impact. In case of the SwissRanger SR-3000, a circuitry is implemented which subtracts within a pixel the electrons added equally to every storage site by the background. As a result the distance measurement is possible even under strong background radiation. If the background is measured once and then subtracted equally from all $c(\tau)$, there is no loss of precision in the pure distance calculation process. But the increase of photon shot noise with higher background remains evident.

According to Büttgen et al. (2005), the dynamic range DR can be calculated by means of

$$DR \; [dB] = 20 \cdot \log_{10} \left(\left(\frac{R_{max}}{R_{min}} \right)^2 \cdot \frac{\delta_{max}}{\delta_{min}} \right) \tag{2.13}$$

In case of the minimal and the maximal distance that has to be measured, $R_{min} = 0.2 \; m$ and $R_{max} = 7.5 \; m$, and the reflection coefficients, $\delta_{min} = 5\%$ and $\delta_{max} = 100\%$, the dynamic range will become as high as 89 dB. This means a factor of about 1 : 28000 between the weakest and the strongest reflections. A second way to avoid the saturation of the pixels but to keep data with low corresponding reflectivity is

to regulate the integration time according to the intensity. This means stopping integration of additional electrons if saturation is nearly reached. The SwissRanger SR-3000 is equipped with such a functionality.

2.3.2 Photonic Mixer Device (PMD) in CMOS Technology
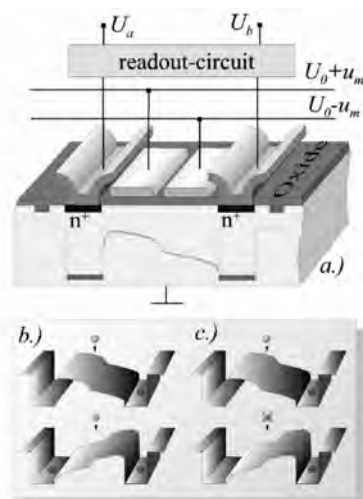
Figure 2.28: *Schematic and functionality of a PMD pixel Heinol (2001).*

At the same time the SR-2 was developed, another RIM camera was brought to concept. Due to their similar backgrounds, which is discussed in the work of Lange (2000), the Photonic Mixing Device (PMD) and the SwissRanger sensors are based on a nearly equal working principle. The main difference, beyond chip design, is the complete production in a CMOS process. Whereas the SR-2 uses CCD technology for the gates, all PMDs just use CMOS. PMD sensors use finger-structured photogates. This helps in using increased modulation frequencies simultaneously together with a scalable pixel size to increase the optical fill factor.

Figure 2.29: *Casing of the PMD Camera.*

But again, due to their histories, both principles are very similar. As figure 2.28 outlines, the incoming radiation separates charges, which are driven to one of the integrating gate buckets. The decision as to which gate is chosen is superposed by the modulation frequency. As outlined by Heinol (2001), the PMD sensor works with the 2-tap principle outlined in section 2.3.1. But Schwarte et al. (1997) already proposed an four-quadrant diode for the 4-tap ability.

Figure 2.29 shows the casing of the PMD array sensors. Like the SR-2, the PMD system uses a high number of LEDs to fulfill the optical requirements. Lange (2000) has pointed out that a sufficient optical output power is needed to reach a certain level of distance measurement accuracy. This level lies
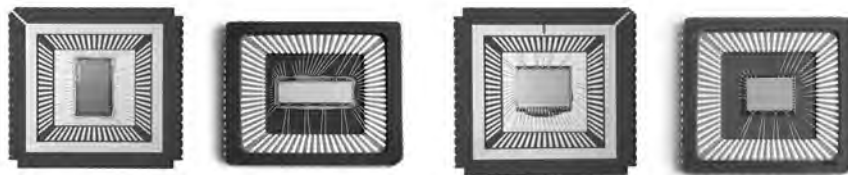
Figure 2.30: *Overview of the different PMDTec Products: PMD 768-S 3D with Active SBI, PMD 1k-S 2 3D with Active SBI, PMD 3k-S 3D with Active SBI and PMD 19k High Resolution 3D Video Sensor Array (from left to right).*

somewhere at about 700 mW optical output power for a distance of about 7.5 meters (relating parameter, Lange (2000)). This high power can only be provided by high-energy diodes, laser sources or, as realized in the SR-2 and PMD cameras, with a bunch of LEDs. The main drawbacks of such a configuration are as follows:

- LEDs normally have a certain beam divergence (in case of the SR-2 about 22°) and non-constant radiation power over this field of view. Therefore, the use of pure LEDs without any additional optics (except the normal cover dome) leads to illumination non-uniformity. Sections 3.3.4 and 3.3.3 outline this problem more closely.

- Because of the array-like configuration, no clear reference point for the emitting of radiation exists. The basic idea for the working principle of RIM prerequisites a point-like light source. Otherwise a non-uniform phase front occurs. This leads to a lower contrast due to the different time-shifts (offsets in distance) from every LED–object–sensor set.

- All the LEDs have to be triggered simultaneously. Different driven LED result in a distance shift for this single LED and, therefore, a decreased contrast as well.

Figure 2.30, in combination with table 2.3, outlines some realizations of the PMD principle into sensors. As it can be seen, many different sensor dimensions can be implemented. Of course, this is possible for all RIM sensors based on CMOS (section 2.3.1, 2.3.2, and 2.3.3). The scalability is one of the main advantages of the RIM technology. Therefore, an adaption to many different applications is guaranteed.

	PMD 768-S 3D	PMD 1k-S 2 3D	PMD 3k-S 3D	PMD 19k
Array Format	24 × 32	64 × 16	64 × 48	160 × 120
Optical Format	1/2″, 16 : 9	2/3″, 3 : 1	1/2″, 4 : 3	1/2″, 4 : 3
Eff. Image Area [mm]	6.75 × 3.73	9.94 × 3.37	6.4 × 4.8	6.4 × 4.8
Pixel Size [μm]	210.8 × 155.3	155.3 × 210.8	100 × 100	40 × 40
Fill Factor (FF)	42%	42%	32%	31%
Dynamic Range [dB]	78	78	74	65
DR Inc. by SBI [dB]	50	50	50	na

Table 2.3: *PMD sensors and selected specifications.*

Some of the PMD sensors are equipped with a suppression of background illumination (SBI) circuitry. The SBI subtracts the uncorrelated signal, added equally by background illumination to all photon-generated electron storage sites and, therefore, avoids the pixel to reach the saturation level. Figure 2.31 shows the principle in the case of the CMOS device. By means of charge comparison, the background corresponding electrons are discharged. The dynamic range of a typical PMD pixel can be increased in
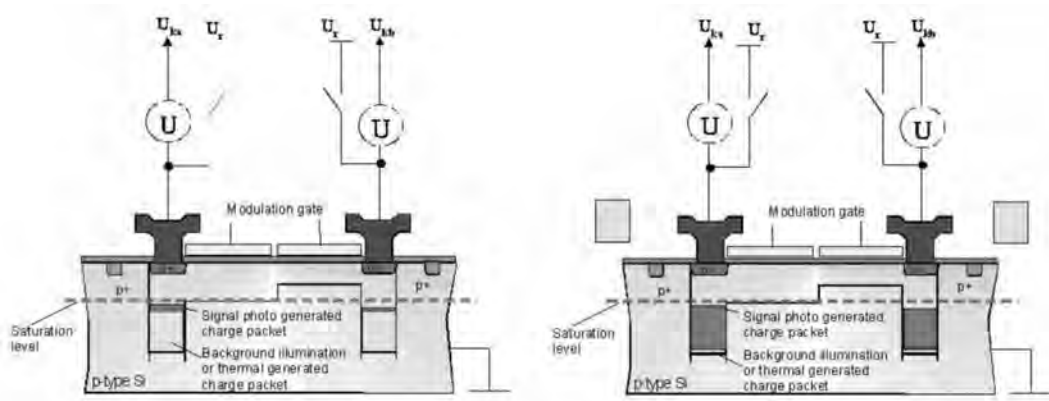
Figure 2.31: *PMD suppression of background illumination (SBI) circuitry*

this way by a factor of 300 or 50 dB. This technology can be compared to the background subtraction methods implemented in the SR-3000 sensors.

Another important task to increase the accuracy of the distance measurements is to increase the emitted optical power. The simplest way is to increase the number of LEDs or to use stronger light sources, for example. But due to restrictions in power consumption as well as eye safety, this is only possible in a very limited range. Normally, LEDs are driven in continuous wave modulation. A very effective way is to drive the LED in a so-called *burst mode*. This means that the LEDs are driven with a very high optical output for very short pulses (peak power) instead of a continuous modulation. Within the burst, modulation the average of the optical power over the time and, therefore, the number of photon-generated electrons remains constant. But fewer noise electrons are collected (Möller et al. 2005).

2.3.3   Arrays of Single Photon Avalanche Diodes in CMOS Technology

The Avalanche Photodiode array (APD array) is a third way to construct a RIM sensor array. Figure 2.32 (left) points out the circuit principle and a photograph of a realization (right) done by the Federal Institute of Technology Lausanne (EPFL) (Niclass et al. 2005). It is built up in CMOS technology. Figure 2.15 already showed a lateral cut through such an APD. As it can be seen, the multiplication region is guarded by a ring of p-doped silicon against neighboring regions and, therefore, falsely sensed electrons coming from elsewhere than the wanted sensing region. Premature breakdown is avoided.
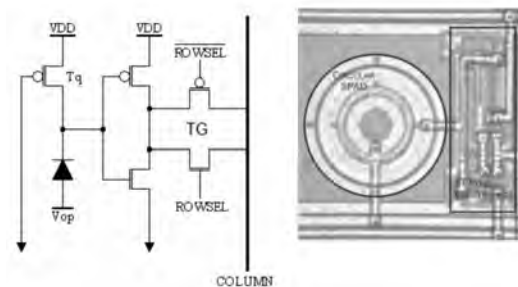
Figure 2.32: *Circuitry and photograph of avalanche photodiode in CMOS technology (Niclass et al. 2005).*

The active area (80 μm^2) of the digital pixel just makes about 1% of pixel size of 58 μm · 58 μm = 3364 μm^2 (figure 2.33). The main advantage of the APD array is given by its very low power requests towards the incoming light. Even single photons can be measured. Therefore, inexpensive low-power lasers are sufficient. In the case of the outlined RIM SPAD sensor in this chapter, a laser source (635 nm)

with a peak power of 100 mW (average 750 μW) and a pulse width of 150 ps was used. To reach a homogenous illumination of the whole scene, the laser was intentionally uncollimated.

One of the main advantages of SPADs is that they are not limited by analog noise and device mismatch in the readout circuitry (Niclass et al. 2005). It has also experimentally been shown that they are completely free of crosstalk effects (electrical and optical crosstalk < 0.01%), which is therefore lower than DCR.
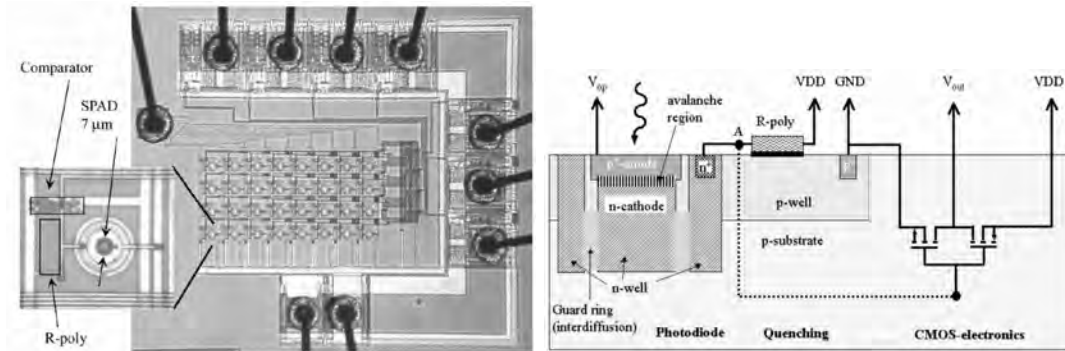
Figure 2.33: *Left side shows a photograph of the SPAD array from EPFL. On the right, a lateral cut through the pixel is shown.*

Niclass et al. (2005) also reports of the successful implementation of an external low-cost CMOS time discriminator. In operation, a timing uncertainty of 300 ps was measured. In order to reach better results, an averaging of measurements is unavoidable. With a measuring rate of 50 kHz, the exposure time for a single mean measurement is reported to be 200 ms. Accuracies in the millimetric range are expected. But in the case of the described demonstrating product, the pixels were driven in serial mode in which a pixelwise and differential distance measurement was performed. In future, all pixels will be driven in parallel mode.
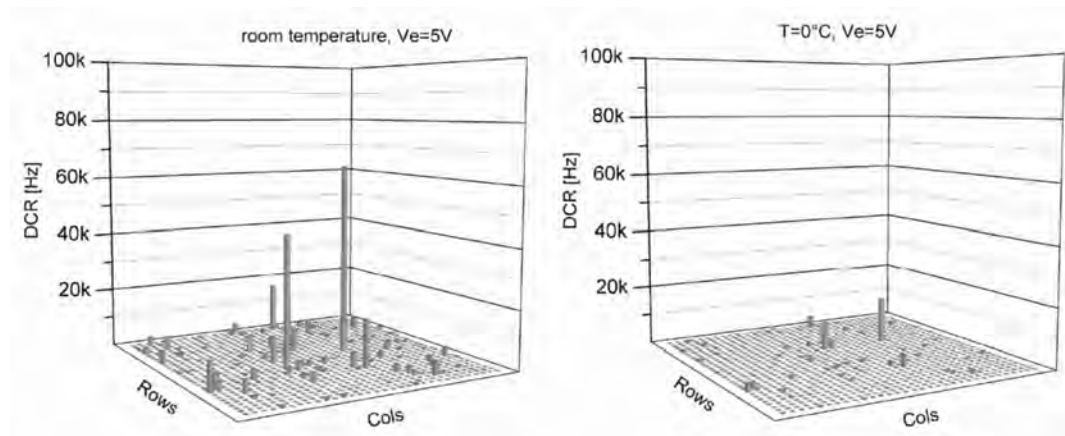
Figure 2.34: *DCR of an EPFL SPAD array.*

Figure 2.34 shows the DCR dependency of an SPAD with respect to the temperature. As it can be seen, the DCR drops significantly at lower temperatures. For this work an SPAD based-sensor was not available. Details about this sensor technology can be found in the corresponding literature.

2.3.4 Shuttered Time-of-Flight

A completely different, direct Time-of-Flight approach for the generation of range images was introduced, for example, by Gvili et al. (2003). Figure 2.35 indicates the basic principle. A radiated light pulse is

reflected by the object scene back to the camera. In front of the camera, a fast GaAs (optical) shutter chops the incoming light. Ever, small period of acquisition time, with respect to the speed of light, corresponds to a distance interval. Therefore, with one light pulse, the amount of energy of the certain distance interval is mapped on the camera. The relative amount of light (gray value) mapped on the sensor is then a measure for the distance between the specific pixel and the object. Because no such sensors were investigated, this RIM approach is not followed in detail, here. The reference literature is recommended, though. The main advantage of this approach is the usability of standard digital cameras.

Figure 2.35: *Depth keying principle. A scene is illuminated with a light pulse. The incoming signal is captured only for a short period of time. The impinging optical energy then is related to a specific distance within this interval. Thus, the chopping of the time domain leads to distance interval mapping, sequentially.*

2.4 3-D Coordinate Measurement Principle

Finally, the calculation of 3-D coordinates based on range imaging data will be explained for the sake of completeness. Therefore, a simplified model is used. As an output, three different data sets are produced by a 3D RIM camera:

- distance map or range image,

- intensity map, and

- amplitude map.

The distance map is a picture-like array-structure with distance information instead of intensity (intensity map) or color data. Due to the use of optics, the environment is mapped onto the sensor array. Therefore, every pixel measures the distance toward the corresponding point in the 3-D space. This condition is demonstrated in figure 2.36 in detail. Because of the calibration process explained in chapter 3, a pinhole camera model is sufficient.
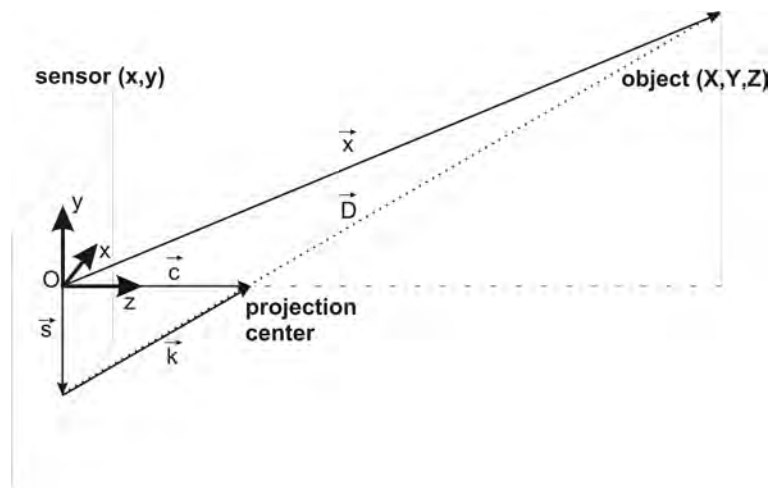
Figure 2.36: *Simplified model for the calculation of 3-D coordinates out of the measured distance map (SR-2). The coordinate system for the SR-3000 has been modified: $x = -x$ and $y = -y$.*

As it can be seen, the object coordinates X, Y, and Z are calculated out of the sensor coordinates x_s and y_s as well as the camera constant c (for first calculations $c \approx f$) and the measured distance D, which is stored in the distance map:

$$\vec{c} = \begin{pmatrix} 0 \\ 0 \\ c \end{pmatrix} \tag{2.14}$$

$$\vec{s} = \begin{pmatrix} x_s \\ y_s \\ 0 \end{pmatrix} \tag{2.15}$$

$$\vec{k} = \vec{c} - \vec{s} = \begin{pmatrix} -x_s \\ -y_s \\ c \end{pmatrix} \tag{2.16}$$

$$\vec{X} = \vec{s} + \vec{d} = \vec{s} + D \cdot \vec{k} \cdot \frac{1}{|k|} = \begin{pmatrix} x_s \\ y_s \\ 0 \end{pmatrix} + \begin{pmatrix} -x_s \\ -y_s \\ c \end{pmatrix} \cdot \frac{D}{\sqrt{x_s^2 + y_s^2 + c^2}} \tag{2.17}$$

The precision of the calculated coordinates with respect to the different influencing parameters follows the law of error propagation:

$$\mathbf{S}_{XX} = \mathbf{F}\mathbf{S}_{LL}\mathbf{F}^T \tag{2.18}$$

The diagonal elements of $\mathbf{S}_{XX}$ are the variances s_x^2, s_y^2, s_D^2 and s_f^2. $\mathbf{S}_{LL}$ contains the input variable variances and covariances. Matrix $\mathbf{F}$ contains the derivatives of the coordinates according to equation 2.17

$$\mathbf{F} = \frac{\partial \mathbf{X}}{\partial \mathbf{L}} \tag{2.19}$$

The derivatives were calculated numerically for the following estimation. Correlations between x_s and y_s were set to zero. Table 2.4 displays some interesting constellations. The pixels chosen were in the outer corners of the sensor array ($x_s = 3.136\ mm$ and $y_s = 3.398\ mm$). The standard deviations of x_s and y_s were set alternating to 1 $pixel$ and 0.5 $pixel$. The precision s_f of the focal length was fixed to 0.05 mm.

$\mathbf{sx_s}$ $[mm]$	$\mathbf{sy_s}$ $[mm]$	$\mathbf{D}$ $[m]$	$\mathbf{s_D}$ $[m]$	$\mathbf{X}$ $[m]$	$\mathbf{s_X}$ $[m]$	$\mathbf{Y}$ $[m]$	$\mathbf{s_Y}$ $[m]$	$\mathbf{Z}$ $[m]$	$\mathbf{s_Z}$ $[m]$
$c = 0.008\ mm$
0.0392	0.0548	7.5	0.01	-2.542	**0.031**	-2.754	**0.041**	6.493	**0.022**
0.0196	0.0274				**0.019**		**0.024**		**0.016**
0.0392	0.0548	2.0		-0.676	**0.009**	-0.732	**0.011**	1.732	**0.010**
0.0196	0.0274				**0.006**		**0.007**		**0.009**
0.0392	0.0548	7.5	0.02	-2.542	**0.032**	-2.754	**0.041**	6.493	**0.026**
0.0196	0.0274				**0.020**		**0.024**		**0.022**
0.0392	0.0548	2.0		-0.676	**0.011**	-0.732	**0.013**	1.732	**0.018**
0.0196	0.0274				**0.008**		**0.010**		**0.018**
$c = 0.012\ mm$
0.0392	0.0548	7.5	0.01	-1.826	**0.023**	-1.978	**0.031**	6.998	**0.014**
0.0196	0.0274				**0.013**		**0.017**		**0.011**
0.0392	0.0548	2.0		-0.485	**0.006**	-0.525	**0.009**	1.866	**0.010**
0.0196	0.0274				**0.004**		**0.005**		**0.009**
0.0392	0.0548	7.5	0.02	-1.826	**0.023**	-1.978	**0.031**	6.998	**0.021**
0.0196	0.0274				**0.014**		**0.017**		**0.020**
0.0392	0.0548	2.0		-0.485	**0.008**	-0.525	**0.010**	1.866	**0.019**
0.0196	0.0274				**0.006**		**0.007**		**0.019**

Table 2.4:   *Precision of object coordinates derived from RIM data.*

As expected, the precision of coordinates calculated near the camera is better than those farther away. This is a result of the intercept theorem. Due to the optical way of the rays in the optics, the distance measurement precisions mainly respond to the Z precision, of course. A very important role for the precisions of X and Y is the precision of the coordinate measurement on the chip, that is, in the distance map or the picture.

The enormous impact of the camera constant on the accuracy is pointed out in figure 2.37. Due to different reasons, mainly internal calculative reasons, the coordinate system for the SR-3000 has been used in a modified manner: $x = -x$ and $y = -y$. Thus, the z-axis remains the same.
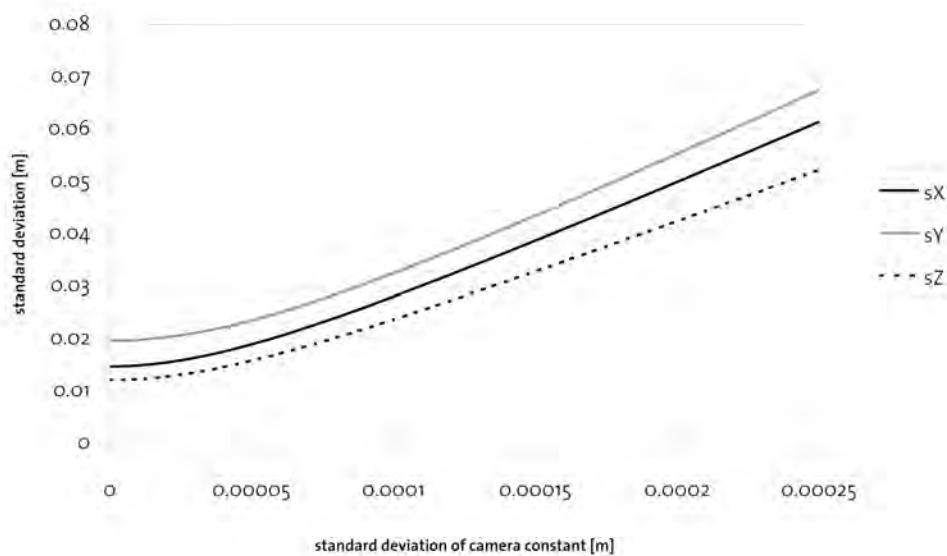
Figure 2.37: *Impact of camera-constant accuracy on coordinates ($x = 3.136$ mm, $s_x = 0.5$ pixel, $y = 3.398$ mm, $s_y = 0.5$ pixel, $D = 7.5$ m, $s_D = 0.01$ m, $c = 0.008$ m). If the camera constant is not known properly, the impact on the coordinate´s precision is not negligible.*

Chapter 3

Investigation and Calibration

In order to obtain a complete description of a measurement process (implemented into a product), it is necessary to outline the method (functional model) itself as well as the statistical characteristics (statistical model). Some of the quality characteristics are accuracy, precision, and reliability. Efforts have been undertaken to standardize these descriptions by means of normative regulations to hand out guidelines for the producer and especially the customer of the certain products (DIN ISO 17123-5:2005 2005). These regulations are supposed to verify the quality of the measurement system. The verification process is mostly indicated as *calibration* (cf. section 3.1).

A calibration mainly consists of the determination of possibly existing systematic deviations between true and measured values as well as the determination of statistical model parameters of the system. In most cases a holistic description with respect to the influencing parameters (e. g. temperature and reflectivity) cannot be given. Therefore, unknown influences can only be embraced within the stochastic model. In order to gain best results, the systems' functional model is gradually expanded until the stochastics represent the limiting factor. In case of actual RIM cameras, the theoretical limitations, given by the nature of the process (opto-physical limitations, cf. section 2.1.2.2), are nearly reached. In order to derive the accuracy of actual range imaging cameras, the different influencing parameters that affect the measurements have to be investigated. Two different cameras were investigated for this purpose: the SwissRanger SR-2 as well as the SR-3000. Therefore, for some aspects, a comparison between both systems is possible. Some investigations about these cameras can be found in Gut (2004) and Hempel (2007), exemplarily. Additionally, a PMD 3k-S camera was briefly available for further analysis. However, only a few aspects about this camera can be found in this work.

The goal of this chapter is mainly to introduce a functional calibration model for use with RIM cameras like the SwissRanger$^{\text{TM}}$ SR-2 and SR-3000 and to give an insight into the stochastical model. Due to the high number of influencing parameters with partially high correlation, the explored properties of the system will be helpful in better understanding the functioning of RIM cameras. Should a suitable calibration model be found, the remaining stochastic deviations could be examined in order to give a quantification of the system's potential. In sections 3.2 and 3.3, the different system components, imaging sensor and distance measurement system, are mostly calibrated serially. In section 3.4 a general integral calibration approach for 3-D coordinate measurement systems, like RIM cameras, is introduced. Section 3.5 concludes the results and limitations of the calibration approaches.

Figure 3.1 gives an overview of some possibilities of calibration steps, i. e. how to correct the measurements of RIM cameras. It starts with the raw measurements distance and pixel coordinates.[1] Different ways of generating calibrated data are possible and can partially be combined. All calibration procedures start with raw distance data and pixel coordinates as well as amplitude information. The left in combi-

---

[1] These measurements are not the primary measurements in fact. The original raw measurements are the intensities (or run times at SPAD systems) measured by the sensor pixels. But, normally, the derived information distance and pixel coordinates are the basic information the user is interested in.
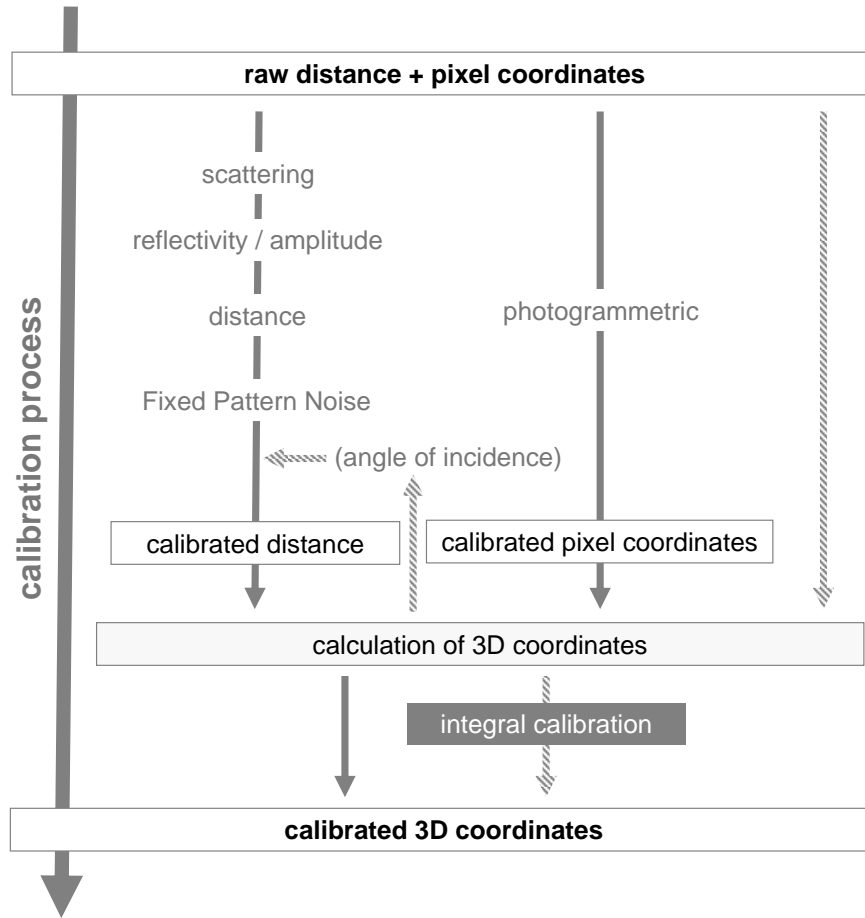
Figure 3.1: *Overview of the calibration approaches for RIM cameras.*

nation with the middle path indicates the component-wise calibration of the distance measurement data and the image distortion calibration. The distance data are calibrated with respect to the scattering, the reflectivity and amplitude, the distance itself (linearity), the Fixed-Pattern Noise and eventually the angle of incidence. The image distortions are calibrated by means of photogrammetric camera calibration approaches. The photogrammetric camera calibration of the SR-2 and the SR-3000 will be shown in section 3.2 and the distance data calibration in section 3.3. These steps are known as *component calibration*. On the right path, no calibration is performed on the principle measurement data. After the calculation of 3-D coordinates, with calibrated or uncalibrated data, the *system calibration* or *integral calibration* can be done[2]. This approach treats the secondary output of the camera, which are 3-D coordinates. The correction of data, which uses the 3-D data is also known as *black box calibration* and corrects the 3-D coordinates with respect to their spatial occurrence. All approaches can be combined and finally lead to calibrated 3-D coordinates. The main task is to reduce systematics within the original data.

The following sections will deal with the determination of the introduced calibration rules or approaches.

---

[2]The term *integral calibration* has been chosen, because this approach inherits several calibration aspects. It is also known as *system calibration*. It can be designed as a 3D LUT calibration or as a functional model. With respect to photogrammetric calibration aspects, an *integral calibration* would be considered to be a typical camera calibration which includes the measured distances into the calibration procedure.

3.1 Definitions

First of all, some specific terminology used for the investigations in this work has to be outlined. Many different opinions for technical terms exist. Thus, normative regulations were strived for in order to bring clearness. First, *calibration* has to be defined. One of these norms is DIN EN ISO 9001:2000 (2000). Measuring equipment has to be...

> *... calibrated or verified at specified intervals, or prior to use, against measurement standards traceable to international or national measurement standards; where no such standards exist, the basis used for the calibration or verification shall be recorded; ...*

It becomes clear that *calibration* has to deal with deviations of the measurements from standards. It is assumed that in case of 3-D measurement systems, like RIM cameras, the standard is a metrical reproduction of the geometrical (plus radiometry, plus time) reality. However, the explicit definition is given by ISO VIM (2004):

Calibration is an ...

> Definition (a):
> *... operation establishing the relation between quantity values provided by measurement standards and the corresponding indications of a measuring system, carried out under specified conditions and including evaluation of measurement uncertainty.*

> Definition (b):
> *... operation that establishes the relation, obtained by reference to one or more measurement standards, that exists under specified conditions, between the indication of a measuring system and the measurement result that would be obtained using the measuring system.*

> > *NOTES : The relations referred to in definitions (a) and (b) can be expressed by calibration diagrams, calibration functions, or calibration tables. ...*

These definitions show that the basic requirement is the comparison between standards and measurements. In order to fulfil the demands of users of measurement systems, the definition is extended in such a way that the correction of the measured data is included in the calibration process.

Further, the terms *accuracy* and *precision*, which are used within this work very often, have to be defined. ISO VIM (2004) with respect to ISO GUM (1995) already gave detailed definitions:

> *Accuracy:*
> *closeness of agreement between quantity values obtained by measurement and the true value for the measurand*

> *Precision:*
> *closeness of agreement between quantity values obtained by replicate measurements of a quantity, under specified conditions*

Nevertheless, the definitions used for this work are given here and digress into the common usage of the terminology. The definition of the accuracy does not allow for an expression as a numerical value (ISO VIM 2004). But here, for the investigations of RIM cameras, accuracy is described as the root mean square (RMS), which gives a partially meaningful representative (compare definition at Schulz (2007)):

$$RMS = \sqrt{\frac{1}{n} \sum_{i=1}^{n} (\tilde{x} - x_i)^2} \tag{3.1}$$

where n is the number of measurements, $\tilde{x}$ the true or nominal value, and x_i the single realization, the measurements. Thus, the demand for the integration of the nominal value is partially fulfilled. Another

understanding of the accuracy is given in equation 3.2. It just deals with the offset between the nominal value and the measured mean without further statistical measure:

$$\delta = \tilde{x} - \bar{x}. \tag{3.2}$$

where again $\tilde{x}$ is the nominal value and $\bar{x}$ the mean of the measurements. In many cases the nominal value cannot be known or is just known one or two orders better than the measurement is. But in order to give a measure of the variation of a certain measurement, the precision is defined in accordance with ISO VIM (2004) as the empirical standard deviation:

$$s \quad = \quad \sqrt{\frac{1}{n-1} \sum_{i=1}^{n} (\bar{x} - x_i)^2} \tag{3.3}$$

$$\bar{x} \quad = \quad \frac{1}{n} \sum_{i=1}^{n} x_i \tag{3.4}$$

where n is the number of measurements, $\bar{x}$ is the mean value of the measurements, and x_i is the single measurement. Thus, s is the empirical standard deviation of a single measurement. If the measurements are distributed according to a Gaussian distribution, the standard deviation of the mean value decreases with a factor of $\frac{1}{\sqrt{n}}$. This topic is analyzed in closer detail in section 3.3.3 for the distance measurements of the RIM cameras.

3.2   Photogrammetric Camera Calibration

A vital prerequisite for the use of cameras as measurement instruments is the determination of the correct geometrical dependencies between the pixel coordinates and the object coordinates with respect to the optical system. Image coordinates have direct impact on the derived 3-D object coordinates measured by the RIM camera (cf. equation 2.17). In most cameras, complex optics are used that do not match the simplicity of the pinhole camera model. Additionally, because of distortions of the optics and inaccurate mounting, errors are present. These errors can be determined by means of a photogrammetric camera calibration. As RIM cameras primarily are based on digital imaging technology, a photogrammetric camera calibration is taken into account. Various methods are known. Remondino & Fraser (2006) outline some aspects of the different approaches. Of high importance for the calibration is the introduction of rotated camera positions. The photogrammetric camera calibration used in this work for the SR-2 and the SR-3000 is based on the method presented by Brown (1971). This includes a perspective geometrical model and is performed by means of a bundle adjustment. Mainly four parameter sets have to be determined:

- The camera constant c of the optics has to be derived.

- The principle point (x_P, y_P), which describes the offset between the center of the sensor and the perpendicular projection of the principle point, has to be known.

These two aspects are declared as the *inner orientation*. Additionally, these parameters can be extended by the distortions of the optics:

- In case of radial distortions of the lens, which cause failures in the calculation of 3-D coordinates as well, distortion parameters (K_1, K_2, K_3) have to be found (parameters according to Brown (1971)).

- Decentral distortion parameters (B_1, B_2), also known as (P_1, P_2), as well as the scaling sc_x and the sheer factor sh_y are calculated.

Due to the low resolution of the sensor, the specification of the coefficients of decentering distortions is not followed in the case of the SR-2.

Caused by the different technologies implemented in the SR-2 and the SR-3000, separate calibration procedures were used. The internal pixel coordinate systems differ as well as the external coordinate system, which holds the derived 3-D coordinates. Thus, the photogrammetric camera calibrations for the SR-2 and the SR-3000 are described separately with respect to the different approaches in the following.

3.2.1   SR-2
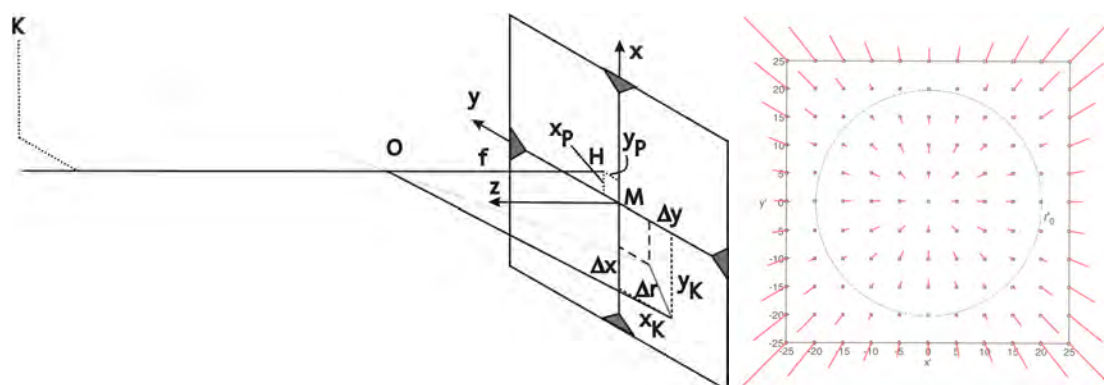
Figure 3.2: *Inner orientation (left) and effect of radial distortions (right) similar to Luhmann (2000) (adopted to SR-2 coordinate system definitions).*
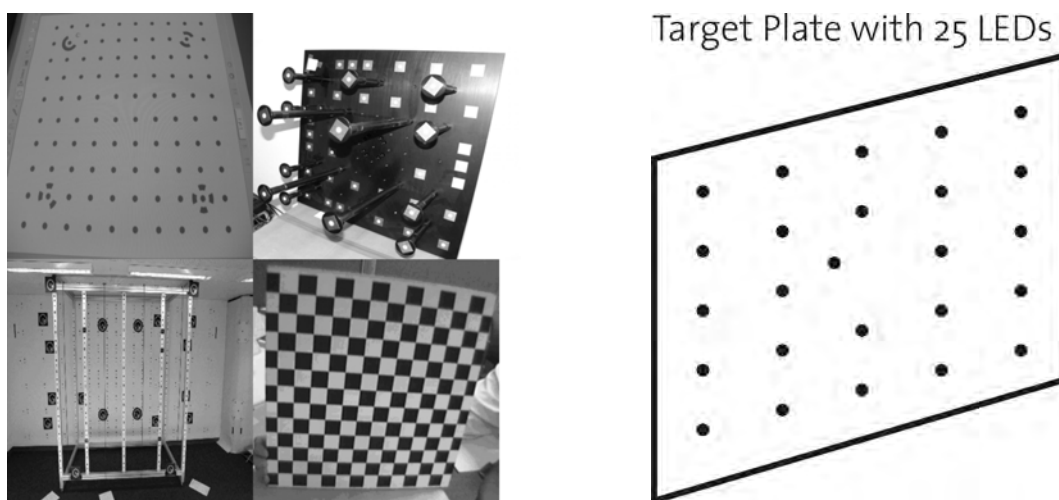
Figure 3.3: *Different calibration test fields usable for a photogrammetric camera calibration (left). In the case of the SR-2 these test fields cannot be used adequately due to the low lateral resolution of the sensor. Therefore, another solution had to be found. On the right, a planar test field structure for the photogrammetric calibration of the SR-2 can be seen. The LEDs can be extracted from the SR-2's intensity data very easily.*

First, the orientations of the axes of the internal coordinate system of the SR-2 have to be defined. Figure 3.2 shows the geometrical definition of the inner orientation parameters (left) and the effect of the radial distortion parameters on the image coordinates (Luhmann 2000). The calculation of the calibration parameter set can be done by means of a photogrammetric camera calibration. Gruen & Huang (2001) depict the least-squares adjustment in combination with the bundle block solution for the estimation of the calibration parameters in closer detail. Maas (1997) also gives some insight into the various calibration

procedures. The setup for the images needed for the calibration, as well as other conditions, are specified in Remondino & Fraser (2006) more closely.

Second, in order to calibrate the SR-2, a suitable calibration test field had to be found. Figure 3.3 (left) displays four different standard camera calibration test fields used in photogrammetry. However, the low resolution of the SR-2 does not allow for an automated and precise extraction of the target coordinates out of the intensity image without intensive investigations. The small size of most target points is a drawback, as well. Therefore, another solution had to be found. Kahlmann et al. (2006) already reported on the test field and the results of a calibration, as shown in the following.
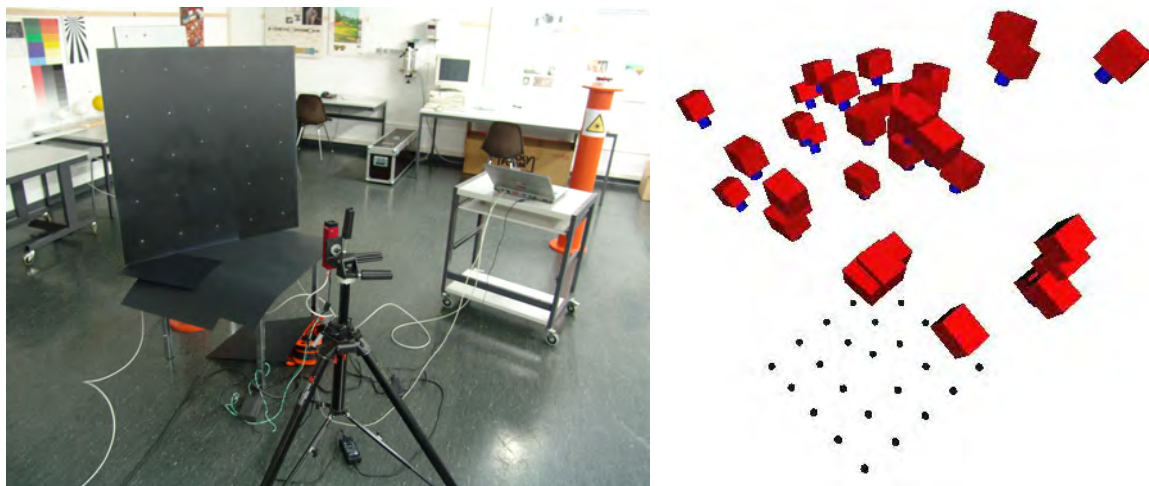
Figure 3.4: *Measurement setup for the photogrammetric camera calibration of the SR-2. The camera positions, calculated within the calibration, can be seen on the right. A 25 NIR-LED planar target plate was used. The LEDs can be found very easily in the intensity image.*

A suitable test field was developed. Figure 3.3 (right) shows a simple planar test field with 25 NIR-LEDs. Because of the high intensity of the LEDs, their image coordinates can be found very easily by means of threshold and centroid operators within the intensity image of the SR-2. These image coordinates are introduced into a bundle block adjustment, which contains the desired calibration parameters as unknowns.

Figure 3.4 displays the measurement setup and the camera positions used for the calibration. Besides variant positions and distances toward the target plate, the orientation of the camera was changed between the positions to fulfill the recommendations summed up by Remondino & Fraser (2006). The introduction of positions with a rotated camera is evident for reliable solutions of the calibration. The results of the calibration are depicted in table 3.1.

Parameter	Value	Standard Deviation
Camera Constant c	$7.656 \ mm$	$0.136 \ mm$
Principle Point x_P, y_P	$-0.1158 \ mm$, $0.1051 \ mm$	$0.068 \ mm$, $0.067 \ mm$
Radial Distortion K_1	$-2.388e - 3$	$0.78e - 3$
Radial Distortion K_2	$1.286e - 4$	$0.41e - 4$
Radial Distortion K_3	0.0 not significant	

Table 3.1: *Photogrammetric Calibration Parameters for the SR-2*

The derived calibration parameters allow for the correction of the measured data and the calculated three-dimensional coordinates. The use of a planar test field certainly is a drawback for the photogrammetric camera calibration. But in order to enable the extraction of the correct targets with the cor-

responding identification tags, a planar target is advantageous. However, the introduction of rotated camera positions as well as the well-chosen intersection angles and the high number of correlating rays within one target help to avoid strong dependencies between the different calibration parameters. Especially the usage of higher convergence angles helps to reduce correlations between P_1, P_2, and x_P, y_P (Remondino & Fraser 2006).

3.2.2   SR-3000

The test field used for the calibration of the SR-2 cannot be adapted to the calibration process of the SR-3000 without modifications. Due to the background radiation suppression of the SR-3000 (cf. section 2.3.1), the NIR-LEDs of the test field are not visible within the amplitude image (remember: with the SR-3000, the amplitude image and the intensity image are equal, due to the suppression mode). The main disadvantage of standard test fields is the small size of the target points. Thus, they cannot be extracted from the images precisely.

One special target was built for the calibration of the SR-3000. The test field is nearly the same as the one used for the calibration of the SR-2. Figure 3.5 shows the used test field. A black aluminium plate was equipped with white labels with a diameter of 11.7 *cm*. On the one hand, the targets can be found more easily because of the flat test-field shape, but on the other hand, rotations and well-distributed camera positions have to be chosen carefully. In order to reduce the influence of photon shot noise, which causes scattering in the amplitude image as well, the integration time was chosen with a high enough size: 100 [*dec*].
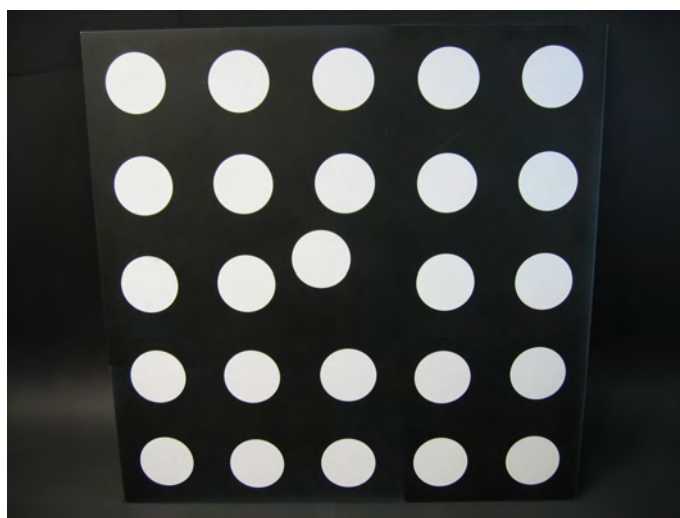
Figure 3.5: *Calibration test field for the photogrammetric calibration of the SR-3000. A black colored aluminium plate with* 25 *white circles with a diameter of* 11.7 *cm was chosen.*

The computations for the following analysis were done mainly by means of the OpenCV library, which is freely available on the internet (Intel Corporation 2006). The calibration, using a least squares bundle adjustment, was performed by the Australis©software package published by Photometrix Pty Ltd.

Figure 3.6 (left) displays a typical amplitude image of the calibration test field. It becomes clear that the amplitude decreases with respect to the distance from the image center in a radial manner. This is caused by the emitting characteristics of the LEDs, the decreasing angle of incidence (cf. 2.1.2.2), and the optics. Sections 3.3.4 and 3.3.6 go into more detail. In order to reduce these influences, the image was homogenized with respect to the amplitude. Thus, a blackboard was captured (cf. figure 3.6 (center)). This blackboard image was scaled by means of experiments until good results for the homogenization were reached. Mathematically, this was done by a multiplication of the specific amplitude image with the blackboard scale image. Figure 3.6 (right) shows the image being used for further analysis.

Figure 3.6: *Processing of amplitude images of the photogrammetric calibration test field from the SR-3000 in order to reduce the decreasing amplitude with an increasing radial distance from the center of the image: original amplitude image (left), blackboard image (center), and the processed image for use in further analysis (right).*

In order to enhance the targets in contrast, the edges of the round target dots are processed by means of a Laplace filter. The Laplace image (b/w) is afterwards filtered with a Gaussian filter (7×7) and finally both images are combined. Figure 3.7 clearly depicts this (the Gaussian filtered image is not shown here). The homogenized image is displayed on the left, the Laplace image in the middle, and the combined one on the right.
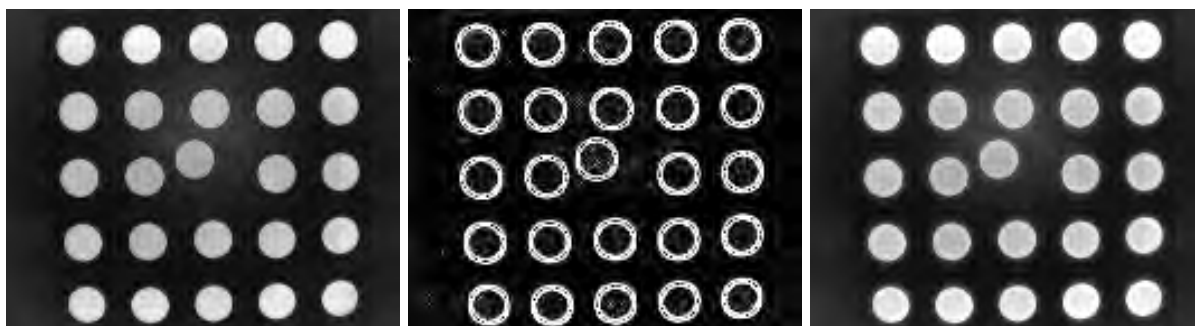
Figure 3.7: *Processing of amplitude images of the photogrammetric calibration test field from the SR-3000 in order to increase the contrast of the targets for the ellipse detection: improved amplitude image (left), the Laplace image (middle), which is smoothed with a 7x7 Gaussian filter afterwards (not shown), and the combination of both images (right).*

As a result, the image can now be processed with a simple threshold filter. By means of a simple search routine, the optimal threshold was found for each of the calibration images. The result of the threshold filter is a b/w image. Within this binary image, ellipses are searched by means of the ellipse-fitting routine provided by OpenCV. Due to the different camera positions, the circular targets become ellipses. As it can be seen in figure 3.8 (left), the ellipses are precisely located. In the middle the centers (integer values!, no interpolation) are displayed within the image. The ellipses are shown as well (right). Finally, the corresponding target identification was carried out.

Beyond the analysis shown here, different experiments were undertaken to increase the accuracy of the determination of the targets. The method shown above is supposed to be accurate far better than one pixel. However, at the edges of the field of view, systematics may occur. In order to reduce these effects, a least squares matching (lsm) of a template was performed. The ellipse data were used as initial values for a matching. First, an adequate template with known image coordinates was used. This well-known template was matched to the amplitude image. Unfortunately, these investigations gave no usable results. Thus, the first solution, the ellipse fittings, were used for further study. The usage of the centers of the
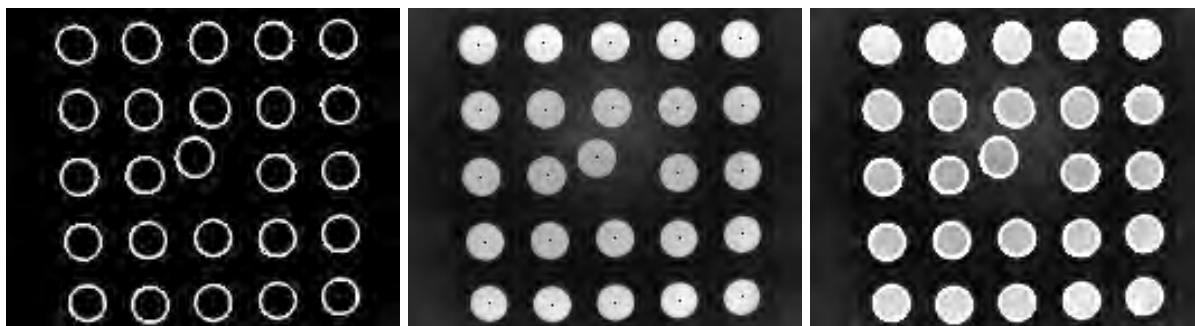
Figure 3.8: *Ellipse-fitting in the amplitude image in order to calibrate the SR-3000. On the left, the found ellipses are displayed after thresholding of the input image. In the middle, the centers of the extracted ellipses are shown. On the right, fitted ellipses are introduced into the image (white).*

ellipses as the target center's representation leads to small shifts, which have to be regarded and reduced in future calibrations.

The following calibration was done by means of a bundle adjustment with the *Australis* software provided by *Photometrix*. Figure 3.9 shows the camera positions for the calibration of the SR-3000. The stations were chosen carefully with respect to the sophisticated investigations (Remondino & Fraser 2006). Especially rotated camera stations were introduced. The real, relative 3-D coordinates of the target points were measured by means of a theodolite measurement system with a precision of about 20 μm. The accuracy is assumed to be below 0.1 mm. These coordinates are introduced into the calibration process as control points.
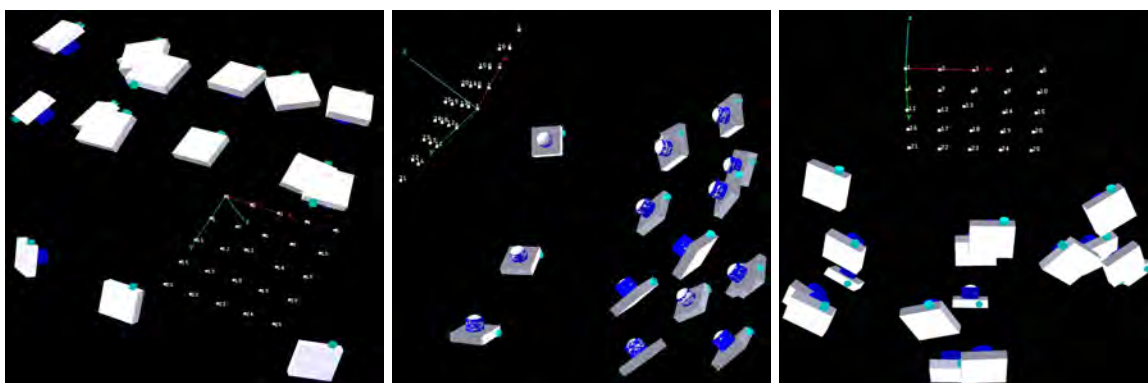
Figure 3.9: *Camera stations for the photogrammetric camera calibration of the SR-3000. Besides a well-chosen spatial distribution of the stations in order to get good intersection angles, rotated setups of the camera are essential for the calibration procedure.*

The results of the calibration are indicated in table 3.2 in closer detail. The demanded accuracy of about 0.01 mm for the camera constant was reached (compare section 2.4). The (full) data set can be found in appendix C.

Finally, it has to be concluded that the photogrammetric camera calibration is one of the most challenging aspects in the calibration procedure of the SR-3000. This is caused by the absence of intensity image information. Therefore, the amplitude data besides the distance measurements are the only information that can be used for the calibration. Even though the calibration of the SR-3000 has successfully been done in the investigations, much work has been left to automate this calibration procedure for everyday use of these sensors. However, with respect to the huge workpackage that is connected with the calibration of a RIM camera, the photogrammetric camera calibration has not been optimized to its maximum. Also, statistical tests of the calibration parameters have not been performed.

Parameter	Value	Standard Deviation
Camera Constant c	$7.9955\ mm$	$1.387e - 002\ mm$
Principle Point x_P, y_P	$0.0997\ mm$, $0.4357\ mm$	$1.969e - 002\ mm$, $2.027e - 002\ mm$
Radial Distortion K_1	$1.65764e - 003$	$3.884e - 004$
Radial Distortion K_2	$3.78532e - 005$	$6.179e - 005$
Radial Distortion K_3	$-2.65190e - 006$	$2.825e - 006$
Decentral Distortion P_1	$3.17463e - 004$	$1.172e - 004$
Decentral Distortion P_2	$-1.43750e - 004$	$1.198e - 004$
Scale Factor SCX	$-5.59513e - 004$	$4.216e - 004$
Sheer Factor SHR	$7.38923e - 005$	$3.972e - 004$

Table 3.2: *Photogrammetric calibration parameters of the SR-3000.*

3.3   Distance Measurement

This section deals with the calibration of the distance measurement system. Whereas the photogrammetric camera calibration removes, or at least reduces, deflections in two dimensions, systematic errors in the third dimension mainly depend on the distance measurement. Therefore, the distance has to be calibrated to obtain accurate data, too. In case of actual range imaging systems, these errors dominate the system's performance with respect to the derived three-dimensional coordinates. These errors can be eliminated or at least minimized with respect to their systematic influences by means of a calibration. The indicated and shown calibrations underlie one significant limitation: the scattering of radiation and temperature effects. The scattering effect finally dominates all effects. It primarily is of a systematic nature. Due to complexity, a compensation was not possible in this work. The influence of temperature effects is investigated in this thesis as well (cf. section 3.3.7 and chapter 4). The results shown in the next sections are mostly affected by scattering and temperature. Especially the investigation of the angle of incidence and amplitude are supposed to be significantly changed by a compensation and filtering of the scattering. This also has an effect on the distance-to-distance (linearity) calibration. Enhancements, both in optical as well as in calculative matters, are on their way. But as long as these solutions are not available on the market, the results shown here indicate the system's performance quite sufficiently.

3.3.1   Scattering

Figure 3.10: *Distance measurement variations toward targets of various reflectivities with respect to different background reflectivities. The distances were measured by the SR-3000 at a fixed distance of 1.660 m towards six targets of different reflectivities. The upper graph shows the variation of the measured distance with a white wall, the lower one with a black wall. An offset can be seen very clearly.*

Range imaging cameras are measuring distances in each pixel simultaneously. Due to the measurement principle, every pixel is considered to capture intensity information of the corresponding surface area mapped on this specific pixel, only. This simple model does not take into account correlation between the pixels. In terms of single ray optics, the reflected light goes through the lens and through the NIR-pass-filter directly to the sensor. Unfortunately, the light is reflected internally several times between the

diverse elements (lenses, filter, sensor chip). Thus, a pixel also contains information which belongs to neighboring pixels. This leads to false amplitude information and thus follows false distance data.

Figure 3.10 shows the results of measurements towards targets of a size of 2 *cm* × 2 *cm* with different reflectivities in a fixed distance of about 1.660 *m* to the SR-3000. A pixel near the center of the chip was chosen. The measurements were done twice. The only difference between the setups is the difference in the reflectivity of the surrounding wall. Thus, the measured distance should be the same in the range of setup uncertainties of about 2 *mm*. As figure 3.10 clearly indicates, the distance varies with the target's reflectivity as well as the background's reflectivity in the range of several centimeters. This effect is caused by the internal reflections within the sensor. Because this effect causes variations of a few centimeters, it clearly is one of the limiting factors for the distance accuracy of the SR-3000. Nevertheless, this effect shows systematics which should be calibrated in future investigations by means of reverse filtering, the knowledge of the exact dependencies, and of course the reduction due to constructural changes. A similar investigation was carried out with the PMD 3k-S. The camera was set up in front of a wall. The reflectivity was changed during the experiment from black to white. Five targets with reflectivities from white to black were mounted on the wall. So far, this experiment does not significantly differ to the one shown above. In order to reduce the influence of the scattering within the camera body, the old, standard optics were replaced by reflex-reduced optics. This objective has a different focal length. Nevertheless, as figure 3.11 indicates, these optics do not solve the scattering problem. The PMD 3k-S also suffers from scattering effects.
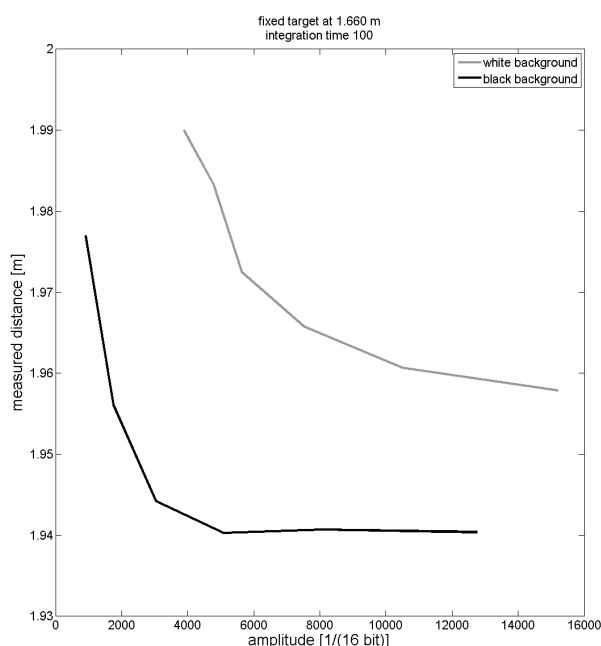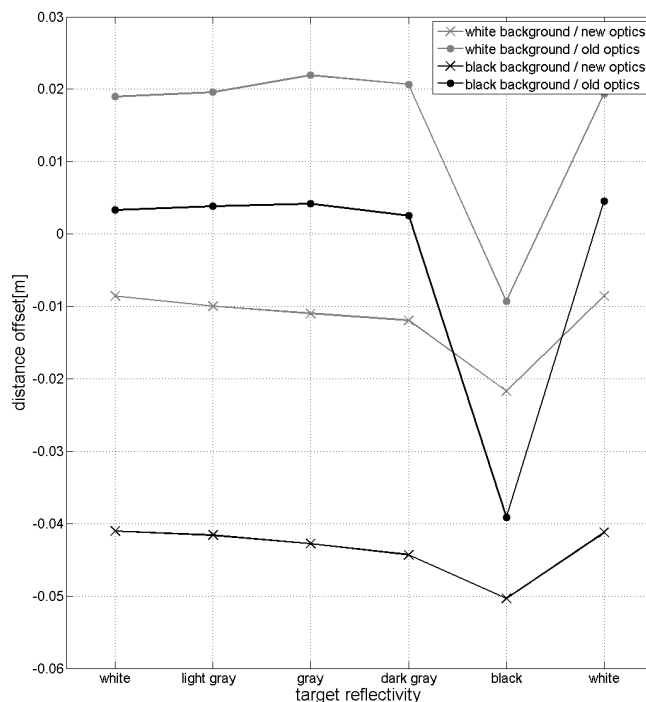

Figure 3.11: *Distance offset variations toward targets of various reflectivities with respect to different background reflectivities and two different optics. The distances were measured by the PMD 3k-S at a fixed distance of about 1.414 m toward six targets of different reflectivities. The influence of the surrounding wall can be clearly outlined. However, even though the new optics are reflex-reduced, they do not solve the scattering problem.*

Figure 3.12 shows the lateral and longitudinal influence of overexposed areas on the distance measurement in case of the SR-3000. In the center, an area can be seen, where a retro-reflective target was
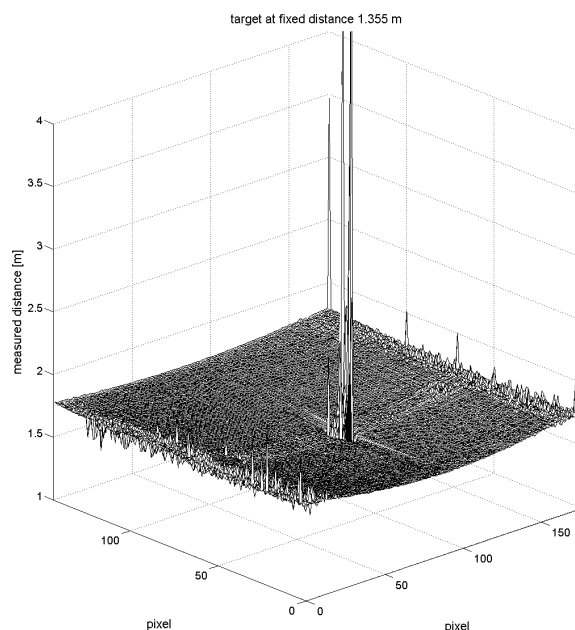
Figure 3.12: *Distance measurement against a wall with a retro-reflective tape carried out by the SR-3000. The small retro-reflective tape causes saturated pixels. Thus, the distance measurement gives no valid results (peaks). The most interesting effect can be observed in the neighboring pixels. The saturation of a few pixels causes neighboring pixels in the same row or column to measure shorter distances.*
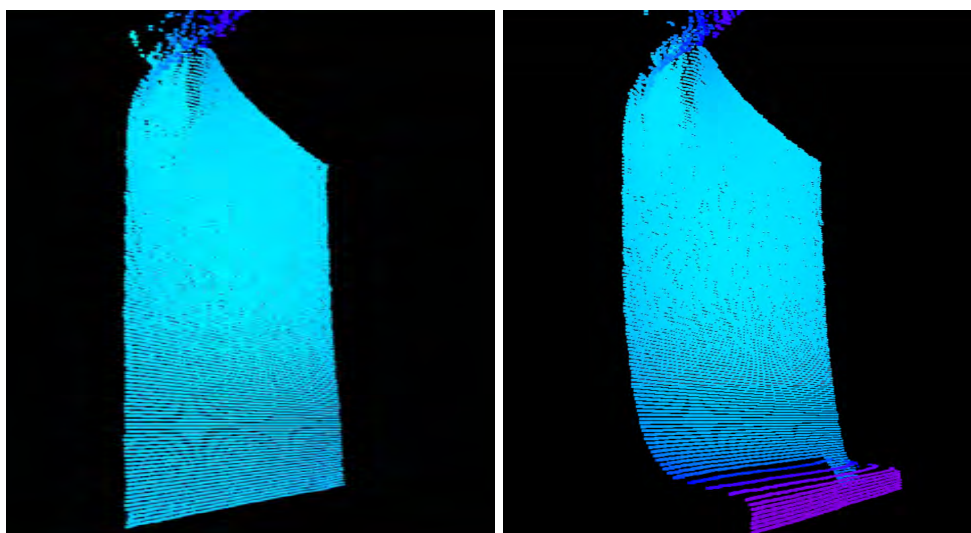
Figure 3.13: *Scattering effect in the SR-3000. Even pixels far away from the introduced object are affected.*

measured. This quite small area has an effect on the neighboring pixels up to the edges of the sensor.

Typically, scattering becomes obvious when introducing a very close target into a static measurement scene. Figure 3.13 shows such a setup. On the left, a white wall has been measured. The anomaly on top is caused by a reference light path. On the right, the introduced flat object can be seen. Beyond the mixed pixels (cf. section 3.3.10), a distance variation of pixels is present, even though they are situated far away from the object.

Further on, the distance variation of a single pixel was verified experimentally. Again a white wall was
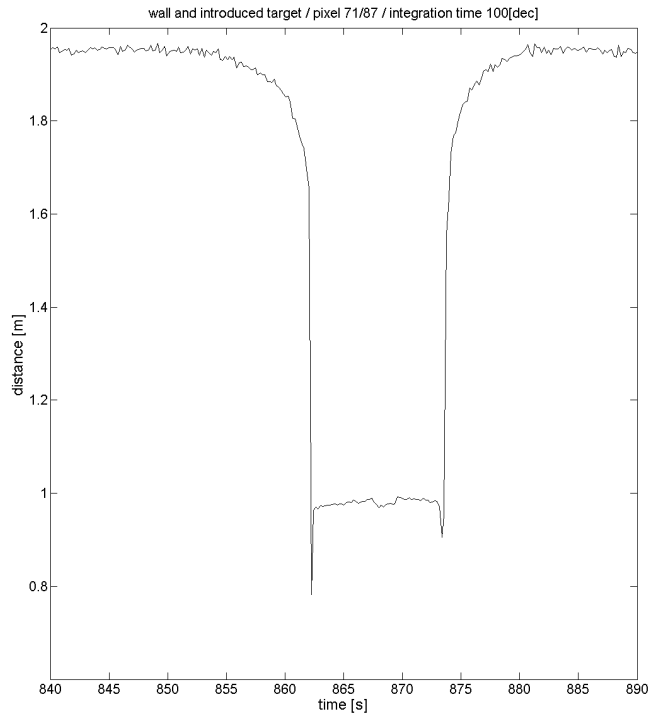
Figure 3.14: *Distance scattering of a central pixel of the SR-3000. A white paper target has slowly been moved through the field of view. Even though the analyzed pixel has no direct correspondence to the target, the distance measurement is already affected and becomes significantly shorter.*

measured. After a warm up sequence, a white paper target was slowly moved through the field of view. In figure 3.14, it can be seen that the distance changes as expected. But even though the target has not been in the field of view of the specific pixel, the distance already becomes affected. This is caused by the scattering within the sensor. This effect is similar to the mixed pixel phenomena, again. But scattering disturbs the whole measurement process due to its influence on nearly the whole sensor array at once.

The importance of the scattering has been underestimated so far. It is one of the limiting factors of the distance measurement accuracy. After most of the investigations, described in this thesis, had been made, the significance of scattering became clear. Future work needs to concentrate on the constructural as well as on the mathematical control of this effect. More complex and detailed investigations are needed to understand and interpret the behavior of the light within the sensor.

3.3.2 Integration Time

The controlling software of the investigated RIM cameras (SR-2 and SR-3000) allows for user-defined integration times. In this case the integration time is not the integration interval Δt shown in section 2.1.2.2, but the number of integration cycles over which the photon-generated charges are integrated within the pixel storage sites. It ranges from 1 to 255. The acquisition time depends on the type of camera and the implemented measurement algorithm. The integration time has several influences on the measurements. An increased integration time primarily has the following effects:

- A higher integration time leads to a better SNR and, thus, to more precise data.

- With an increasing integration time, the amplitude of the measured distance signal increases. Thus, the saturation level is reached faster compared to the same target's reflectivity and a lower integra-

tion time. Normally, this limits the minimal measurable distance.

- The offset of the distance measurement varies. An increasing integration time leads to shorter measured distances.

- The acquisition speed decreases.

Even though an increasing integration time increases the SNR significantly, however, it also enlarges the overall acquisition time for a single range image as well as it is leading faster to electronic pixel saturation. Thus, a consensus between precision and acquisition speed has to be found for every application, separately. But the main problem, with respect to different integration times, are the occurring offset differences. In order to reduce the dimension of investigations in this work, three representative integration times were chosen:

- 16

- 60

- 100

in decimal notation ([dec]), as used in the software. Most of the investigations were only carried out with these three integration times. Further settings would have to be investigated separately. In some cases only a single integration time was analyzed, which was in most cases 100 [*dec*].

3.3.3   Statistics

An analysis of the statistics of the distance measurements was done, as well. In many cases the distribution of the desired measurands is assumed to follow the rules of the normal (Gaussian) distribution. For the chosen integration times, the histograms of approximately 8000 distance measurements are listed in appendix D. For the SR-3000 one histogram is exemplarily displayed in figure 3.15. The distribution of the measurements is close to a normal distribution. But according different reasons, a χ^2-test failed. First, the number of measurements is perhaps not high enough. However, due to the programming of the data acquisition, the total number of measurements that can be captured in a fast sequence, is limited to the memory of the used computer. File access was avoided during the measurements. Second, the distance measurements are evaluated by means of an *atan* function. Because of electronic reasons and acquisition speed, not all of the 16 *bit* are used. Some measurements are not available and, therefore, shifted into neighboring bins. This leads to empty bins. The histogram for the SR-2 (integration time 16) in figure D.1 shows this effect clearly. Lastly, the choice of the size and the borders of the bins has an impact on the histograms.

This effect also is indicated in distance measurement data from section 3.3.7. Although the distance to the target remains constant, the statistic distribution of the measurements can be seen. Figure 3.16 displays an extracted section of the measurement shown in figure 3.41. It becomes clear that not all sampling steps are available. Empty sections occur.

In order to validate the distribution the measurements follow, a Gaussian function was fitted to the histograms. The distribution was chosen to be a general Gaussian:

$$y = a \cdot e^{-\left(\frac{x-b}{c}\right)^2} \tag{3.5}$$

In table 3.3 the results of the fittings are listed. Special interest is laid on the comparison of the mean value of the measurements and the center of the fitted distribution. It clearly can be seen that the values are nearly identical. However, for the simplicity of the evaluation, normal distribution is assumed to be significant. This is verified by the redundancy factor R of the fitted Gaussian distribution. This assumption is especially valid for higher integration times.
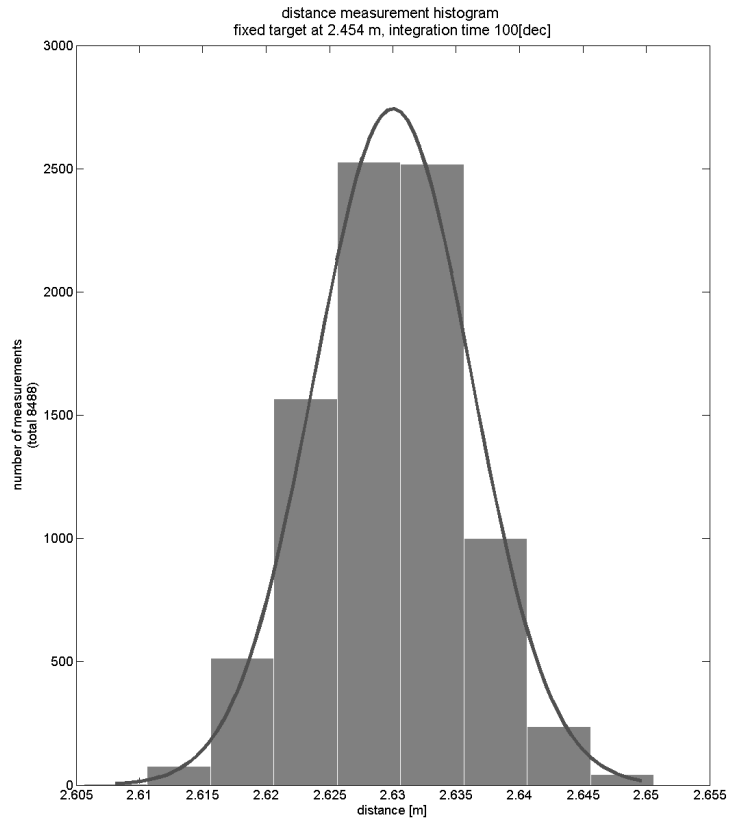
Figure 3.15: *Histogram of SR-3000 distance measurements with adjusted Gaussian distribution (for more details cf. appendix D).*
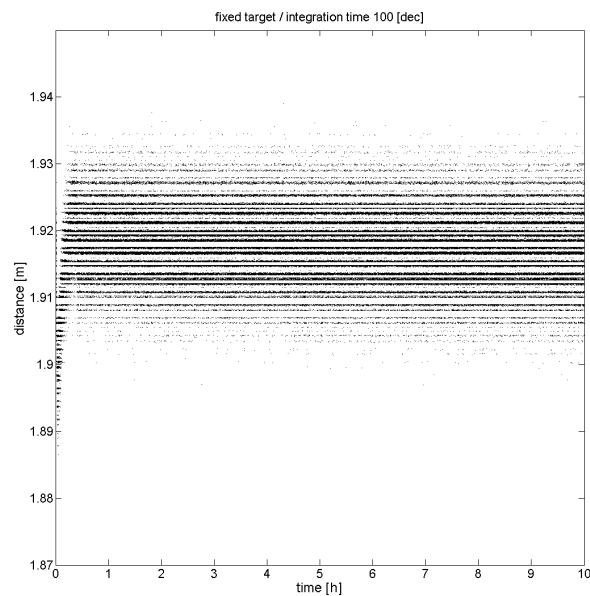

Figure 3.16: *Empty sampling intervals (SR-3000). Even though the resolution on the sensor is higher, not all possible distances are used within the calculation.*

SR-3000

	integr. time 16 [dec]	integr. time 60 [dec]	integr. time 100 [dec]
#	7957	7835	8488
a	612.8	1808	2743
b [m]	2.557	2.621	2.630
mean measurements [m]	2.557	2.621	2.630
c [m]	0.03728	0.01226	0.008728
R	0.79	0.9667	0.9916
RMSE	117.1	135.4	92.78

SR-2

	integr. time 16 [dec]	integr. time 60 [dec]	integr. time 100 [dec]
#	6548	7635	8202
a	857.3	2601	3473
b [m]	2.601	2.611	2.650
mean measurements [m]	2.600	2.613	2.649
c [m]	0.02188	0.007848	0.006515
R	0.4887	0.9438	0.9799
RMSE	338.7	252.0	215.0

Table 3.3: *Fitting parameters for distance measurement histograms of the SR-2 and the SR-3000 and the functional dependency of a Gaussian distribution (cf. equation 3.5). Special interest is laid on the parameter R, which is an indicator for the quality of the fitting. In cases of the higher integration times, R becomes nearly 1, which means a good fit.*

To get a closer idea of the sensor's precision as a conjunction of sensor elements, the standard deviation of the distance measurement system (each pixel) observed over the whole sensor is a meaningful measure. For its derivation, the following measurement setup was chosen:

The sensor to be analyzed was set up in front of a white wall in a perpendicular distance of about 2.463 m. The wall's significant properties (position and orientation) with respect to the sensor were derived by means of a scanning total station. A reasonably high number of points were acquired and the plane parameters of the wall were calculated by means of an adjustment. The normal vector of the wall, hitting the center point of the RIM camera, was marked on the wall by means of a retro-reflective tape, which can be easily found in both the intensity image (SR-2) and the amplitude image (SR-2 and SR-3000) by means of the threshold and clustering filters. This information was used for the orientation of the SR-2 and SR-3000 towards the wall in a perpendicular manner. For simplicity, the center of the sensor array and not the image focal point is used. As figure 3.17 indicates, the variation of the sensor between neighboring pixels is negligible. At least 100 distance measurements of each of the whole number of available pixels (without the defect ones) were done and the standard deviation for a single distance measurement for each single pixel was calculated. Figure 3.17 shows the results with respect to the sensors geometries (pixel wise). It clearly can be seen that the precision of the distance measurement varies over the sensor array. Pixels near the center show a precision of about 5 to 10 mm for a single measurement. With an increasing lateral offset from the center, the standard deviation continuously increases to a level of about 40 to 50 mm. The measurements of the SR-3000 are slightly better than those of the SR-2.

Figure 3.18 shows results of a set up in a shorter perpendicular distance of 1.366 m. It can be seen that the precision increases as expected. The reason for the differences in precision between the diverse pixels cannot be found within the sensor design. All the pixels in the CMOS array are designed identically and are more or less independent from other pixels, with respect to the precision of the measurements in
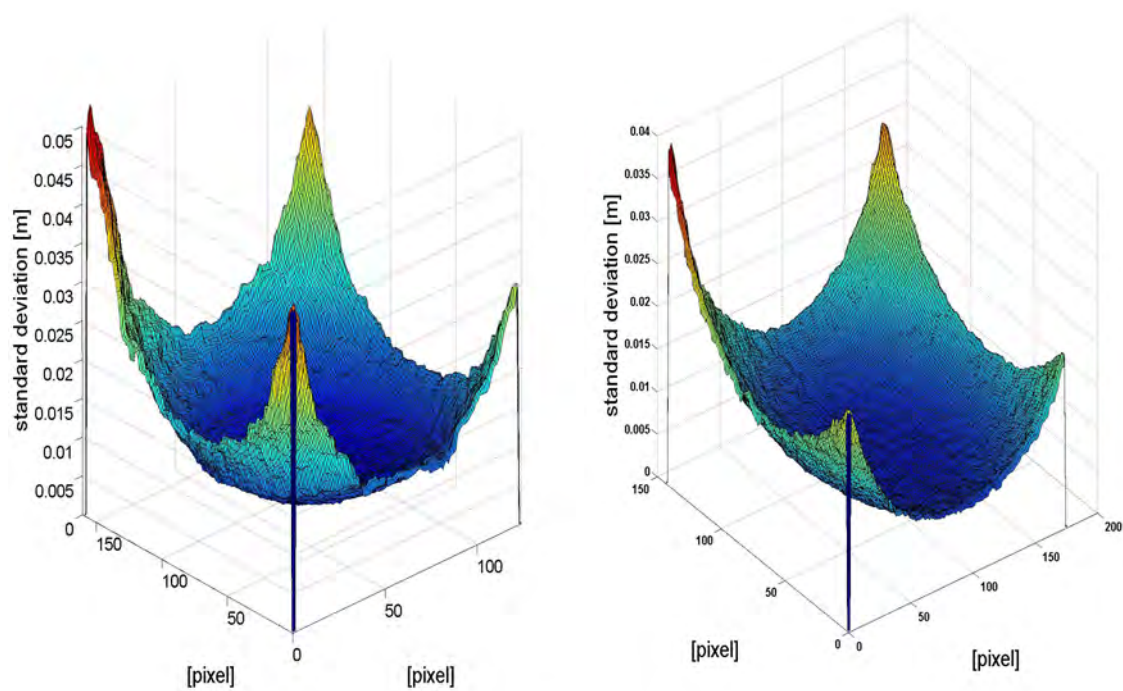
Figure 3.17: *Precision of a single distance measurement toward a plane wall (SR-2 left, SR-3000 right). The perpendicular distance was* 2.463 *m. Integration time 100 [dec].*
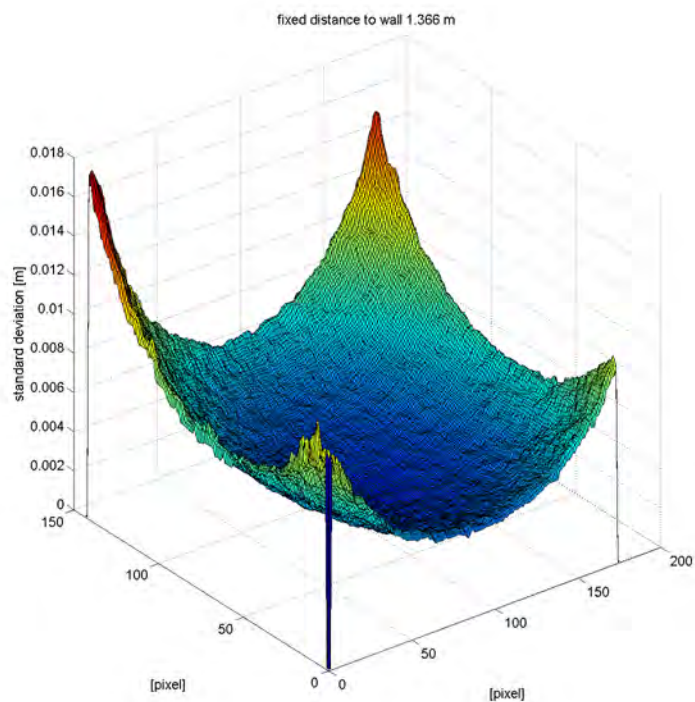
Figure 3.18: *Precision of a single distance measurement toward a plane wall (SR-3000). The perpendicular distance was* 1.366 *m, the integration time was 100[dec].*
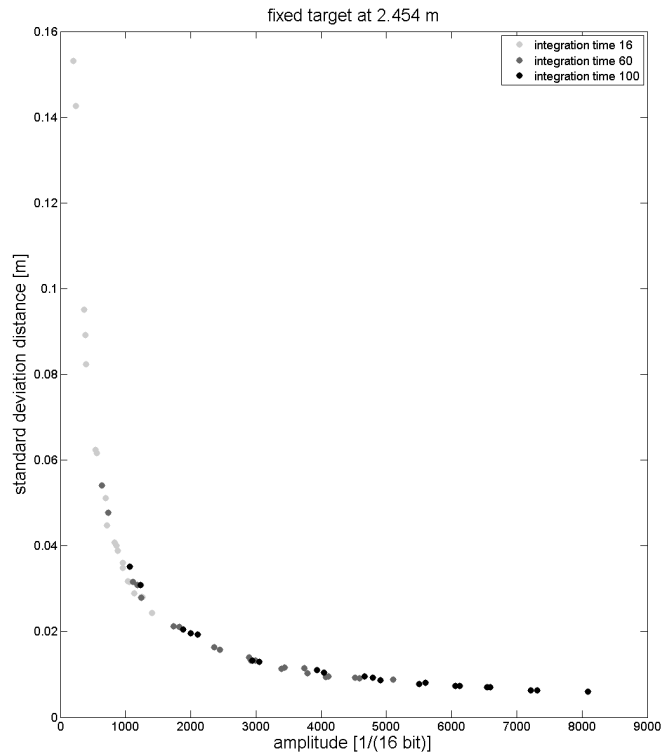
Figure 3.19: *Dependency between the amplitude and the distance measurement precision for the SR-3000. Remarkably, the choice of the integration time has no influence.*

contrast to systematic influences as indicated in sections 3.3.8 and 3.3.9. Therefore, this effect has to be a result of the electronics, optics, and the sensor setup. Some of these reasons are:

- Section 2.1.2.2 indicates that the precision of the distance measurement system highly depends on the amount of energy that comes back to the sensor. The higher the amplitude, the better the derived distance. In section 3.3.4 it is shown that the LED emitting system does not radiate homogeneously over the whole field of view, but shows systematic effects. This radiation distribution correlates with the precision of the distance measurement with respect to the specific pixel position on the sensor: the emitting system radiates less power at the edges of the camera's field of view than at the center. Less energy means a decreasing precision of the distance measurements. Therefore, the distance measurement at the edges of the field of view has to be worse than in the middle of the sensor.

- The SR-2 and the SR-3000 are equipped with small diameter lenses. The energy flow through such lenses is supposed to decrease at the edges of the field of view. Therefore, the same conclusion can be drawn as in the previous aspect: the distance precision has to be lower at the edges.

- The third aspect concerns the setup in front of a flat wall. Two influences can be named: the increasing angle of incidence and the increasing distance towards the edges of the field of view reduce the energy flow back to the sensor. This again indicates a decreasing precision of the distance measurement. Further, the increasing angle of incidence in correspondence with the non-Lambertian reflectance model also leads to lower reflected optical energy (cf. section 2.1.2.2).

The first two aspects are camera-specific and are not influenced by the setup of the system. The third one only relates to the experiment setup.

The influence of the amplitude of the demodulated signal has a direct impact on the distance measurement precision: distance precision and amplitude are directly anti-proportional to each other. An experiment was carried out to verify the theory. It is explained in more detail in section 3.3.5. Figure 3.19 shows the statistical results of this experiment. In correspondence with the theoretical background discussed in section 2.1.2.2 (figure 2.7), the amplitude influences the distance precision anti-proportionally (equation 2.8). The choice of the integration time has no influence on the precision-to-amplitude dependency.

3.3.4   Emitting System (LEDs)

The calculation of coordinates derived from the initial output of the sensor (distance and pixel coordinates) is based on the assumption that the emitting unit and sensor are placed at the same spatial position. Obviously, this has not been realized within all analyzed sensors, the SR-2, the SR-3000, and the PMD 3k-S. Due to electronic reasons, the LEDs were mounted around the optical system. If all LEDs radiate in-phase, the only influencing parameter is the distance difference between the single LEDs. Due to the type of modulation (amplitude), the result is a signal with a lowered amplitude. In case of a symmetrical arrangement of the LEDs around the camera's normal through the focal point, the sum of signals has no phase shift with respect to the center. In case of the SR-2, this requirement is given. The SR-3000 has a small unbalance. However, this effect increases the SNR and results in a minimally increased precision towards the edges of the field of view. The geometrical influences on the distance offsets were already analyzed by Gut (2004) and Hempel (2007).
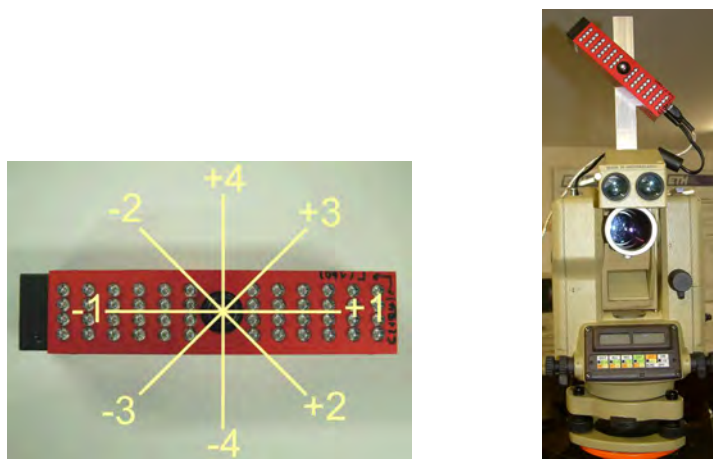
Figure 3.20: *Overview (left) and setup (right) of the LED unit investigation.*

Besides the geometrical influence of the placement of the LEDs on the distance measurement, the radiation properties are of special interest. Equation 2.9 indicates that there is a direct dependency between the amount of energy from the original emitted radiation (in amplitude), which is captured by the sensor, and the precision of the measured distance. Thus, the illumination of the scene is of further importance for the analysis of a RIM camera. In case of the SR-2, the radiation properties of the complete set of LEDs were measured. In order to perform precise angular measurements, the SR-2 was mounted on top of a theodolite and placed in front of a radiance measurement unit (Newport Handheld Optical Power Meter 840). In steps of 10° the emitted optical power was measured and reduced to a distance of $1\,m$ for reasons of comparability. Four different setups with different orientations of the SR-2 were made (cf. figure 3.20).

Figure 3.21 displays the central normalized data sets. The decreasing power towards the edges of the field of view is clearly visible. Only about 30 *to* 50 % of the center-near power remains at the outer limits. With respect to equation 2.9, it can be expected that the precision of the distance measurement
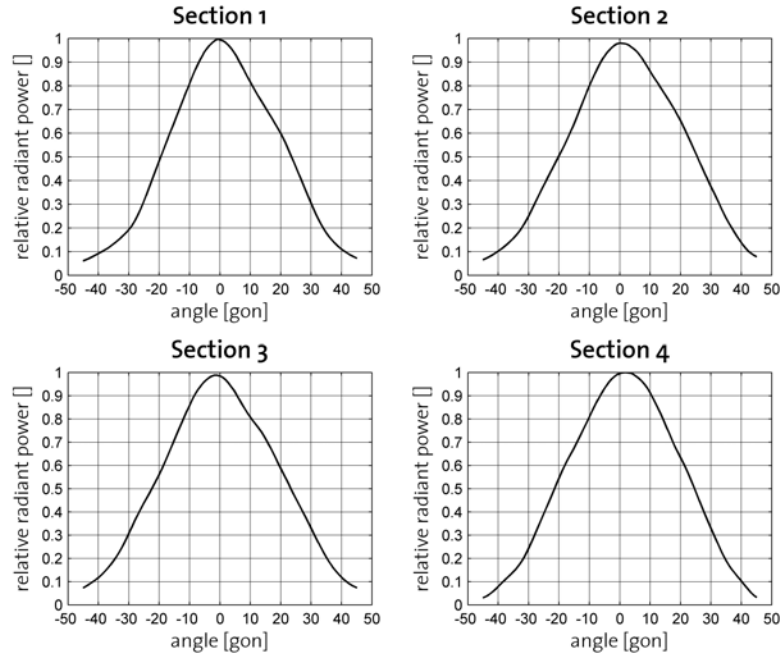
Figure 3.21: *Emitted radiation of the SR-2's LED unit. The sections are indicated in figure 3.20. The decreasing downwards to about 40 % of the radiated energy towards the edges of the field of view (approx. ±25 gon) in relation to the center are clearly visible.*

will decrease in the same way the radiated power decreases. If only a nth part of the energy is radiated, the standard deviation decreases with $\sqrt{n}$ (assumption: the amplitude and intensity decrease equally). Section 3.3.3 shows the effect of this problem more closely.

3.3.5   Target Reflectivity

Different influences which potentially have an impact on the distance measurement have to be included into a calibration process evaluation. Therefore, the influence of the reflected energy on the distance measurement was investigated. If an influence exists, the possibility of its calibration is of importance for an increased accuracy of the distance measurements.

In a first experiment, a distance calibration which compares the nominal distance to the distance measured by the SR-2 was done with several targets with different reflectivities. To qualify and quantify this influence, the distance calibration for a single pixel on a calibration track line (cf. section 3.3.8) was done with five planar targets with different reflectivities: black, dark gray, gray, light gray, and white. Figure 3.22 shows the results of the distance calibration for an integration time of 140. The object's reflectivity has an impact on the distance measurements. As figure 3.22 indicates, differences with respect to the various reflectivities of the targets are visible. However, clear systematics in the offset variations are not obvious, here. In order to derive this influence more clearly, further investigations which avoid the influences of distance and the angle of incidence were done.

A setup as indicated in figure 3.23 was chosen. For the sole variation of the reflectivity, a planar target with decreasing reflectivity (gray wedge) was moved perpendicular in front of the SR-3000, by means of the motorized trolley of the calibration track line of the IGP (cf. section 3.3.8). In order to reduce the drift of temperature variations (cf. section 3.3.7) and variations in the distance because of deviations in the perpendicular arrangement, a reference section was introduced in the measurement target. Systematic errors caused by the sensor warm up were avoided by means of a warmup time of 6 minutes. For each measurement step, 200 measurements were acquired. The amplitude of the demodulated signal is a
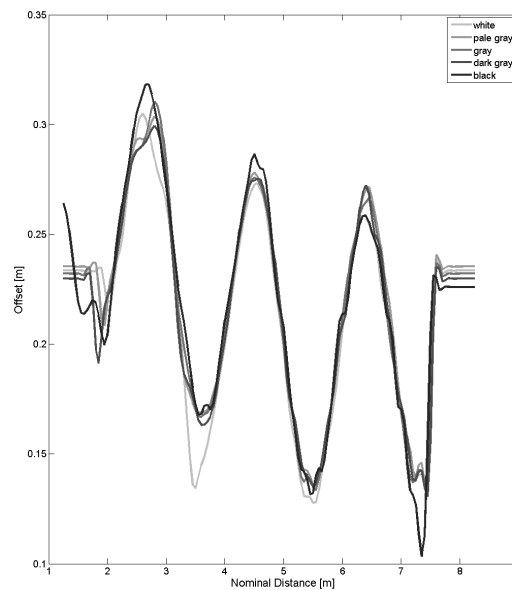
Figure 3.22: *Distance calibration results for the SR-2 for different target reflectivities (integration time 140 [dec]). The influence of the target's reflectivity has a slight impact on the distance offset. (The constant behavior at the outer limits are caused by setting the mean value of the offsets if no measurements were available.)*
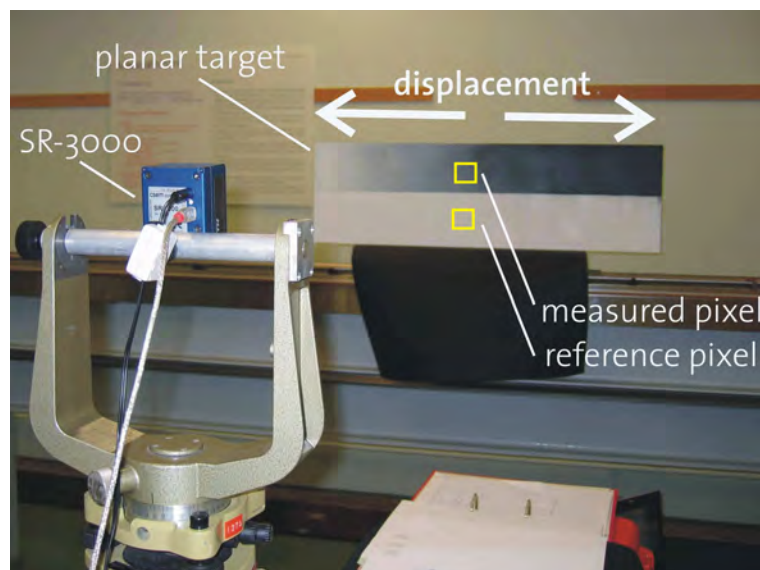
Figure 3.23: *Measurement setup for the determination of the influence of the target's reflectivity on the distance measurement. The SR-3000 was analyzed only.*

measure for the target's reflectivity if nothing else is changed, especially if the distance is not varied. Thus, the amplitude, with respect to the measured distance, is of importance in this experiment. Figure 3.24 clearly shows that a significant resulting correlation exists.

The characteristics of the functional relation is close to a hyperbola. Even though the distance to the target is fixed, lower amplitudes lead to higher measured distances. In case of very low amplitudes, the gradient is too high (in negative). Therefore, an exact calibration of the distance is not possible,
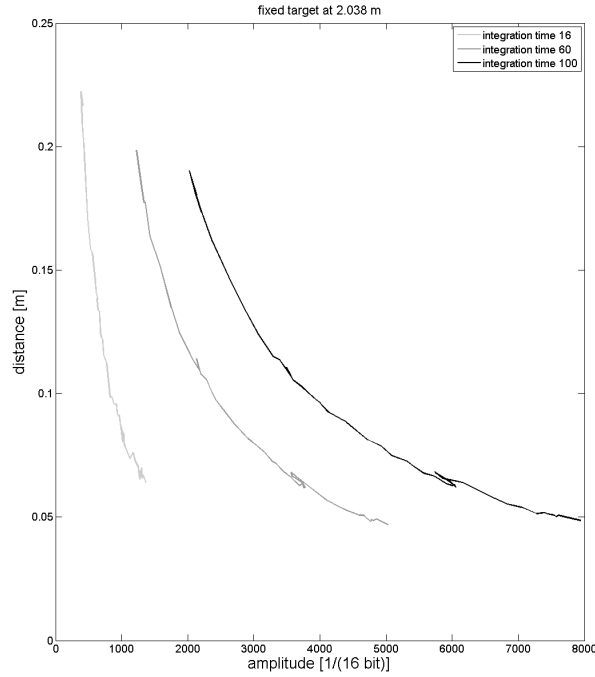
Figure 3.24: *Influence of the amplitude on the distance measurement of a single pixel (SR-3000). With a lower intensity, the measured distance increases. Here, the distance measurements for three different integration times, reduced with respect to their asymptotes, are shown.*

anymore. Thus, points measured with amplitudes below a certain limit shall be discarded. Due to the experiment's setup, amplitudes above 8000 $[1/(16\ bit)]$ were not acquired. In order to calibrate the distance measurements with respect to the amplitude, a general hyperbola (equation 3.6) was adjusted to the measurements:

$$\Delta d_A = \frac{a}{A_{meas} - b} + c \qquad (3.6)$$

Table 3.4 depicts the results. The fitting for the lowest integration time is not as good as for the higher integration times because of the small variation in amplitude. The derived parameters can be used to reduce distance measurements with respect to the demodulated amplitude.

Integr. Time [dec]	a	b	c
16	85.71	0.995	2.202
60	237.00	15.710	2.276
100	383.30	4.036	2.287

Table 3.4: *Derived parameters for the calibration of the distance with respect to the demodulated amplitude for the SR-3000.*

The parameter c is not of importance for the distance calibration. It only represents an offset. The offset is calibrated within the FPN calibration (cf. section 3.3.9) and the distance calibration in section 3.3.8. Thus, it leads to the following correction for the measured distance D_{meas}:

$$D_{corr} = D_{meas} - \Delta d_A = D_{meas} - \frac{a}{A_{meas} - b} \qquad (3.7)$$

where D_{meas} is the measured distance and A_{meas} the measured amplitude. A reduction of the measured distance to a reference distance with the maximal amplitude of 16 *bit* is possible.
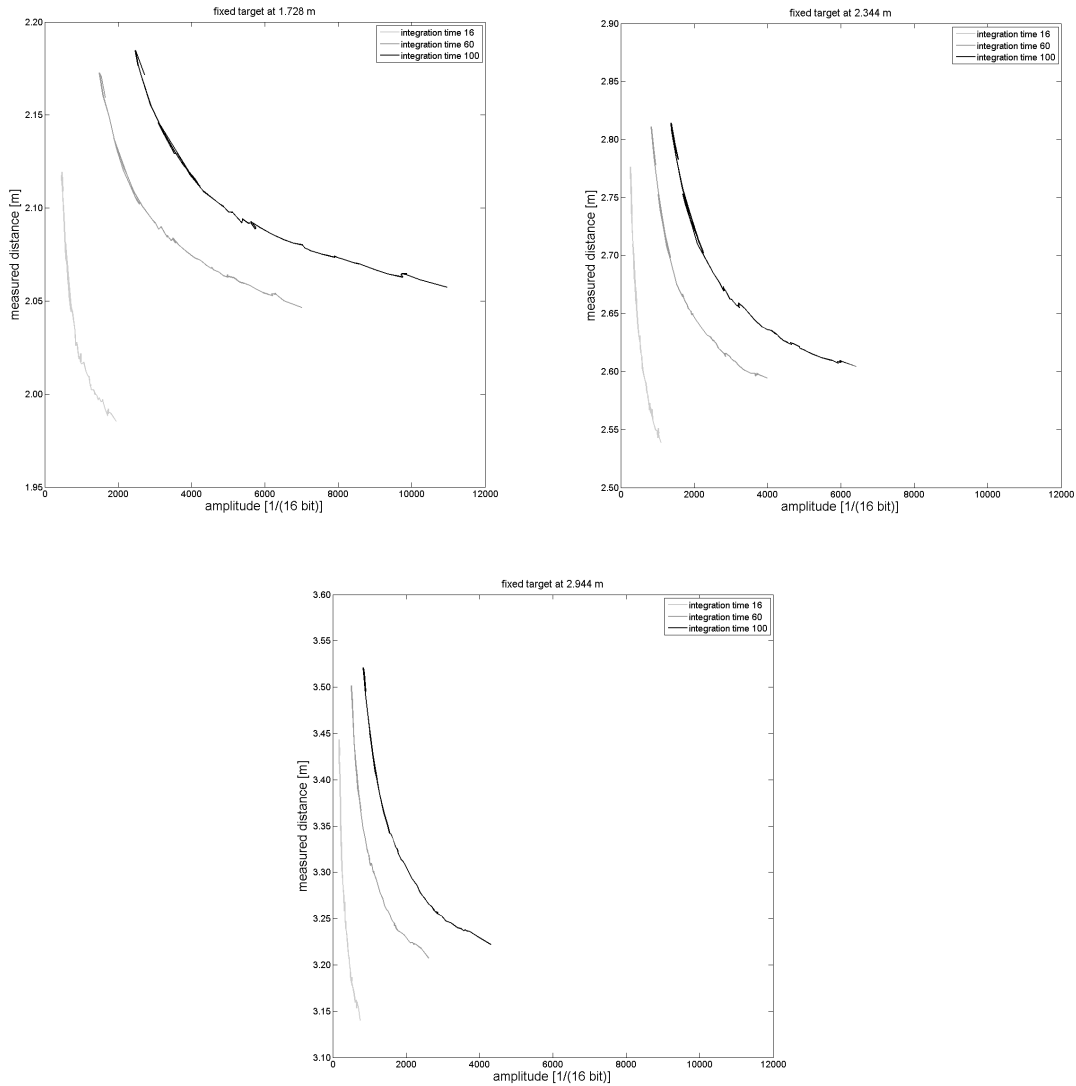
Figure 3.25: *Repetition of the gray wedge experiment with three different distances. The results seem to be very similar, but figure 3.26 shows that there are significant differences.*

For all integration times, lower limits have to be defined according to the accuracy requests of the application. These cut-off amplitude limits are necessary because of the high uncertainty of the distance measurement with respect to the uncertainty of the measured amplitude. One of the main problems is the scattering noise as indicated in section 3.3.1. The experiment shown above was repeated with three different setup distances from the gray wedge. Figure 3.25 shows the single data series for distances of 1.728 m, 2.344 m, and 2.944 m. At first, the impression evolves that the results fit to each other. However, after a shift in distance (y axis) in such a manner that the distances at an amplitude of 4000 $1/16bit$ are 0.000 m, the differences become obviously visible. Even though they are very small in amplitude-direction, especially at lower amplitudes, the differences in distance-direction and thus in the desired distance, easily reach more than centimeter level.

In this experiment, the deviations are rather slight and, therefore, not obvious in captured scenes. The neighborhood of the investigated pixel does not change much. Further investigations, already discussed in section 3.3.1, have shown a bigger impact if the background varies significantly. Six targets with different reflectivities were set in front of a plane wall. The experiment was done twice; first with a black wall and second with a white wall. The results are shown in figure 3.10.
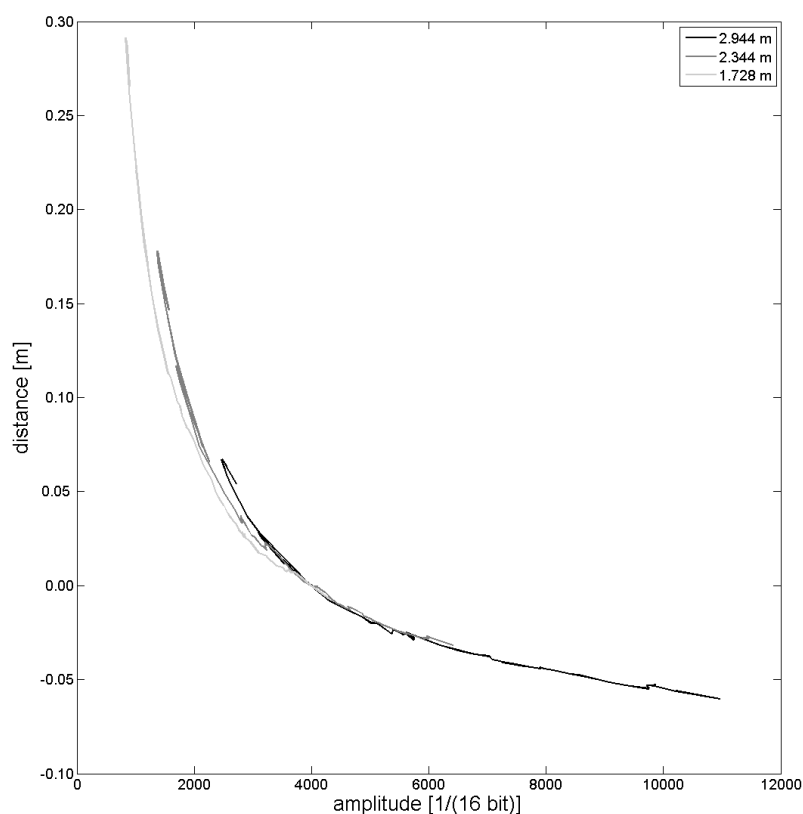
Figure 3.26: *Comparison of gray wedge experiments with different distances. The data series for the integration time of* 100 *[dec] from figure 3.25 were shifted in distance, so that the data are centered to an amplitude of* 4000 *[1/16bit]. The differences are significantly visible.*

3.3.6 Angle of Incidence

In order to quantify the influence of the angle of incidence on the distance measurement of a single pixel, a specialized experimental setup was developed. A planar target was mounted on a motorized total station in such a manner that it is rotatable about the vertical axis. Within the expected precision of the analyzed RIM camera SR-3000, the target is aligned to the vertical axis of the total station. A second total station is set up in front of the first one at a distance of about 2.5 m. The height of the second total station is chosen with the consideration that the RIM camera that replaces the second total station afterwards already is at the same height as the center of the target. Therefore, the different offsets in height of the different instruments have to be regarded. Figure 3.27 shows the setup.

Next, the total stations were collimated and the horizontal orientations were set to zero. A possible shift in parallel (horizontally) was avoided by first directing one of the total station toward the other's mounting screw. Afterwards, the second total station's telescope was levelled. One target plate was equipped with a retro-reflective tape in the center and was aligned by means of the second total station exactly above the first total station. This retro-reflecting tape can easily be found in the amplitude image of the RIM cameras because of its high reflectivity: saturation occurs.[3] After the measurement of the distance between the second total station and the target plate, the second total station was replaced by the RIM camera. The camera was oriented toward the retro-reflective tape with a center near pixel which

---

[3]A newer version of the driver causes highly reflective targets to have very low amplitudes. If such a driver is used, a minimum search in the amplitude image can be performed.

Figure 3.27: *Experimental setup for angle of incidence investigations. The theodolite, which rotates the target plate, is shown in the foreground in the left image. The second theodolite for the collimation and, therefore, the orientation as well as the determination of the nominal distance toward the target plate, can be seen in the background. In the right image the SR-3000 is visible.*
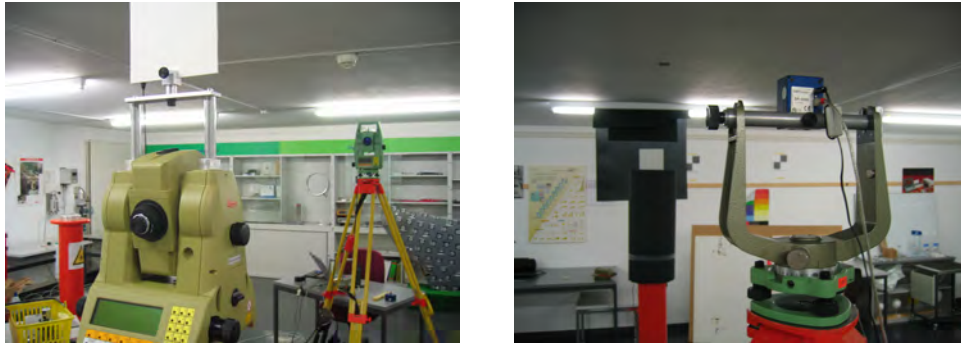
was investigated. As a result the RIM camera was then oriented toward the vertical axis of the first total station.
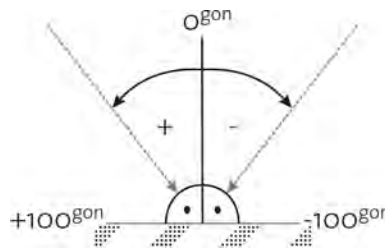
Figure 3.28: *Angle of incidence definition.*

The goal was to measure precisely towards target plates with different reflectivities with respect to the angle of incidence for a single, sensor center near pixel. The definition of the angle of incidence for this investigations is given in figure 3.28. In order to keep the influence of the variations of the distance measurements low, the median of 1000 measurements was used. The target plate was rotated by means of the total station automatically, controlled by the same computer which controls the camera acquisition. Therefore, influences and errors of the operator are minimized. The target was rotated from −90 *gon* to +90 *gon* in steps of 10 *gon*.

Figure 3.29 shows the median values of the measurements and the corresponding standard deviations, respectively. In correspondence with figure 3.30 and section 3.3.3, an increasing angle of incidence decreases the amount of backscattered optical energy and, thus, results in lower distance measurement precisions. The acquired data reflects this to a large degree. With an increasing angle of incidence, the standard deviation for a single distance measurement grows significantly.

Targets with different reflectivities were tried, but especially in the perpendicular case the reflectivities of the different targets had very little influence on the perpendicular case. This indicates that the reflected energy of the visibly darker targets is not as low as expected. The targets were equipped with foils with different hues of black color. Surprisingly, the foil did not reduce the reflectivity significantly enough. The surface of the target is reflective to a large degree. Only with an increasing angle of incidence, the reflectance differences between the targets become obvious in the precision data.

However, section 3.3.5 has already shown the functional dependency of the amplitude of the demodulated signal and the precision of the distance measurement. Out of the measurements carried out for the investigation of the influences of the angle of incidence, a database of different amplitudes towards the corresponding distance precisions results as a by-product. Figure 3.31 shows very clearly that a relation
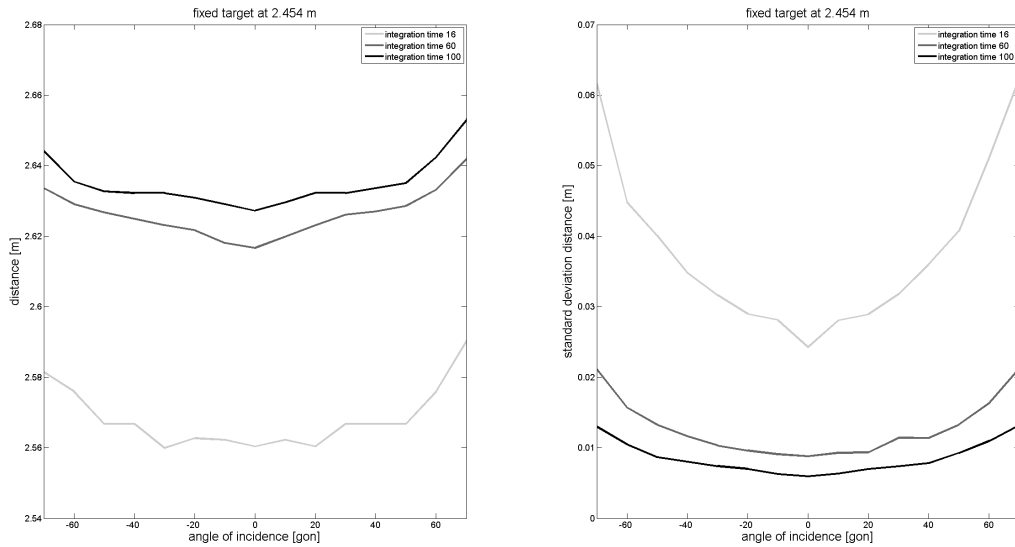
Figure 3.29: *Distance measurements (left) and precision (right) with respect to different angles of inci-dence for the SR-3000. The peak at the perpendicular measurements can be explained by a partial retro reflection.*
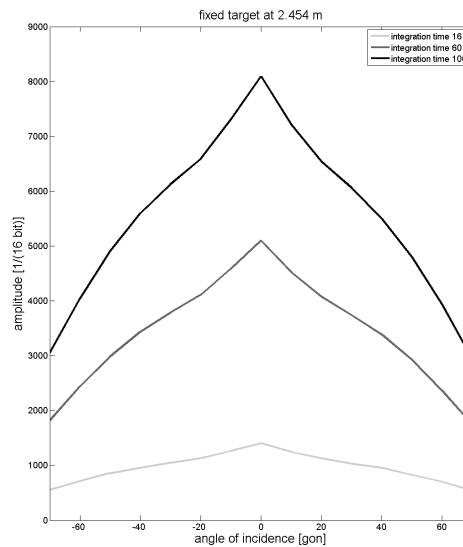
Figure 3.30: *Dependency between angle of incidence and the corresponding demodulated amplitude (SR-3000). The peaks at the perpendicular position can be explained by retro reflection of the target plate.*

between amplitude and distance precision exists. The results confirm the findings of section 3.3.5. The distance observations were normalized to the perpendicular case (perpendicular case $\hat{=} 0.000\ m$). Thus, the measurements of the three different integration times are made comparable. The only difference lies in the integration-time dependent distance measurement offsets.

In order to reduce systematic errors in the setup, the measurements of the corresponding angles of incidence ($\pm x°$) were averaged. Figure 3.32 (left) shows the results. The differences between the integration times are within the precision of the measurements. To separate the influence of the angle
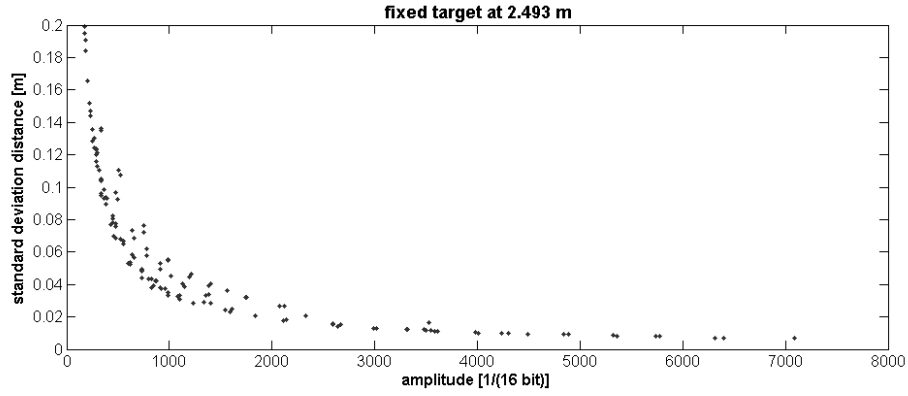
Figure 3.31: *Influence of the amplitude on the distance measurement precision (SR-3000). The three different investigated integration times exactly fit together and show the same results as shown in section 3.3.3. It can be seen that the angle of incidence's influence on the distance measurement precision seems to be reduced to the variation of the amplitude.*
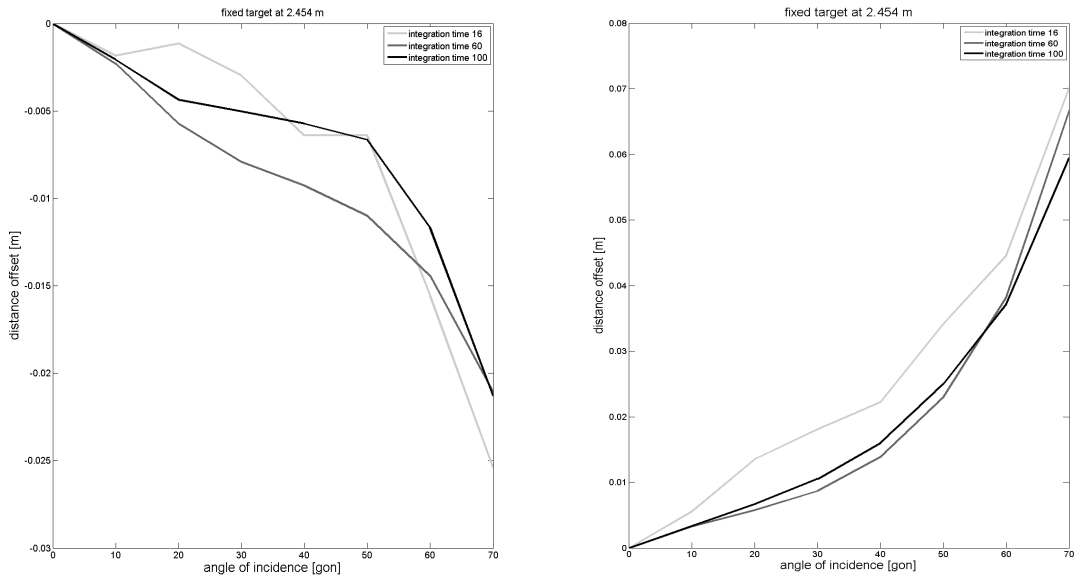
Figure 3.32: *Additive offsets for the calibration of distance measurements of the SR-3000 with respect to the angle of incidence (left) and corrected data due to amplitude variations (right). Without correction (left) the measured distance increases with an increasing angle of incidence. After the reduction of the influence of the amplitude (section 3.3.5), it becomes clear that the measured distance is highly influenced by the angle of incidence. Thus, the influences are contrary in their effect at inclined surfaces and neutralize each other to a large degree.*

of incidence from the measurements, the measurements had to be corrected with respect to the different demodulated amplitudes. Thus, the results from section 3.3.5 were applied. The measurements were corrected to the maximal amplitude corresponding distance. Figure 3.32 (right) shows the reduced data. In order to give a calculative representation of the influence, a polynomial of fourth order was fitted (without physical reason):

$$\Delta d_{aoi} = a_1 \cdot x^4 + a_2 \cdot x^3 + a_3 \cdot x^2 + a_4 \cdot x + a_5 \tag{3.8}$$

The fitting parameters are listed in table 3.5. Parameter a_5 is fixed to $0.000\ m$ in order to normalize

the correction to the perpendicular case. The values calculated out of the parametrization represent the additive offset. Thus, equation 3.9 can be extended in the following way to correct the measured distance D_{meas}:

$$D_{corr} = D_{meas} - \Delta d_A + \Delta d_{aoi} \tag{3.9}$$

Therefore, a reduction provision of the measured distance to a reference distance with the maximal amplitude of 16 *bit* and the perpendicular case is given.

Integr. Time [dec]	a_1	a_2	a_3	a_4	a_5	RMSE	R^2
16	$5.768e-9$	$-4.555e-7$	$9.834e-6$	$5.655e-4$	0.000	1.76e-3	0.9966
60	$4.122e-9$	$-1.806e-7$	$1.757e-6$	$2.996e-4$	0.000	0.43e-3	0.9998
100	$3.065e-9$	$-1.691e-7$	$4.899e-6$	$2.817e-4$	0.000	0.51e-3	0.9996

Table 3.5: *Derived parameters for the calibration of the distance with respect to the angle of incidence for the SR-3000. The angle of incidence has to be given in [gon].*

It can be pointed out that the influence of the angle of incidence is evident. It is remarkable that the dependency between amplitude and distance is inverse to the dependency between angle of incidence and distance. In detail, this leads to the following effect: with larger angles of incidence, the amount of the backscattered energy decreases. According to section 3.3.5, the measured distance becomes longer. In correspondence with figure 3.32 (right), the measured distance becomes shorter with an increased angle of incidence (additive calibration function is shown). Thus, for surfaces with unique reflectivity, both influences compensate each other to a large degree and the resulting offsets are about a tenth of the original influences. If variations in reflectivity and angle of incidence occur, the differences become obvious.

A calibration according to the angle of incidence seems to be thus unavoidable. Normally, the angle of incidence is unknown. Thus, it has to be derived out of the measurements. As figure 3.1 already indicated, the calibration of the RIM measurements causes a recursive calculation within the calibration process because of the influence of the angle of incidence. Therefore, at this point the calibration process becomes truly a matter of three dimensions. First, the distance measurements of all pixels are calibrated separately. A photogrammetric calibration is evident, too. Out of these information, the (local) 3-D coordinates of the object points are calculated. Next it is assumed, that the surface is primarily smooth. If this assumption is true, the angle of incidence can be calculated by means of an adjusted plane over the neighboring object points.

As already reported, scattering has an important influence on the distance measurements. Thus, the investigations should be repeated after the scattering effect has been cleared from the measurements.

3.3.7   Temperature

One influence of the environment, temperature to be explicit, will be examined here in closer detail. Due to the assumed high geometrical stability of the silicon wafer and the mounting case with respect to temperature changes, the external influences mainly affect the electronics. Possible meteorological influences are:

- temperature

- atmospheric pressure

- humidity

The effects of variations of the environmental parameters are well-described within geodetic literature with respect to electro-optical distance measurement. Therefore, the impact on the system's distance

measurement accuracy and precision can be derived on a theoretical level very well. An estimation of the influences on the measured distance with respect to the atmosphere can be done. First, the humidity can be excluded in the case of IR RIM cameras. The humidity only has a significant impact if microwaves are used. Under normal circumstances in the way of everyday usage, the variation of the remaining meteorological parameters can be set to the following limits:

- temperature: $-30 \ldots + 70\ °C$ $(1023\ hPa)$

- atmospheric pressure: $700 \ldots 1200\ hPa$ $(20°C)$

These variations result in the following variations for a maximum distance of 7.5 (50.0) m:

- temperature: $7.4996 \ldots 7.5003\ m$ $(49.9974 \ldots 50.0023\ m)$

- atmospheric pressure: $7.5007 \ldots 7.4997\ m$ $(50.0046 \ldots 49.9979\ m)$

The maximum deviation ranges from $7.4992 \ldots 7.5009\ m$ $(49.9945 \ldots 50.006\ m)$. These variations are calculated for special geodetic distance measurement systems $(\lambda = 850\mu m$, compare Baumann (1998) for example) and assumed to be valid for IR RIM measurements with respect to dimensional estimations, too. Thus, the dimension of the external influences on the electro-optical distance measurement can be neglected as irrelevant under normal circumstances. The deviations only reach about 0.01% of the measurement range. Investigations with respect to the atmospheric pressure have not been carried out.
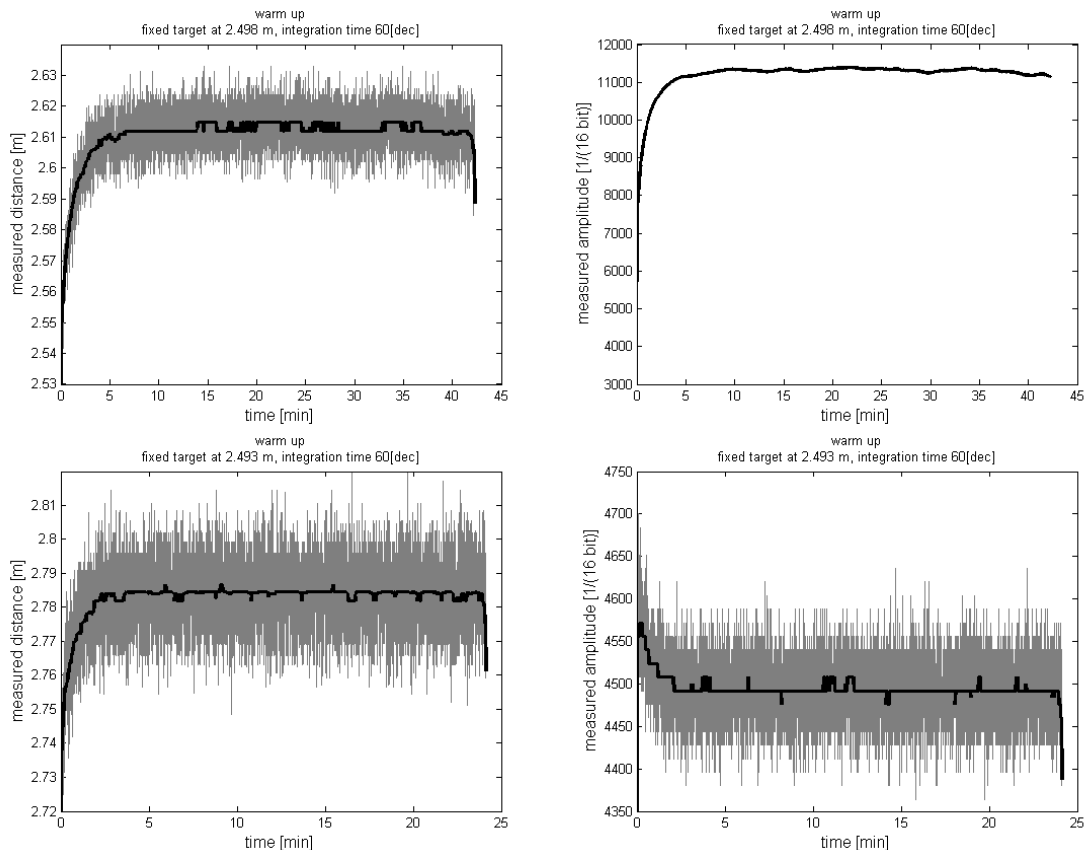
Figure 3.33: *Warm up of the SR-2 (top) and SR-3000 (bottom) RIM cameras and the influence on the demodulated distance and amplitude (black curves are filtered data). Further results for other integration times can be found in appendix E. Some short-term variations can be seen as well.*

Warm Up (Internal Temperature) However, beyond the influences on the radiated signal, the electronics themselves can be affected by the temperature of the environment. Two different aspects were

investigated: First a heat up of the system, especially the emitting system, consisting of a large number of LEDs, was considered to underlie a heat up process. In order to decide whether such an effect is present or not, the RIM cameras were set up in front of a white target at fixed distances. For three different integration times, the first 10′000 measurements were carried out. Figure 3.33 as well as figure E.1 and figure E.2 show the warm up process of the SR-2 and the SR-3000, respectively. Obviously, the measured distance varies, whereas the true distance is fixed. The same happens to the amplitude, whereas the reflectivity of the target does not change during the measurements, of course.

In all cases, the distance as well as the amplitude converge. Nevertheless, the dimensions of the warm up process highly differs between the SR-2 and the SR-3000. Besides different convergence times of the several integration times, the main difference of both sensors is that the SR-3000, due to several reasons, partially construction dependent, only needs half as long heat up time as the SR-2 does. The SR-2 stabilizes after about 12 minutes; the SR-3000 after about 6 minutes. These values are mainly chosen amply.
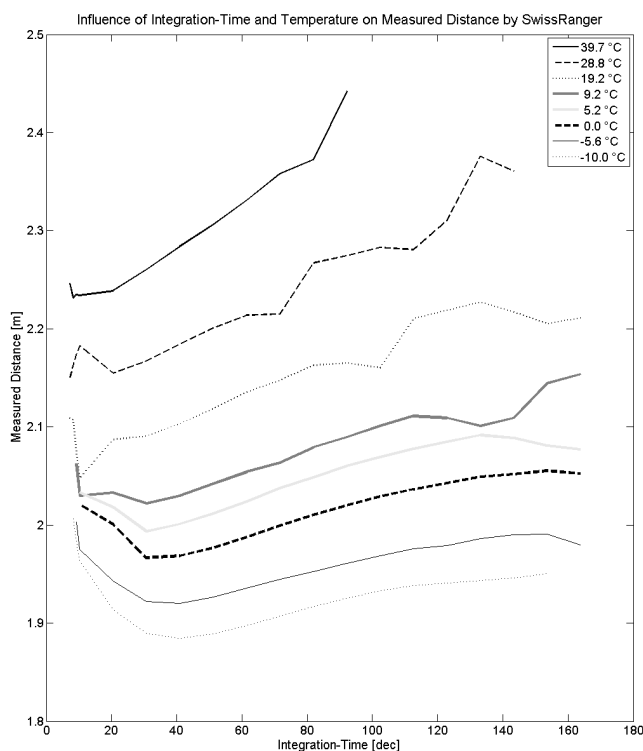
Figure 3.34: *Temperature dependent distance measurement variations of the SR-2. In this case the integration time dependent distance variations with respect to different external temperatures are shown. No warm up time was used. It can be clearly seen that different external temperatures cause distance offsets of some decimeters. The integration time dependent offsets are visible as well.*

External Temperature SR-2   The influence of the external temperature on the distance measurement system was investigated in the climate laboratory cell at IPG at ETH Zurich. This cell allows for measurements under well-defined atmospheric situations. First, the SR-2 was investigated in order to get a first idea of the temperature's influence on the distance measurements. In this case, only the temperature was of interest. The sensor was set up in front of a white wall in a nearly perpendicular manner and distances measured by a single pixel were captured. Different integration times were used. Figure 3.34 shows the results. In this case no warm up time was used. However, an influence of the

temperature is clearly visible. Higher temperatures lead to falsely longer measured distances. A gradient of about $8\frac{mm}{°C}$ was derived.
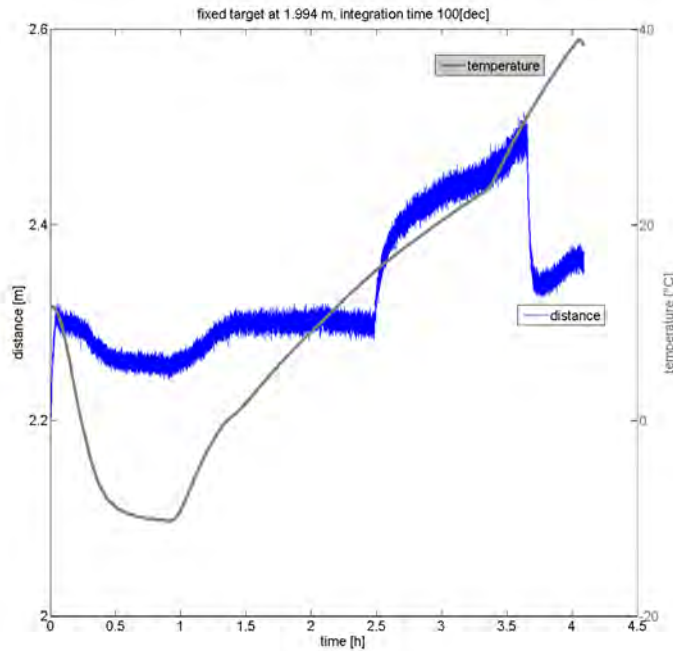
Figure 3.35: *Temperature dependent behavior of the distance measurements (SR-3000). The temperature has been cooled down to about $-10°C$ and then raised to about $40°C$. It becomes clear that the distance measurement correlates with the temperature, even though no definite strict systematic can be derived.*

External Temperature SR-3000 The preliminary investigations of the SR-2 gave the reason to analyze the SR-3000 in closer detail. The SR-3000 is equipped with an intelligent, temperature-driven, semi-active cooling. The included ventilator's speed is varied with respect to the temperature of the SR-3000. Again, the climate cell of the IGP was used for the investigations. Figure 3.41 shows the results of the first experiments with the SR-3000. In this case the distances are not calibrated with respect to amplitude and angle of incidence as suggested in sections 3.3.5 and 3.3.6. First, the temperature was decreased from $20°C$ down to $-10°C$. After the indicated warm up sequence, the distance measurement follows the temperature curve and decreased distances of a few centimeters are acquired. Afterwards, the temperature was increased nearly linearly up to $40°C$. First, the measured distance goes back to the $10°C$ level. In the following the distance stays constant up to a temperature of about $15°C$. Then the measured distance to the fixed target suddenly jumps back to the high correlation level up to about $30°C$. Here, the distance goes back to a lower level and varies more or less linear in correspondence with the temperature, again.

These observations indicate that the SR-3000 measures, analogue to the SR-2 (cf. figure 3.34), longer distances with an increasing temperature even though the target is not moved. The SR-3000 is equipped with an intelligent cooling system, as mentioned before. The most feasible explanation for the discontinuous developing can be found in the driving of the ventilation. In correspondence with the humidity and due to its semi-passive construction, the range of the cooling is limited. For a very limited temperature range, the cooling system can compensate for variations in the external temperature.

Further investigations were made in order to specify the dependencies in closer detail. The setup is similar to the investigations undertaken previously. As figure 3.36 indicates, the SR-3000 was set up in front of two white targets; the first one at a distance of $1.628\ m$ below the horizon of the image center;
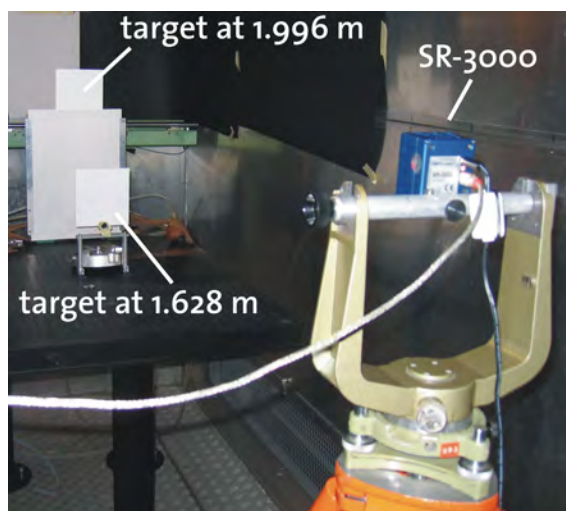
Figure 3.36: *Setup for temperature investigations of the SR-3000 in the climate laboratory cell of the IGP. Two different target plates at different distances were used.*

the second one near the perpendicular projection of the image center at a distance of $1.996\ m$. Thus, two different pixels were measured: 106/87 (lower) and 71/87 (near sensor center).
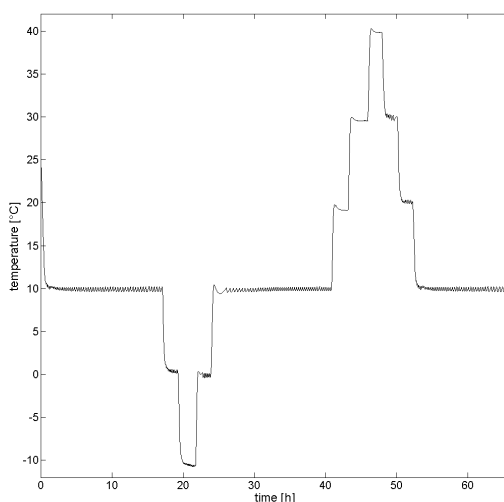
Figure 3.37: *Temperature curve for the investigations of the SR-3000.*

In order to avoid saturation effects and the influence of optical crosstalk, the background was partially filled with black cardboard. To derive significant data, the temperature cycle, which is shown in figure 3.37, was used. First, the temperature was stabilized at $10°C$ for over 15 hours. Then the temperature was driven in steps of $10°C$ to $0°C$, $-10°C$, $0°C$ and back to $10°C$ for 2 hours including the cool down and warm up phase. After a steady-state phase of again over 15 hours, the temperature was set to $20°C$, $30°C$, $40°C$, $30°C$, $20°C$ and back to $10°C$. All steps took about 2 hours to complete. Finally, $10°C$ were held for over 10 hours. This cycle was used to integrate steady-state as well as warm up and cool down phases equally. Due to the complexity, only the integration time of 100 [dec] was investigated. The acquisition speed was approximately 5 Hz. Thus, over 1.1 million measurement sets were acquired and analyzed.

Figure 3.38 shows the measurements of this experiment. On the left, the distance measurements of
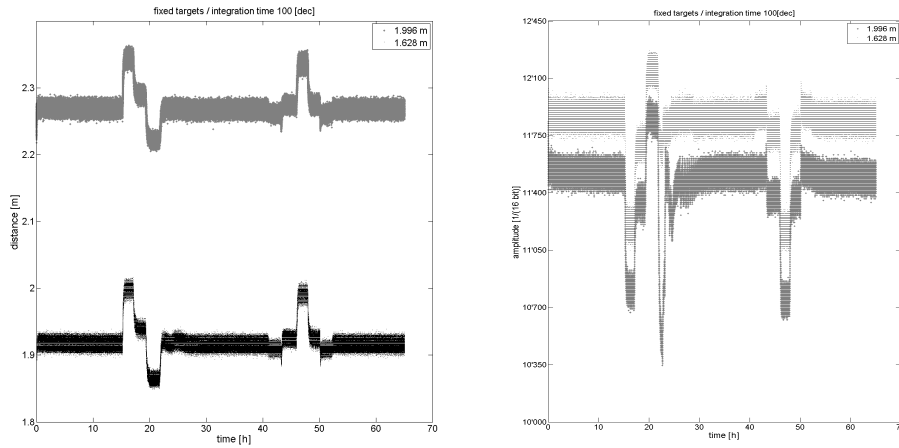
Figure 3.38: *Measured distances and amplitudes of two different pixels (106/87 and 71/87) under variation of the external temperature (SR-3000). The nominal distances are 1.628 m and 1.996 m. A high correlation of both can be seen.*
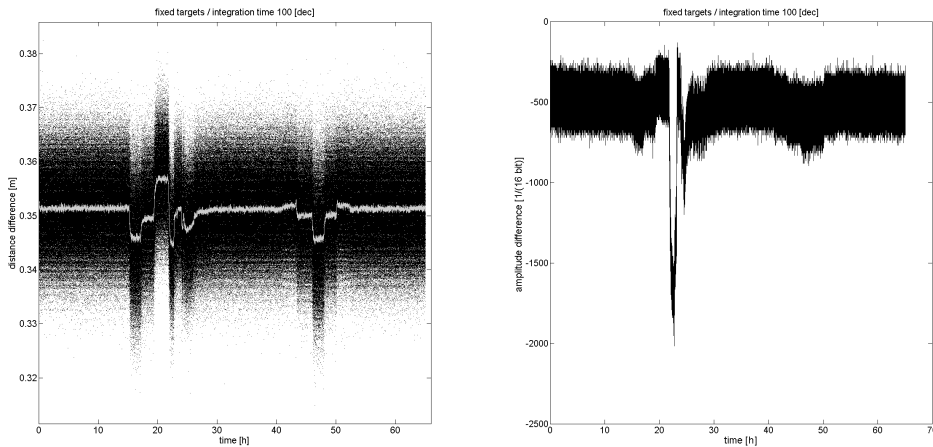
Figure 3.39: *Differences in distance (left) and amplitude measurements (right) for temperature experiment between both investigated pixels. For the distance measurements, a floating mean of 501 measurements is displayed in light gray as well. Besides some outliers (due to condensed water), the differences are constant and variations marginal (max 1.2 cm) but present. Therefore, a small variation of the scale may be present.*

both pixels are displayed over time. The scatter of the measurements leads to a band with a width of several centimeters. Nevertheless, as indicated later, the standard deviation of a single measurement is about 5 *mm*. First, the distance measurements as well as the demodulated amplitudes are supposed to be highly correlated with the external temperature. This will be analyzed in the following. But one anomaly in the amplitudes has to be examined. After about 22 hours, the amplitude of the center near pixel suddenly drops. During earlier experiments, it was observed that condensed water became present at the $0°C$ border. Thus, the reflectivity of the target plate changes. Due to unknown reasons, this effect is higher for the farther target. The different angles of incidence may have an influence, here.

The analysis of differences in distance and amplitude measurements shows that, besides the condensed water effect, the differences remain constant. Only a very small variation of a few millimeters for the distance measurements can be outlined. The variations in scale are marginal especially when close
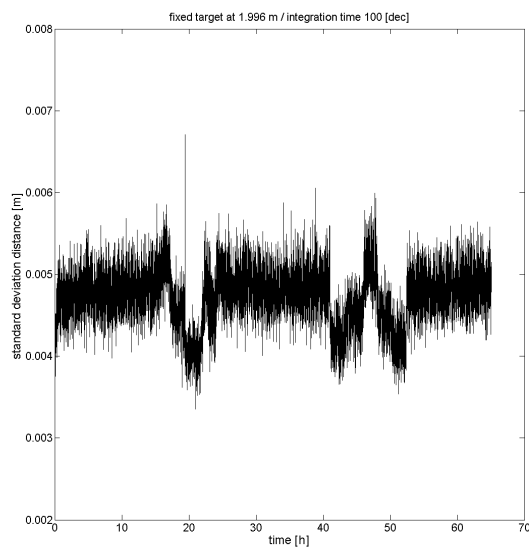
Figure 3.40: *Standard deviation of a single distance measurement at different external temperatures. Lower temperatures (external or by means of ventilated cooling) improve the distance measurement precision.*
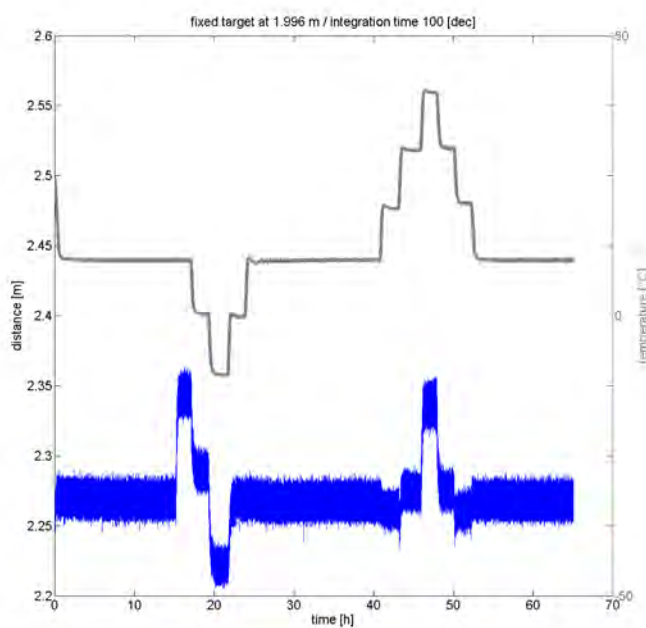
Figure 3.41: *External temperature and measured distance (SR-3000). A correlation seems to be existent.*

to room temperature. If a variation of the distance scale is present, it may be of interest in future investigations. Due to the enormous effort this investigation needed, no more measurements were done for the verification. In order to verify the distance measurement precision, the standard deviation of a single measurement was calculated for the whole data set for the farther target. Figure 3.40 makes clear that just a very weak correlation between distance precision and temperature is present. Nevertheless, the distance precision is better at lower temperatures. If an automated cooling of the temperatures over
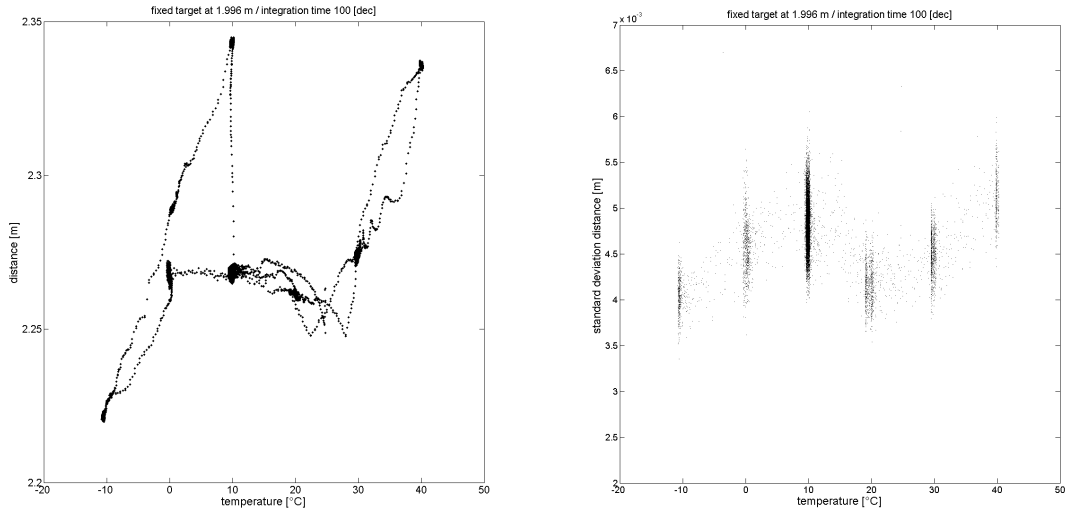
Figure 3.42: *Correlation between external temperature and the measured distance (left) and the distance measurement precision (right) for the SR-3000. Whereas no correlation between temperature and distance measurements is obvious, due to strong outliers from linearity, dependencies between the external temperature and the standard deviation of a single measured distance is valid with respect to the cooling system.*

$10°C$ is assumed, a reduced standard deviation can be explained here as well. Figure 3.41 displays the temperature (compare figure 3.37) and the measured distance towards the second target (1.996 m) within one diagram. On first view, distance and temperature are somewhat correlated. On a second, closer look, erratic fluctuations appear (the measurements were double-checked but not repeated due to complexity). Even though the steady-state sections lead to stabilized distances, the temperature changes do not lead to correlations. Figure 3.42 (left) makes this clear. A high correlation between the external temperature and the distance measurements cannot be seen. However, a correlation between the temperature and the distance measurement precision can be pointed out in figure 3.42 (right). If again the cooling ventilation is included in the analysis, lower temperatures lead to more precise data.

It can be concluded, though, that the SR-2's as well as the SR-3000's measurements are influenced by internal and external temperature conditions. However, for the SR-3000, these states are less predictable for the whole temperature range, but seem to be stable for room temperatures. Further investigations could be done. In order to reduce temperature influences, suppression methods, like the internal way of light as a reference, should be adopted. Chapter 4 deals with this topic more closely.

### 3.3.8 Distance / Linearity

One of the main errors of range imaging systems lies within the distance measurement system deviations with respect to the distance itself. Due to the well-known geometry of the imaging system, like pixel size, optics, and sensor placement, the photogrammetric camera calibration only has a limited but, nonetheless, significant impact on the accuracy of RIM cameras. Section 3.2 showed the influence of lens distortions and aberration in the case of the SR-2 and the SR-3000, respectively. Due to the miniaturization of the distance measurement system into small pixels and the limited speed of such semiconductor array measurement systems, a limited quality of the distance measurements results as already seen in the previous sections. Due to the high systematic deviations, a calibration of the distance measurement system seems to be possible. This section will explicitly deal with the distance calibration with respect to the distance itself, which is also known as the *linearity* of the system.

One of the main problems in the calibration process of range imaging cameras lies in the high number of ranging systems: each pixel is a complete demodulation section and, thus, more or less a distance measurement system of its own. In a best case scenario, every single pixel should be calibrated. This is obviously beyond every efficiency and economic aspect. Therefore, some generalization and systemization has to be done:

- If the offset for all pixels is different but stable, a fixed-pattern-noise (FPN) matrix can be determined. This is done in section 3.3.9.

- If the same systematic for all pixels was found, only one single pixel had to be calibrated. The derived functionality could be used to correct other pixels, as well. Such functionality shall be derived in this section. In this case, only very few pixel-specific parameters have to be derived and included within the calibration, like the fixed-pattern noise, presented in section 3.3.9, and a phase shift of the cyclic linearity deviations.

This section contains different measured aspects of the distance calibration. After the introduction of the experimental set up, the distance calibration for different integration times for a center-near pixel of the SR-2 will be presented. Then, the distance-to-distance calibration of the SR-3000 will be shown in more detail. The goal is to derive a calibration rule for the correction of distance data with respect to the previous section's findings as well as the linearity dependencies.

Distance Calibration Setup   The distance calibration for a single pixel was done on the automatic interferometric calibration track line at the IGP at ETH Zurich. The advantage of the trackline is the nearly completely automated measurement process. A complex programming was developed to integrate RIM cameras into the calibration process. The track line is equipped with an interferometer which has a precision of a few μm. This is then the precision of the distances given as the nominal distances in the following for the calibration process, too. The accuracy of the distance calibration (accuracy of the offset) is around 1...2 mm in this case. This is due to deviations and variations in the setup, the mounting, and the derivation of the offset. Figure 3.43 shows the calibration setup.

The RIM camera to be investigated is set up in line with the track line. A motorized trolley is equipped with a planar target. The target and the RIM camera are oriented toward each other in such a way that the target is measured in a perpendicular manner. The target shown in figure 3.43 was used for the calibration of the SR-2 and for early experiments with the SR-3000. Later, in order to be closer to the comparator principle of *Abbe*, for the calibration of the SR-3000 the target plate was moved nearer to the line of sight of the interferometer. Figure 3.44 shows the measurement principle of the calibration track line in closer detail. It is specially designed for the calibration of electro-optical distance measurement systems.

To derive reliable data, several different aspects have to be considered within the measurement of the distances as well as in the analysis. With respect to the measurement, the following steps were made:

- The target was marked with a retro-reflective target in order to orientate the RIM camera. For all distances, the retro-reflective target has to be mapped on the same pixel, which is of interest for the calibration. After the orientation and set up of the RIM camera, the retro-reflective target is removed.

- The sensor had a warmup time of 20 minutes for the SR-2 and 6 minutes for the SR-3000 to reduce the impact of self-induced temperature drifts as indicated in section 3.3.7

- In order to reduce linear drift-effects in the cameras as well as in the interferometer, the calibration was performed forth and back three times.

- The measurement range up to 7.5 m was passed in equidistant steps of 5 cm. At each position 10 distance measurements were made for the SR-2 and 50 measurements for the SR-3000.
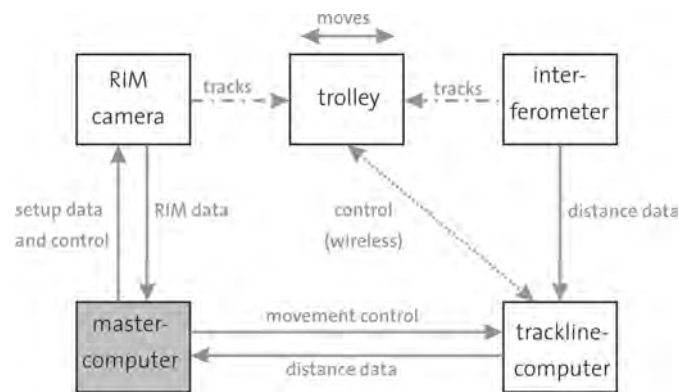
Figure 3.43: *Interferometer-supported distance measurement calibration track line at IGP at ETH Zurich and the setup overview for the distance calibration. Top: the mounted SR-2 can be seen on the right. The trolley with the flat target (center) moves automatically to predefined positions with a precision of about* 50 *microns. The accuracy (the offset in this case has an uncertainty) is about* 1...2 *mm. Bottom: the master computer controls the RIM camera and gives commands for the movement of the trolley. The track line computer controls the trolley and receives distance information of the interferometer. This trolley position and thus the distance information is sent to the master computer.*
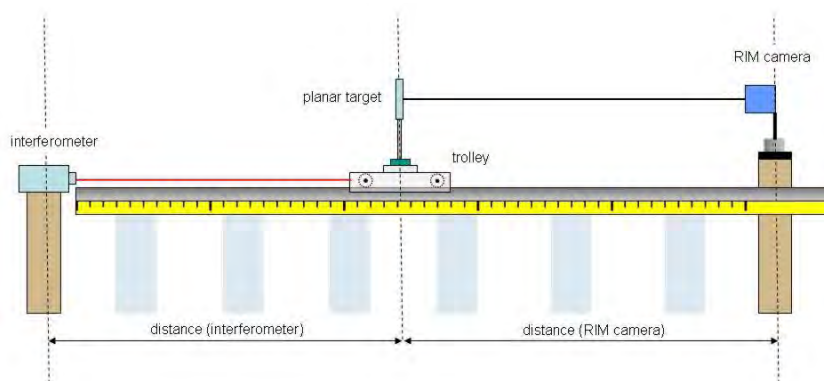
Figure 3.44: *Schematic principle (side view) of the calibration track line at IGP.*

In a first run, only center near pixels were investigated. For the SR-2, the pixel 80 / 62 was of interest, for the SR-3000 the pixel 71 / 87. The thermal conditions were held constant. The calibration track line is set up within a climate laboratory. Thus, the critical influence of thermal effects as shown in section 3.3.7 could be minimized. The laboratory is held at a constant temperature of $20°C$ and 50 % humidity.

The stability is of great importance because of the long time needed for the whole measurement process. It takes several hours to measure all positions.

SR-2   Figure 3.45 shows the calibration results for the SR-2. The additive look-up table for correction of the distance measurement is shown. In this case, no correction was made with respect to the amplitude. However, a high number of aspects can be observed:
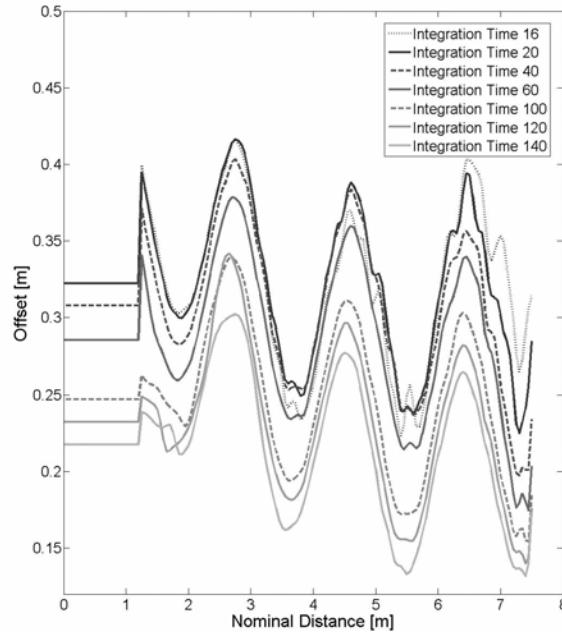
Figure 3.45: *Distance calibration results for the SR-2. The graph shows the final-look up tables for different integration times. The shift between the different LUTs is a result of different integration times. This effect has already been shown in section 3.3.7 (cf. figure 3.34).*

- Non-linearities within the modulation of the emitted signal of the LEDs lead, as it has been predicted, to cyclic effects (Lange 2000). The sinusoidal variation of the distance correction is a result of non-linearities of uneven order. This effect has a dimension of about $\pm 8\ cm$.

- A dependency between distance offset and integration time is present. A higher integration time leads to longer measured distances. This effect goes up to about $10\ cm$. The different integration time dependent measurements reflect the increasing precision of higher integration times. The graphs become smoother.

- A constant distance offset of about $30\ cm$ can be seen. This means that a part of the usable measurement range is lost for the measurements because of the shift between nominal and measured distances, and is thus lost out of the available $16\ bit$.

Due to the fact that the curve is smooth, a correction of the measurement seems to be meaningful. Nevertheless, irregularities occur. Figure 3.22 has already shown results of a distance calibration with targets with different reflectivities. The differences were not obvious but present. Therefore, the calibration of the SR-3000 was done with respect to the measured amplitude correction.

SR-3000   After the first investigations of the SR-2 were made, the SR-3000 was investigated in closer detail. In this case, only the three indicated integration times were analyzed. Again it becomes clear

that longer integration times lead to longer measured distances. Figure 3.46 displays the filtered but uncorrected measured data.

Figure 3.46: *Look-up table for the distance calibration of the SR-3000 with respect to the distance itself. The graphs show uncorrected data.*

The data were afterwards corrected by means of the functionality indicated in section 3.3.5 with respect to the amplitude of the demodulated signal. Figure 3.47 shows the result. It can be clearly seen that a scale occurs in the data (linear trend).
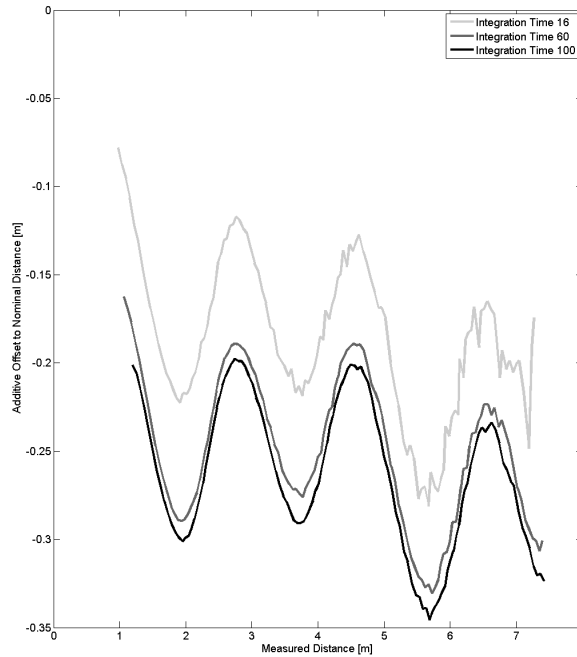
Figure 3.48 displays the obvious dependency between distance and amplitude. The longer the distance, the lower the backscattered energy and, thus, the lower the demodulated amplitude. This again leads to increased measured distance offsets.

However, this also has an impact on the precision of the measurements. Section 3.3.3 already dealt with the distance measurement precision. In section 3.3.5, a connection between amplitude and distance precision was proved. Figure 3.49 shows again that with an increasing distance and, thus, an decreasing amplitude, the standard deviation of the distance increases. Therefore, it clearly can be seen that the distance accuracy of a few millimeter can be achieved for close distances only. At about 3.5 m, the standard deviation for a single distance measurement reaches centimeter level. The results of this section remain stable as repetition measurements after several months indicated. Even though the sensor was set to high dynamic movements, the distance to distance calibrations do not change. This was expected, and proved by investigations.

So far only one central single pixel has been investigated. A full calibration of the sensor needs information of the whole sensor array. In order to capture distance dependent measurement data, the calibration was performed for several pixels. Because of the time-consuming calibration process described above, only a part of the full distance range was measured. From 1.46 m to 3.96 m every 10 cm, 50 distance measurements were acquired. The accuracy of the nominal distance was about $5 - 10$ mm. The pixels indicated in table 3.6 were investigated.

The results are shown in figure 3.50. The data are not corrected with respect to the amplitude of the measured data. The measurements fit to the measurements shown above, even though they were
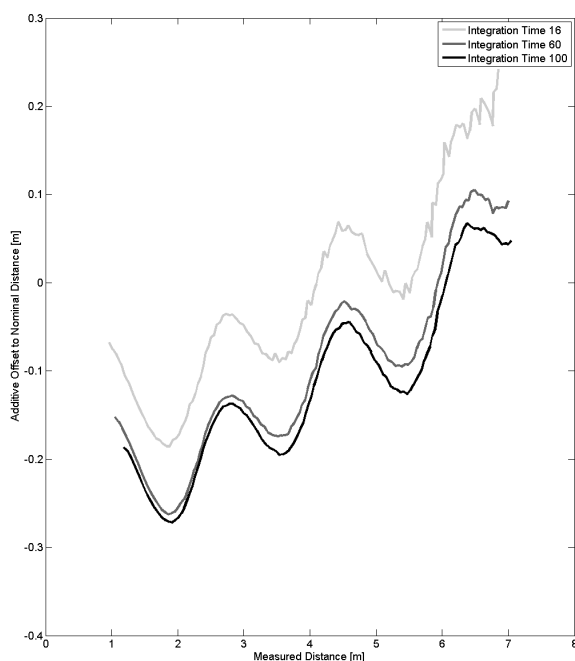
Figure 3.47: *Final look-up table for the correction of the distance measurements with respect to the distance itself. The data were cleared of amplitude effects (cf. section 3.3.5). The predicted cyclic effects can be clearly seen (compare Lange (2000)).*
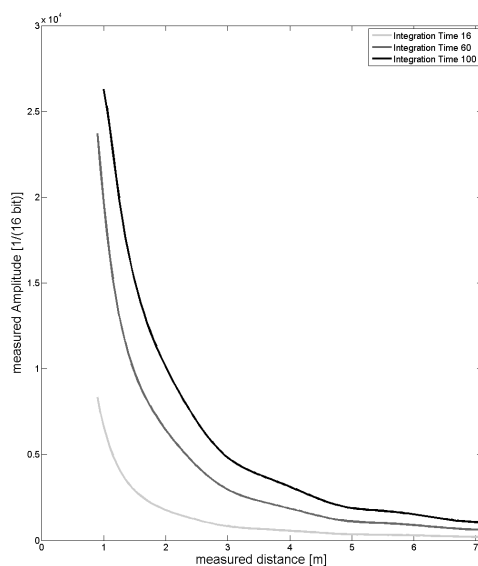
Figure 3.48: *Dependency between distance and the demodulated amplitude (SR-3000 and white target).*

done several months later. What can be observed, besides the different offsets of the data sets for the different pixels, is a phase shift, which depends on the location of the measured pixel on the sensor array. This dependency becomes clearer if the phase shifts are plotted over the sensor array. Figure 3.51 shows very clearly that the phase of the cyclic effect increases with the distance from pixel 0 / 0. Due to the
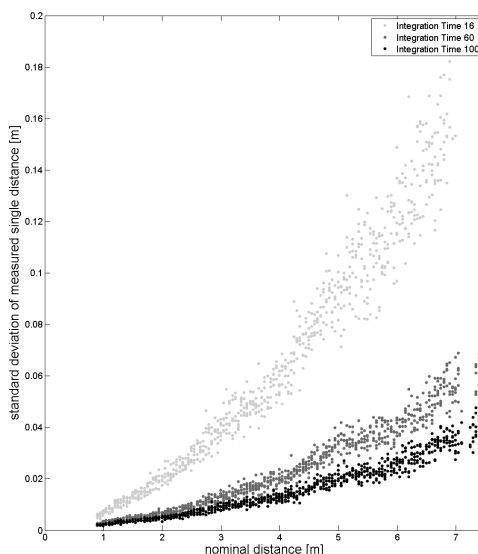
Figure 3.49: *Dependency between distance and distance precision (SR-3000). A white target was used for this investigation. It becomes clear that the precision of a few millimeters for a single measurement can only be verified for close distances.*

row	col
10	10
10	87
40	87
71	20
71	87
10	160
110	87
71	120
71	161
130	150
130	15

Table 3.6: *Distance calibrated pixels of the SR-3000.*

low number of investigated pixels and the uncertainty of the sinusoidal fitting, it cannot be said if the relation equals a planar dependency. In order to visualize the situation, a plane was fitted into the data (cf. figure 3.51). One of the main problems lies within the uncertainty of the phase shift. Even small discrepancies between the true phase shift and the calculated one result in large offsets and, thus, do not reduce the cyclic effect significantly. For a full calibration or investigation, the distance-to-distance calibration should be performed over the whole sensor array and a high number of pixels. Beyond this, the sensor mounting caused small movements of the sensor array with respect to the calibration direction. An improved mounting could increase the accuracy of the measurements. Nevertheless, the movement of the sensor in direction of the calibration track line was about 2 *cm*. However, this only changes the offset, not the phase.

This section has shown the classical distance calibration procedure. With respect to the nominal distance, the measured distance was captured and analyzed. Besides an offset and a cyclic effect, a phase
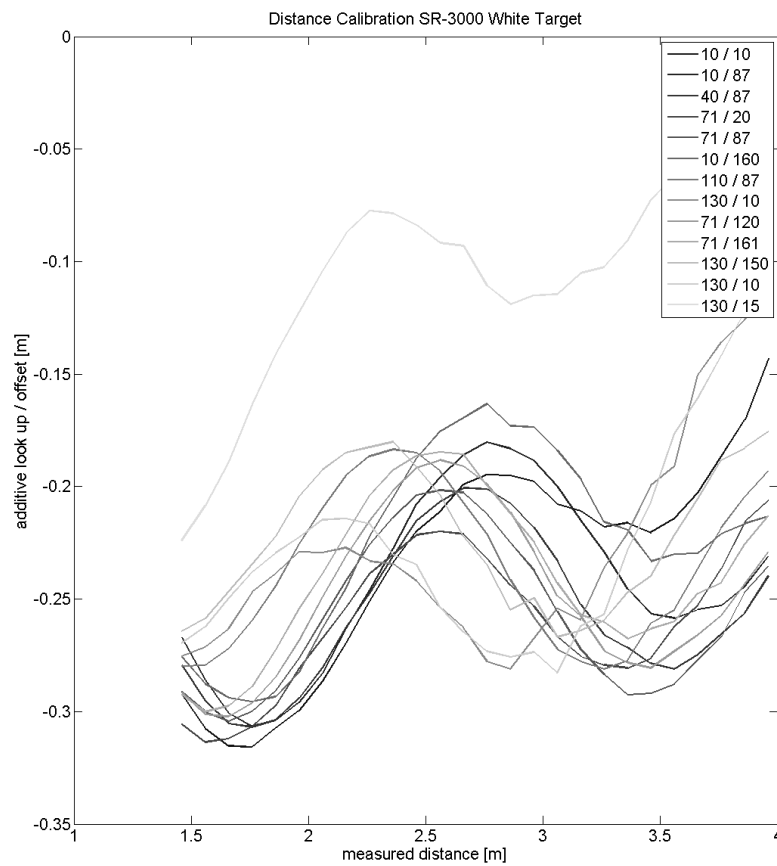
Figure 3.50: *Distance calibration of the SR-3000 (linearity) with respect to different pixels.*

shift of the cyclic effect was shown. Due to some uncertainties, the results of this section do not allow for a full correction of the measured data. Future investigations should increase the number of investigated pixels significantly in order to give a better understanding of the shown relations.
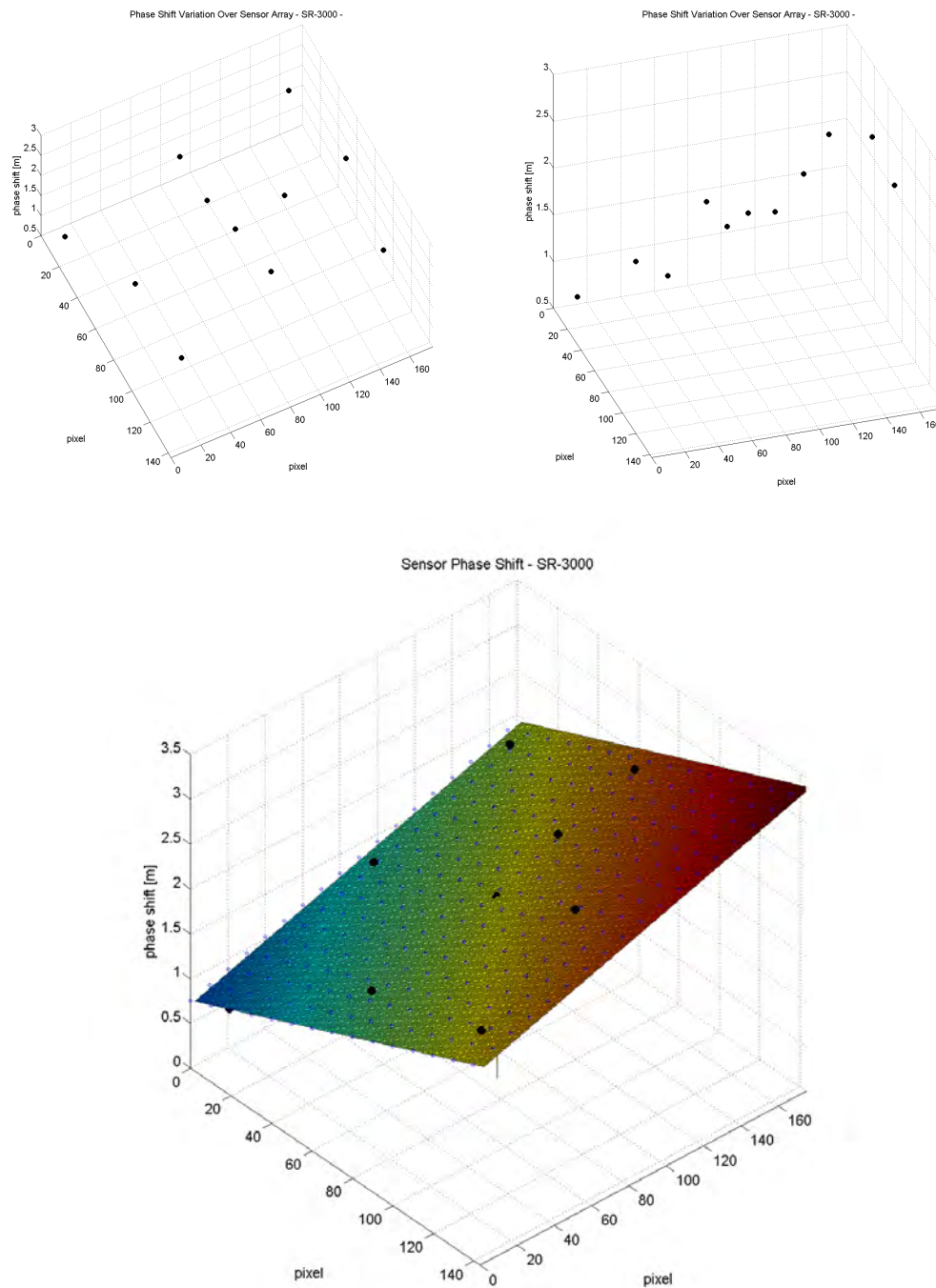
Figure 3.51: *Phase of the cyclic linearity effect for different pixels over the sensor array of the SR-3000. It can be seen, that the phase is not equal in all pixels. Thus, a compensation has to be made within a calibration.*

PMD 3k-S   Beyond the SwissRanger cameras, one of the PMD RIM cameras was calibrated with respect to the distance-to-distance relation. The setup equals the one shown above. In order to speed up the calibration process, the measurements were taken forth and back only twice. Two different integration times were chosen: 2 *ms* and 20 *ms*. The investigations were done on the calibration track line of the IGP.

Figure 3.52 shows the standard deviation of a single distance measurement for the different integration
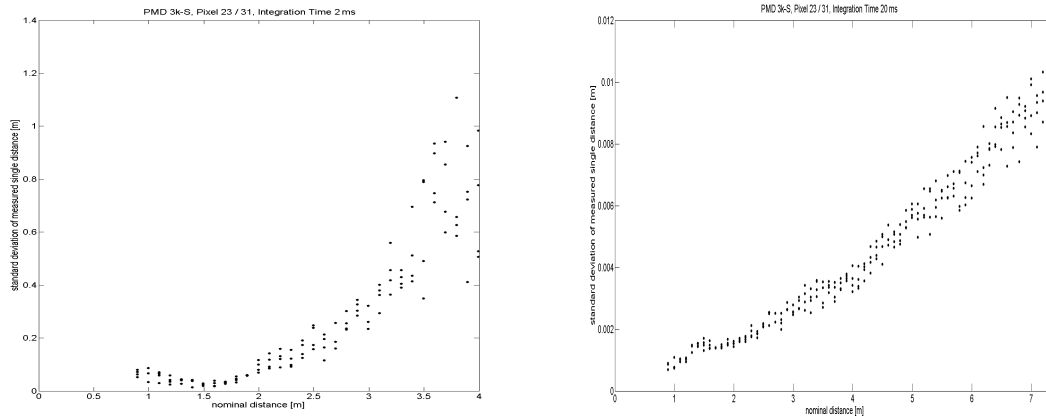
Figure 3.52: *Standard deviation of single distance measurement of the PMD 3k-S with respect to different integration times (2 ms -left- and 20 ms -right-) and different nominal distances. It can clearly be pointed out, that the lower integration time leads to highly disturbed data.*

times. What can clearly be seen is that the precision decreases with the distance, as expected, and is high for higher integration times. In case of the 2 *ms* integration time, the data become highly disturbed. In order to reduce these effects, a filter was applied. After the filtering of clearly wrong data, the look-up tables for the calibration of the distance measurements were calculated (cf. figure 3.53). A correction with respect to the amplitude has not been done. Again, the cyclic effect, already introduced in section 2.1.2.2 and verified above for the SwissRanger cameras, can be observed. It shows the similarity of both systems, which are based on the same measurement principle. The increasing amplitude with respect to the nominal distance can be seen in figure 3.54. The expected relation can be observed.
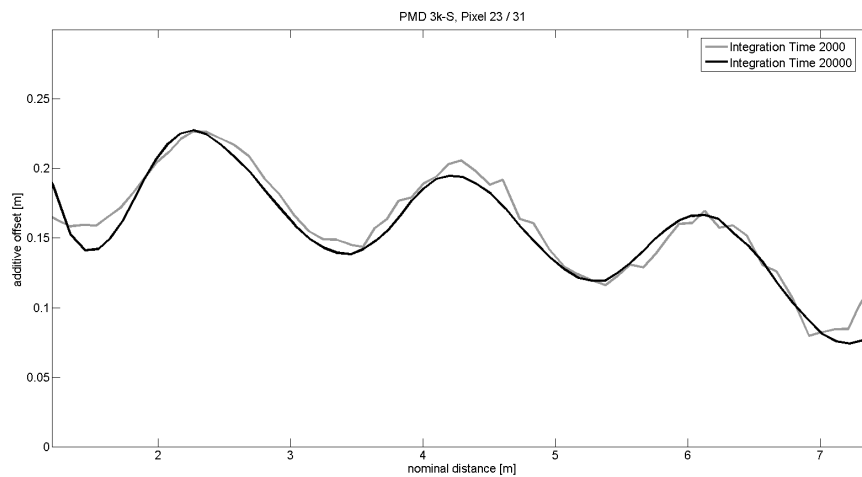
Figure 3.53: *Look-up tables for the calibration of the PMD 3k-S RIM camera. The cyclic effect has already been shown with the SwissRanger cameras. Even though the precision of the distance data has large values (cf. figure 3.52), the filtering leads to usable data.*

The PMD 3k-S camera does not significantly differ from the SwissRanger models with respect to the distance measurement linearity. A cyclic effect is present in nearly the same range in all systems. All systems have in common that the data are smooth and they are thus able to be calibrated to a large degree.
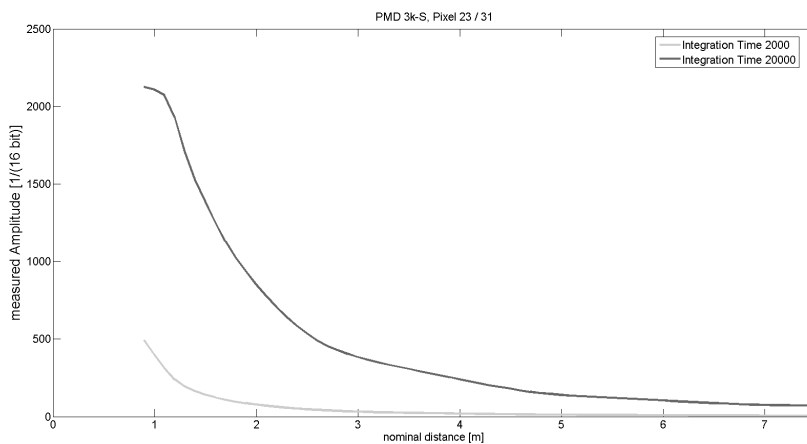
Figure 3.54: *Amplitude to distance relation of the PMD 3k-S camera.*

3.3.9   Fixed-Pattern Noise
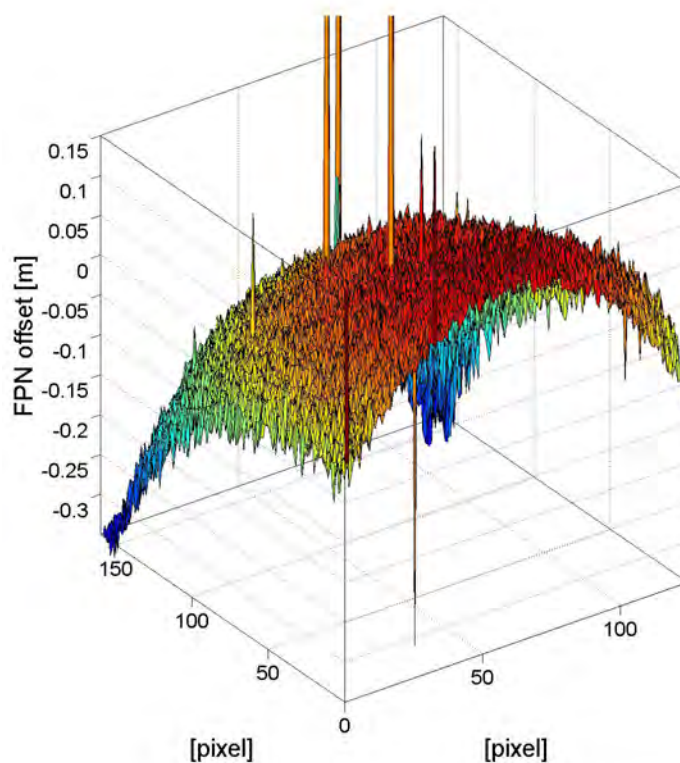
Figure 3.55: *Fixed-Pattern Noise of the SR-2. The nominal distance towards the measured wall was 2.452 m. The distance calibration outlined in section 3.3.8 has already been integrated. In this case no intensity and angle of incidence calibration is applied.*

For each pixel of a RIM camera, a distance offset has to be considered. The fixed-pattern noise (FPN) is equal to this distance offset in every pixel. It thus can be represented by means of a matrix which contains these offsets and which is added to the precalibrated data (intensity, distance-to-distance relation, and the angle of incidence). Figure 3.55 gives an idea of the uncorrected offsets which were

determined for the SR-2. In case of the SR-3000, the FPN was measured in a more sophisticated way and corrections were included. A determination of the FPN for a RIM camera can be done as follows:

- A geodetic total station is placed in front of a (white) wall. The wall is measured by means of the total station. The perpendicular projection of the camera's position to the wall is calculated and marked by means of a highly reflective target which can be found very easily in the amplitude image of the RIM camera automatically. The vertical offset between camera and total station has to be considered.

- The total station is replaced by the RIM camera, which is to be calibrated (figure 3.56). The RIM camera is aligned vertically towards the wall. The principle point's projection on the wall and the projection of the marked perpendicular projection of the cameras position have to fit to each other.

- For every pixel, the nominal distance towards the corresponding point on the wall is calculated. The photogrammetric camera calibration (cf. section 3.2) is included in the calculation.

- For every pixel, the angle of incidence is calculated.

- A number of distance measurements (e.g., 50) is acquired with the camera. These measurements are filtered (e.g., median) and corrected by means of the distance correction with respect to the angle of incidence (cf. section 3.3.6), the target's reflectivity (cf. section 3.3.5), and the distance-to-distance dependencies (cf. section 3.3.8).

- The differences between the calculated and the measured distances can be stored within a matrix which contains the additive correction values for each pixel.

Figure 3.56: *Fixed-Pattern Noise experimental setup for the SR-3000. The sensor is mounted on a tripod on which the total station has been placed before. The total station was used to determine the perpendicular projection of the camera position on the white wall. The SR-3000 then is oriented with respect to the optical center of the sensor towards the wall.*

Figure 3.57 shows the result. It becomes clear that the FPN is based on electronic reasons. The smoothness indicates that an electronic time delay, with respect to the injection of the reference signal, as well as the reflectivity based offsets may cause these distance offsets.
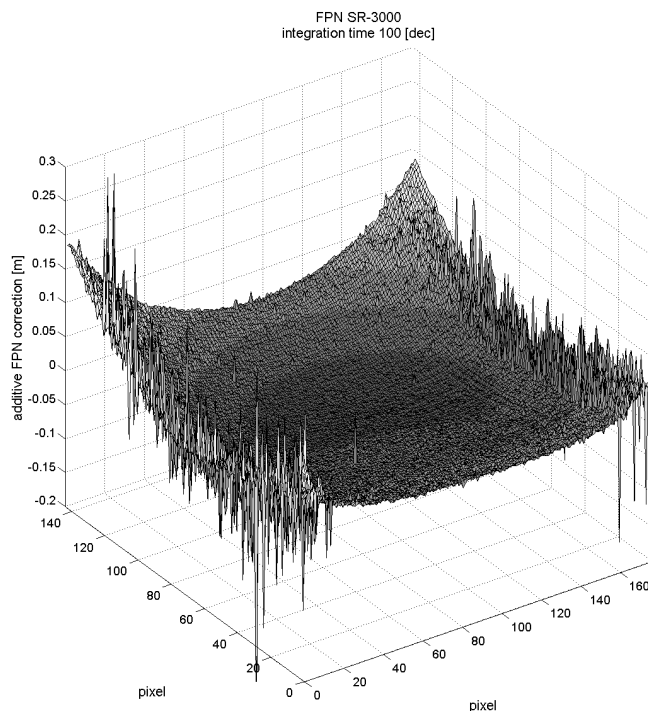
Figure 3.57: *Fixed-Pattern Noise of the SR-3000. The nominal perpendicular distance towards the measured wall was* 1.366 *m. The corrections with respect to the angle of incidence, the demodulated amplitude, as well as the deviations indicated in section 3.3.8 were already applied. The highly disturbed data at the edges can be explained by the low backscattered energy at the edges of the field of view.*

The FPN is the last aspect calibrated in this work. Thus, all calibration tasks could be combined. As already shown in section 3.3.1, the limiting factor of the SR-3000 so far is the scattering effect. Nearly all indicated investigations are influenced. Thus, a combination of all investigations and calibration aspects has thusfar not been successful.

3.3.10 Mixed Pixel

Another challenge in range imaging is well-known from laser scanning applications as well as all electro-optical distance measurement systems: so-called *mixed pixels* cause false data within the measured distance. Mainly two different kinds of mixed pixels can be differentiated: spatial- and amplitude-based mixing.

Spatial Mixed Pixel   A good description can be found in Hebert & Krotkov (1992). If two (or more) targets reflect to one and the same pixel, energy of both combines to one distance information.

Figure 3.58 displays the dependencies by means of a vector diagram (compare Merzinger et al. (1996)). The length of the vector corresponds to the amplitude of the signal. The center angle φ is a measure of the demodulated phase difference between the emitted and received signal (cf. section 2.1.2) and, thus, of the distance itself. All vector directions and, thus, all distances, can be measured even though both targets are not at this specific measured position. This leads to false data. Figure 3.59 displays such mixed pixels. It is shown that with RIM cameras, the vector diagram model is valid. Phenomena caused by mixed pixels are also called *tail of a comet*. The reduction can be done by means of edge filters. However, these pixels are lost for the measurements.
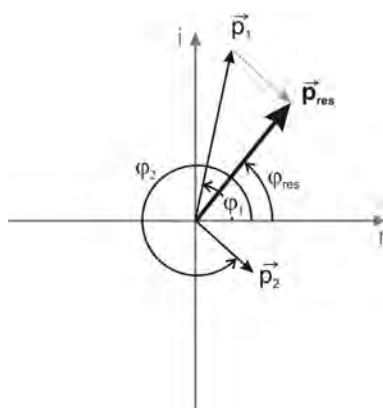
Figure 3.58: *Vector diagram for the explanation and visualization of the appearance of mixed pixels. The amplitude corresponds to the length of the vector. The center angle φ is a measure for the distance. The vector addition for two targets in the field of view of one pixel gives the finally measured resulting vector.*
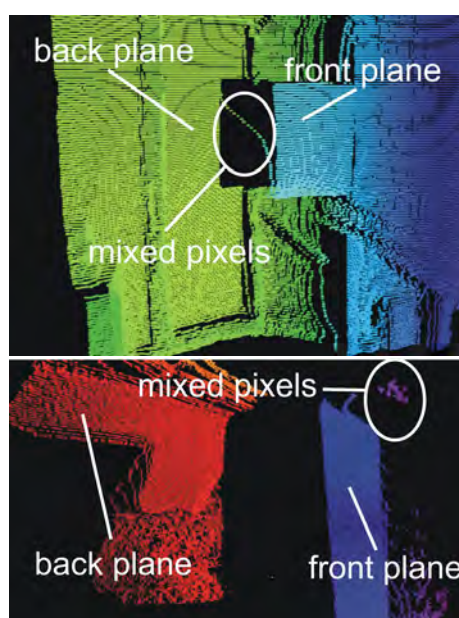
Figure 3.59: *Mixed pixels caused by two targets at different distances measured by one pixel. On the top the case which occurs most often is displayed because the environment mainly is smooth (edges affect the minimum of the measurements in an image): the measured distance lies between the fore- and the background. The bottom image shows the case when the mixed pixels lie in front of both planes.*

Amplitude Mixed Pixel   In order to get an idea of the influence of a single pixel's measured amplitude and distance on the entire sensor, the SR-3000 was set up in front of a black wall. The projected pixel's size is about 5 $mm \times 5$ mm. A white target was mounted at diverse positions on the black wall. The results of this experiment are shown in figures 3.60 and 3.61. For all, the pure black wall measurements were subtracted. Beyond the results from section 3.3.5 in figure 3.26, which validate the influence of the targets reflectivity on the distance measurement, another explanation for these findings can be seen here. Because of the setup, the neighboring pixels may be partially exposed to the white small target. Thus, different amplitudes within a single pixel occur. Because the sensing gates are distributed over the pixel, the distribution of the amplitude data leads to false correspondences of the demodulation measurements and, therefore, leads to false distance and amplitude data. In most cases, the distance measurement of the white pixel is not significantly affected. Especially figure 3.60 shows that the white pixel at position
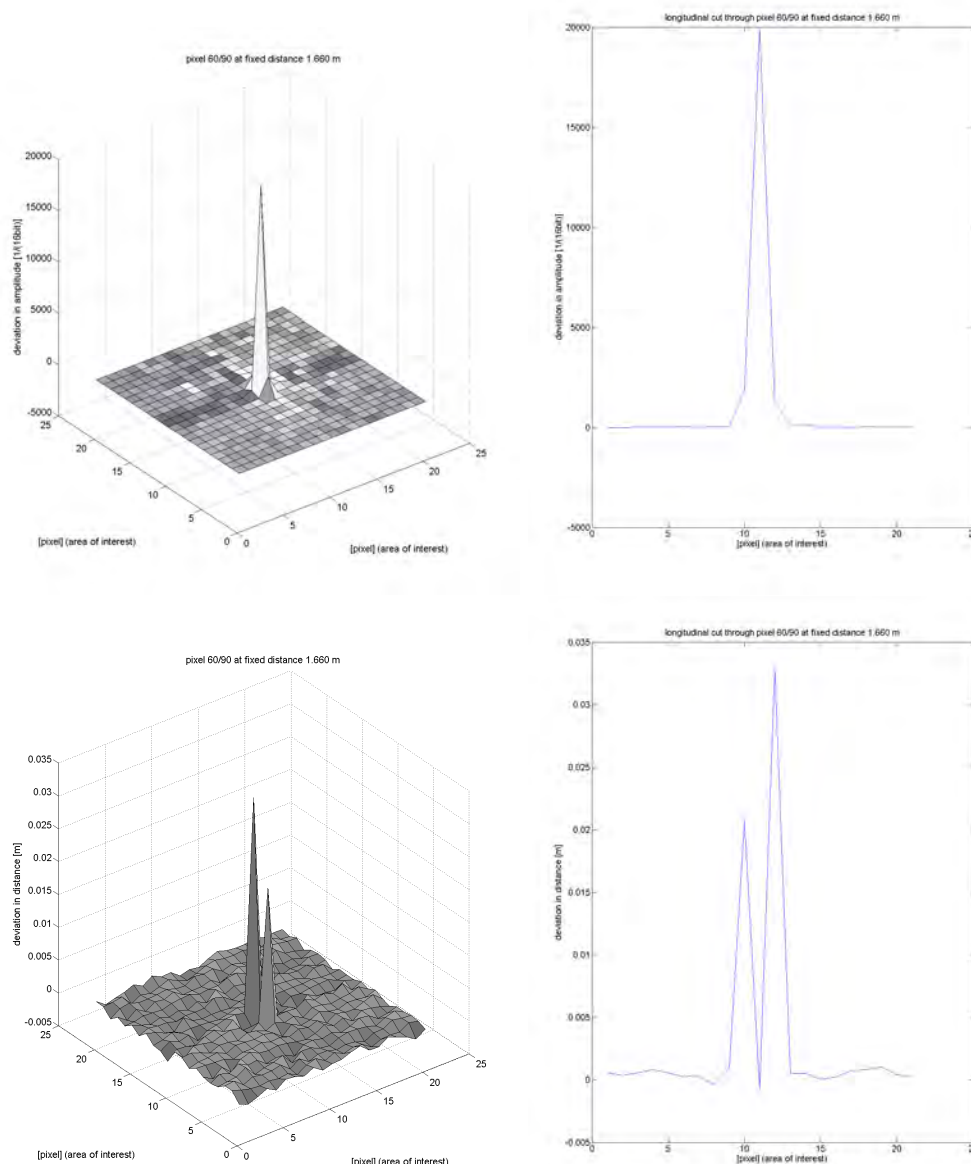
Figure 3.60: *Influence of a partially white pixel (position 11) on a black wall (SR-3000) for a center pixel (60 / 90). On the top, the influence on the measured amplitude can be seen. On the right, a lateral cut (in row direction) shows the increased amplitude of the white target, as expected. On the bottom, the influence on the distance can be seen. The corresponding white pixel does not show any deviation. Only the neighboring pixels have measured longer distances.*

11 measures a distance which fits to the surrounding distances. The amplitude is significantly changed in the white pixel. The only difference lies within the change of the distance and amplitude measurements of the neighboring pixels in the direction of the rows (144; smaller dimension of the sensor). The $(row - 1)$ pixel measures a distance which is significantly increased for about 3 cm. The $(row + 1)$ pixel measures different distances with respect to the position of the reference pixel on the sensor for another setup and a different investigated pixel (cf. figure 3.61). Even smaller measured distances can be observed. Thus, this effect seems to have a more complex structure. The measurements toward the retro-reflective target especially produce negative distance variations in neighboring pixels.
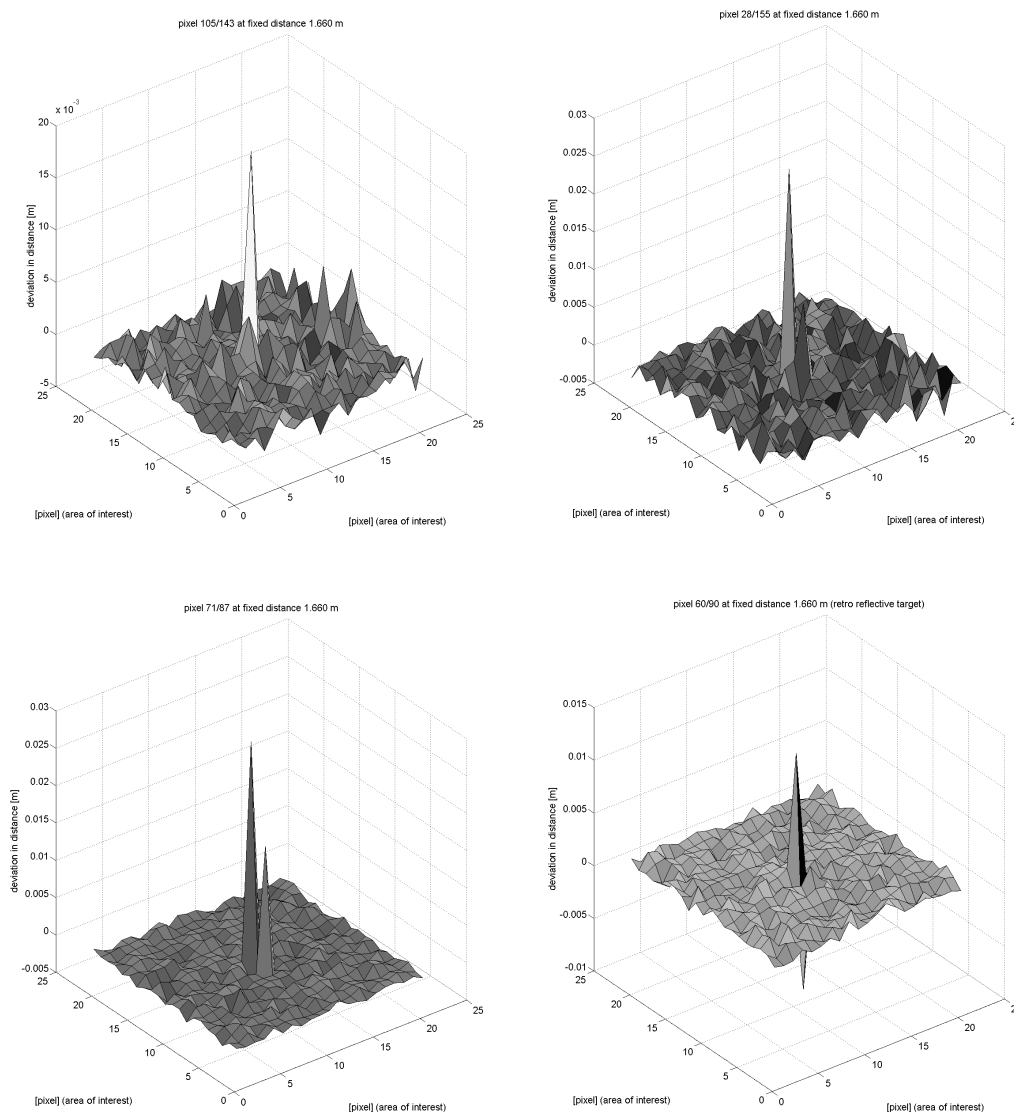
Figure 3.61: *Influence of a white pixel on a black wall (SR-3000) at different pixel positions. The effect is not equal in all pixels. Distance variations can be observed.*

3.4 Integral RIM Camera Calibration

In case of the calibration of the different components of a RIM camera, the pixel coordinates and the measured distances were considered, separately. An alternative approach is to treat the camera's secondary output, the 3-D coordinates, without any knowledge of linearity, Fixed-Pattern Noise, or lens distortions. Due to the deviations caused by lens distortions and uncalibrated measured distances, the calculated 3-D coordinates differ from the real coordinates to a large degree. The following approach treats the RIM camera more or less as a black box system. As Hennes & Ingensand (2000) showed, the combination of both, the component calibration as well as the system calibration approach, helps to improve the calibration procedure as well as it helps the avoid the dilemma of unavailability of information of complex systems. However, they have to be understood to be complementary to gain a maximum benefit.

In order to measure the three-dimensional offsets between the measured and the nominal coordinates, a specialized setup was developed. To measure nominal coordinates, a geodetic total station was used.

The total station was set up in front of a white wall close to the RIM camera SR-2. The total station
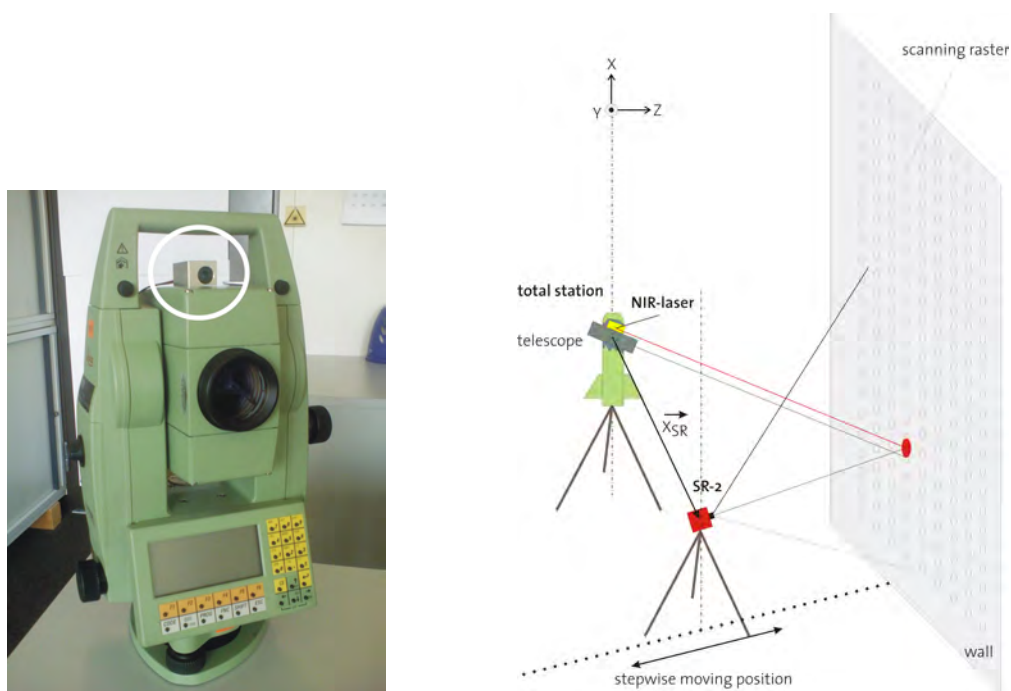
Figure 3.62: *Total station with NIR laser mounted aligned on the telescope (white circle) on the left. By means of this construction, the point, measured by the reflectorless measuring total station, can be signalized on a wall to be measured by the SR-2 (right). The NIR laser spot can be found in the intensity image very well.*

was equipped with an NIR laser, which was mounted in parallel on the telescope of the total station (figure 3.62). All components, the total station, the SR-2, and the NIR laser, where controlled by a computer. The basic idea is to measure points on the wall by means of the reflectorless measurement unit of the total station, then to signalize these points on the wall with the NIR laser, to find the marked points automatically within the intensity images of the RIM, and finally to measure the RIM with the laser turned off.

First, the SR-2 was set up in front of a white wall. In order to have points near the edges of the camera's field of view, the wall has to be large enough in its lateral dimensions. In case of the SR-2 with a field of view of about ± 25 *gon* in vertical and horizontal direction and a maximum distance of 7.5 *m*, the wall needs an extension of 5.9 *m x* 6.4 *m*. Because such a huge (white) wall is normally not available, a wall was chosen, that has the desired dimension in the horizontal direction and half the dimension in the vertical extension. Therefore, only about half of the SR-2's field of view is covered. For the measurements of the second half, the SR-2 was turned to the second face.

The second step was to set up the total station in a manner that the wall's orientation, as well as the position of the SR-2, could be measured properly. Both instruments were set up on tripods with centering devices. After the tripods of the total station and the SR-2 were levelled, a standard prism was set up on the tripod of the SR-2 and the later position of the SR-2 was measured. The SR-2 was swapped against the prism. Finally, a number of points was measured by means of a raster scanning on the wall by means of the total station. The same points were marked with the NIR laser and measured by the SR-2. For the detection of the laser dot positions, a specialized threshold and clustering filter was used which makes use of the high intensity of the laser dot within the intensity image of the SR-2. Some simple transformations lead to nominal coordinates provided by the total station as well as measured coordinates from the SR-2.

The result is a high number of points, measured as well by the total station with high accuracy and by the SR-2. Figure 3.63 displays the nominal coordinates (crosses) and the deviations of the coordinates
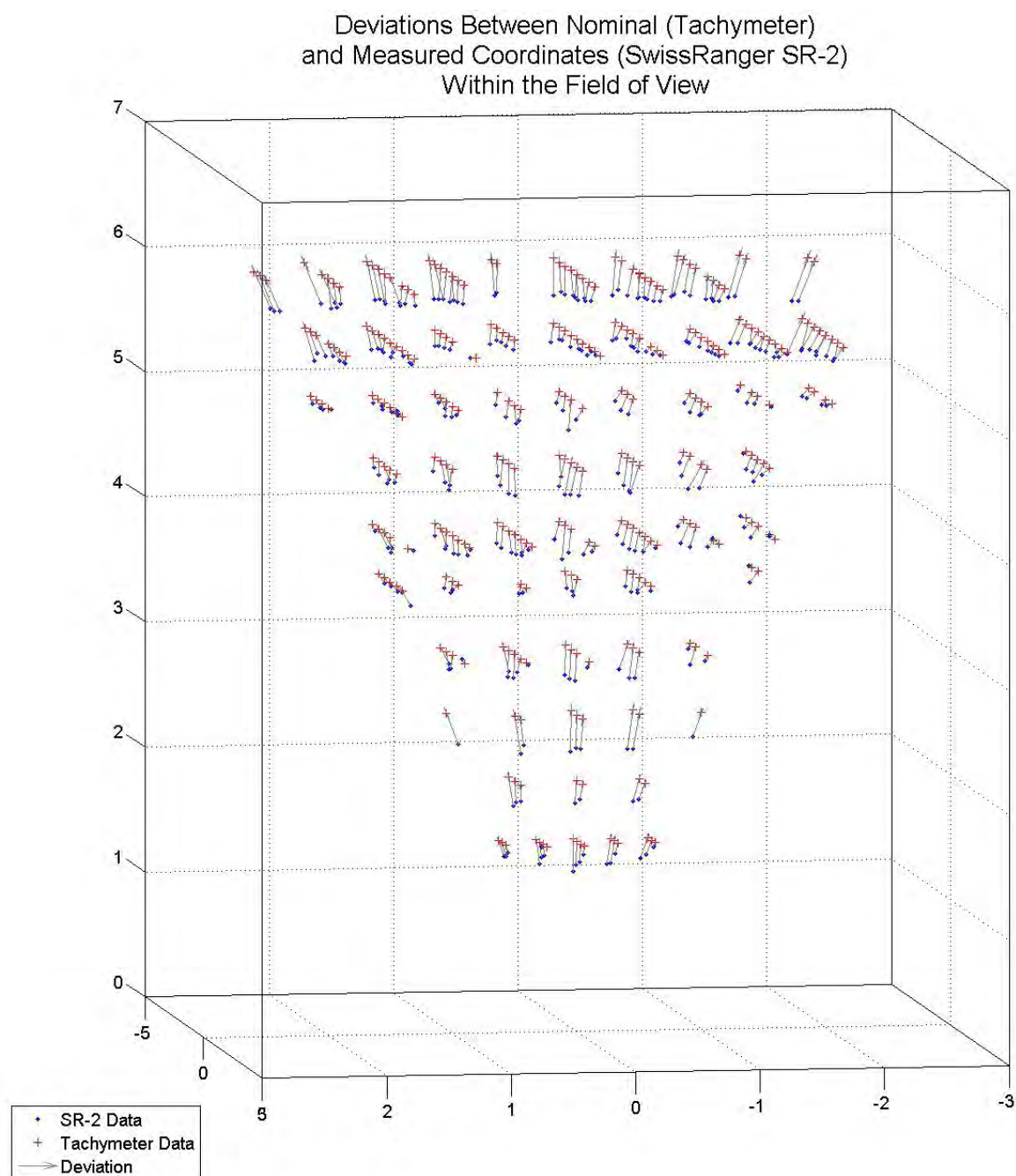
Figure 3.63: *Deviations of the nominal coordinates, measured by a total station (crosses), and the measured coordinates (dots) by the SR-2 (all axes in [m]). The deviations also show the cyclic effect already indicated in section 3.3.8. The measurements were made by means of a scanning total station, an NIR laser and the SR-2.*

from the RIM camera (dots). The deviations in the direction of the distance measurement dominate. Also the cyclic effect indicated in section 3.3.8 can be outlined. Figure 3.64 shows the deviations (three times scaled) from the camera's point of view. The radial distortions as shown in section 3.2.1 are visible as well, even though the principle point does not fit properly. Further investigations have to refine the setup as well as the measurement result analysis.

However, the generated vector field could be used for the calibration of the sensor's data in the manner of a 3-D look-up table. This calibration is only valid if some of the influencing parameters, like intensity
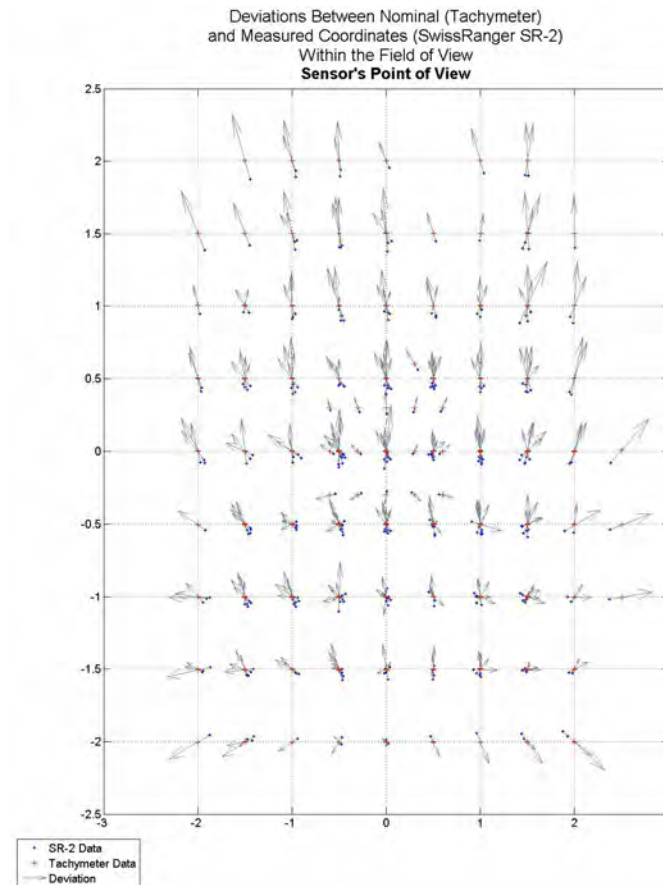
Figure 3.64: *Radial parts of deviations of measured coordinates (SR-2) and nominal coordinates (total station) (all axes in [m]). The radial distortion shown in section 3.2.1 can clearly be seen, even though a shift of the center occurs.*

and scattering, are calibrated in advance. One of the limiting factors of this calibration procedure is the time-consuming measurement setup as well as the measurements themselves. Unfortunately, the procedure shown here cannot be adopted to the SR-3000 because of the camera's background illumination subtraction ability. The NIR laser is not visible in the amplitude data. Thus, this calibration method can only be presented here as a proposal.

Nevertheless, the idea to calibrate a sensor in situ remains possible. This sophisticated approach may be followed for the specific application the RIM sensor is used in. Therefore, no final solution can be given, here. Beyond the calibration and data acquisition process indicated above, a possible setup could include spheres which can be extracted from the amplitude image and measured in the range image very suitable. Then, the integral calibration could become possible even with the SR-3000. Gächter (2006) already reported on successful usage of spheres for calibration purposes.

3.5   Conclusion

This chapter has shown comprehensive investigations on the characteristics, deviations, and potentials of different RIM cameras. Besides the SwissRanger SR-2 and the mainly analyzed SR-3000, one camera from PMDtec, the 3k-S, has been briefly investigated with respect to scattering effects and distance linearity. At first, the idea to calibrate the whole RIM sensor (SR-3000) became obsolete because of the unexpected high complexity of the influencing factors. The dominance of the scattering effect, indicated in section 3.3.1 in nearly all performed measurements as well as the influence of temperature-induced

drifts, made clear, that the calibration of the SR-3000 could only be done successfully, if scattering and the temperature drifts are reduced, or at least a suitable filtering has been developed in order to make the pixels independent from each other and free of drifts. The reduction of scattering was not considered to be part of this thesis. Temperature effects are treated separately in chapter 4. Finally, the enormous influence on the calibration procedure became evident when nearly all calibration procedures had been already performed and a complete system calibration failed. Nevertheless, the growth of knowledge about the properties of RIM cameras is extensively given within this work. Many different dependencies and characteristics have been investigated within this chapter. In particular, the analysis of non-linearities and the temperature dependent investigations show that the limit of the potential of RIM sensors has not been reached thusfar. The physical limits will become more obvious when a full calibrated sensor is available on the market. The sensor's potential will not only be reached in special cases then. Future developments, constructional and mathematical, will help to increase the accuracy of the sensors. Furthermore, the reduction of uncontrolled temperature effects will become more important. Chapter 4 shows a first step in this direction.

Chapter 4

Implementation of an Internal Reference

Up to this point, the commercial standard versions of the SR-2 (modified to 1-tap) and SR-3000 (and partially the PMD 3k-S) were investigated. This chapter deals with the investigations of a modified model of the SR-3000. The driving aspect for the development of an improved RIM camera can be seen in the high sensitivity of the distance measurement towards temperature changes and, thus, in a low reliability of the captured 3-D coordinates. Section 3.3.7 already gave a detailed analysis of the correlation between temperature and the distance measurement with respect to the warm up process as well as to the external temperature. These effects can reach several centimeters in distance and they are mainly of an erratic nature because of the cooling system, which is not able to stabilize the sensor's temperature adequately. For the geometric definition of three-dimensional points, the distance measurement is evident. Therefore, the distance measurement needs a calibration which stabilizes the data with regard to changes in the environment. The measurement of the temperature of the LEDs, as well as the sensor itself, could lead to mathematical temperature-based calibration functions or look-up tables. However, a multidimensional calibration procedure with respect to temperature and different integration times would be necessary. In geodetic high-precision instruments, a more sophisticated method is known: the internal reference distance path. It reduces drift effects by means of a relative or differential measurement setup. A reference path is also implemented within terrestrial laser scanners like the ZF (Zoller + Fröhlich) laser scanners (Zoller + Fröhlich 2007) and the procedure is also known from satellite navigation systems like the NAVSTAR GPS. The assumption is that a well-known or stable indicator underlies the same influences and, therefore, shows similar behavior as the quantity to be measured. This is vital for a reduction of occurring deviations. This chapter deals with the basic theory, technical possibilities, and finally with the implementation into the SR-3000. In order to validate the enhancements, some investigations of the camera will close this chapter.

4.1   Theory

As section 3.3.7 has already shown, the distance measurement of the SR-3000 is highly correlated to temperature effects. Due to different reasons, these correlations cannot be formulated adequately within functional dependencies, mainly because of their uncertain behavior. The SR-3000 houses a sensor for temperature measurements onboard. With help of this sensor, the fan is driven in order to stabilize the sensor's temperature. Because the temperature sensor does not measure temperature at all important points within the sensor and it underlies an inertia in time, the correction does not work properly. The passive cooling system is a drawback as well. Temperatures below room temperature and above about $30°C$ cannot be compensated adequately. The important parts whose temperatures influence the distance

measurement system are mainly the RIM sensor itself, the electronics, and the LEDs. In the following, an attempt to list the possible influences that can be compensated by means of a relative setup is given. The specific aspects of the distance measurement which can be affected are: *scale*, *offset*, and *linearity*. The possible influencing parameters which cause drifts mainly are:

internal temperature	warm up
	self-induced heating (by LEDs and electronics)
	external temperature
	ventilation
oscillator / clock	scale
	offset

Two main characteristics can be outlined to be affected by temperature as already described in section 3.3.7: the warm up of the system affects the first minutes of the distance measurement. This effect can easily cause several centimeters and is thus beyond the precision level of the sensor. Secondly, changes in the external temperature as well as temperatures beyond the semi-active cooling range of the system change the distance significantly by several centimeters as well.

Exemplarily, a solution for this problems is described in Rüeger (1996) and in Deumlich & Staiger (2002). An internal path for the radiated signal is shown for different realized electro-optical distance measurement systems. The goal of the internal path is to reduce drifts in the distance measurement, whether they result from temperature or anything else (see list shown above).
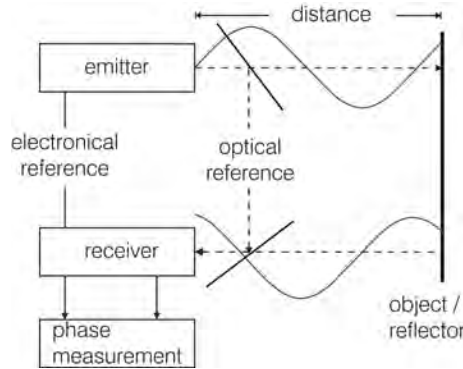
Figure 4.1: *Internal optical reference path within a distance measurement system.*

Therefore, a reference path is introduced into the distance measurement process (cf. figure 4.1). The length of this path is well-known and geometrically constant. Under the assumption that the distance measurement along the reference path underlies the same drifts and changes as the external distance measurement does, the external measurement can be corrected with respect to the drifts of the internal path. The measured distance D_{meas} is afflicted with the drift Δ_{drift} and a set of deviations ϵ as indicated in section 3.3 (ϵ stands for a sum of the different offsets and influences):

$$D_{ext\_corr} = D_{ext} + \Delta_{drift} + \epsilon_{ext} \tag{4.1}$$

The internal path distance $D_{internal}$ is assumed to be afflicted with the same drift and a set of deviations as well:

$$D_{int\_corr} = D_{int} + \Delta_{drift} + \epsilon_{int} \tag{4.2}$$

If the sets of deviations are set constant for the internal and the external path (zero, for example; assumption) the drift Δ_{drift} can be set to:

$$\Delta_{drift} = D_{int\_corr} - D_{int} \tag{4.3}$$

The internal distance D_{int_corr} is known (up to a certain level), deviations will be absorbed in the FPN of the system (pixel) as shown in section 3.3.9. The correction of the linearity (cyclic effect as indicated in section 3.3.8) and other influences, like the reflectivity / amplitude correction, have to be included, as well. They are neglected here for the sake of simplicity. Thus, the correction of the measured external distance can be done with respect to the drift by:

$$D_{ext\_corr} = D_{ext} + D_{int\_corr} - D_{int} \tag{4.4}$$

An important prerequisite is the simultaneity of the measurements of the internal and the external distance path. Normally, measurements of ranging systems are made serially. In order to keep the influence of this time difference small, the temperature gradient with respect to the acquisition frequency has to be small. Due to the fast acquisition speed of RIM cameras, this restriction is satisfied in most cases. Several different implementations are possible.

4.2 Implementation: ETH Solution

The main challenge with respect to an implementation of a reference path in RIM cameras lies within the structure of the back coupling of the emitted optical signal. Two basic strategies can be outlined. At first, the signal emitted from the LEDs (one, a few, or all) is led to all pixels. Thus, a true reference in all pixels is given and the drift term is unique for all pixels. The drawback of this method is the time needed for the switch between the internal and external reference path. A simultaneous measurement of both paths cannot be implemented due to the measurement principle. The mixing of the amplitude signals of the internal and external path would lead to a new mixed signal. Therefore, an optical switching would become necessary. The implementation of a reference path which includes the whole sensor array would help to avoid, or at least decrease, the FPN correction. All measurements could be corrected with respect to stable reference distances.
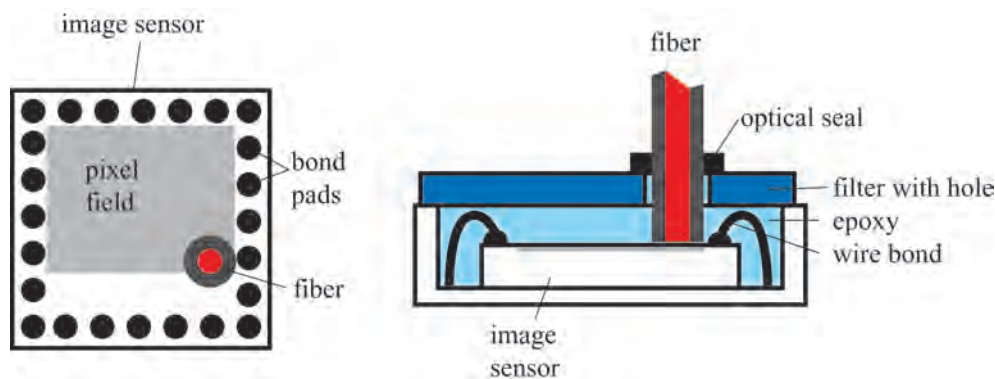
Figure 4.2: *Implementation of an optical fiber as a reference light path for the SR-3000.*

The second way of implementing a reference path is to capture the NIR radiation from the LEDs and route it to a section on the RIM chip, namely to a few pixels at the outer borders or on a separate pixel section. This was done in case of the investigations for this thesis. As figure 4.2 displays, an optical fiber, which comes from the LEDs, goes through the NIR-pass-filter above the sensor array and is mounted very close to the sensor array in one corner (pixel 1/159). Figure 4.3 shows the finally implemented fiber. In order to reduce scattering effects of the fiber, it was optically sealed and the mantle of the fiber was kept. This fiber is led through the housing of the optics and the casing of the camera to the LEDs. The coupling of the LEDs to the fiber (which cannot be displayed here due to restrictions by rights) leads to such a high amount of energy that a reduction by means of an intensity filter was needed in order to avoid saturation in the demodulation process. In chapter 3 it has been shown, that scattering is one of the

main problems within the actual RIM sensors. The implementation of the reference path fiber on the chip struggles with this problem, too. Nevertheless, due to the very close mounting of the fiber to the sensor array, the scattering of radiation out of the fiber to the sensor remains small. Future implementations have to take care of a further reduction of scattered radiation.

Figure 4.3: *Fiber mounted on the SR-3000 sensor. The fiber goes through the adapted IR-filter very close to the surface of the RIM chip.*

4.3   Validation

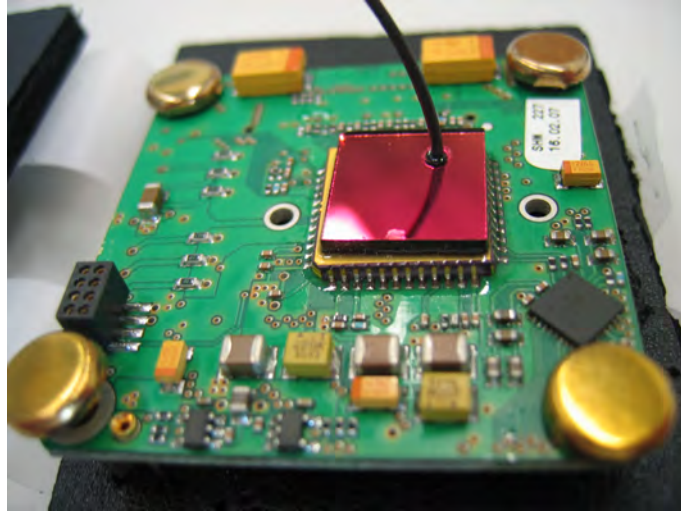In order to validate the functionality of the reference path, a number of investigations were carried out. This is substantial for the verification of the calibration process. It will be shown that the strategy introduced above will lead to a significant reduction of temperature-induced effects. The implemented reference path calibration will convey the potential of the method. The following experiments were done. First, two warm up processes were analyzed with respect to the ability of the reference path to reduce drifts. Afterwards, three different experiments were performed to help investigate the influence of the external temperature as well as of the intelligent cooling system on the distance measurements. This will indicate the potential of the relating reference path compensation. The first experiment will simply clear the functionality within a temperature range of $0°C$ to $30°C$ and a short external distance of about $1.166\ m$ nominal distance. The second one will deal with more extreme temperatures between $-10°C$ and $40°C$, but the same external nominal distance. The third setup integrates two different external distances in order to verify the compensation method for other pixels as well as longer nominal external distances.

4.3.1   Warm Up

First, a warm up sequence of the SR-3000 was acquired. The length of the chosen time segment from a warm up sequence is about $30\ s$. A drift in the distance data can clearly be outlined. The external measured distance has a drift of about $8\ cm$ within the shown $30\ s$, whereas the reference path distance drifts about $7\ cm$ in the same time. A correction by means of the internal reference path was done. As figure 4.4 shows, the warmup process of the camera is strongly compensated. However, a small remaining drift can be observed. This may result from differences in the temperature dependent characteristics of the pixels as well as the inertia of the reference pixel because of the larger lagging caused by the mounted fiber. A scale-dependent term is able to reduce this effect additionally. Also, a preceding linearity
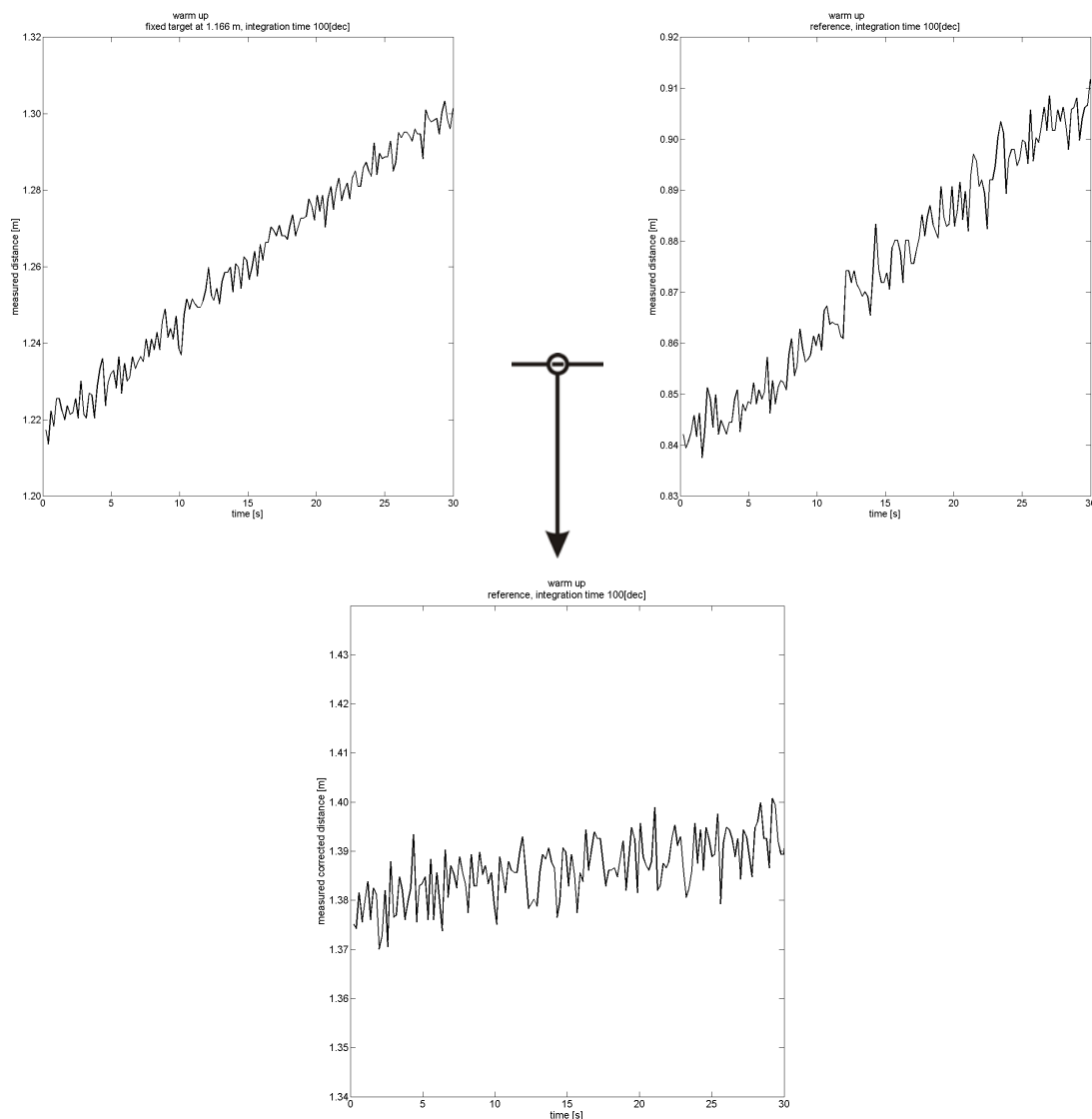
Figure 4.4: *Part of the warm up process of the SR-3000. The first* 30 *s of the distance measurements towards a fixed target (1.166 m) are shown: external distance (left), internal distance (right), and the corrected / reduced external distance (bottom). It can be seen that the warm-up-induced drift is significantly reduced by means of the linear model, as shown in equation 4.4.*

calibration could help here to further increase the reduction of the temperature effect by means of the reference path measurements (see section 4.4). Nevertheless, the warm-up-induced drift is reduced down to only about 20%.

A second experiment was performed with a longer warm up sequence until the distance measurements were stabilized with respect to the warm up of the sensor. The measurements range over 30 minutes (figure 4.5). Without compensation, the temperature-driven warm-up drift spans from the start of the sensor to about 8 minutes and ranges over more than 9 *cm*. Afterwards, other variation effects can be seen. When the reference path correction is introduced, the warm up sequence is significantly shortened to 1...2 minutes and the variation in the following measurements is reduced from about 1 *cm* to only a few (1...2) millimeters. Thus, the sensor is operable within the application much faster, and dead times of the system after the first start are minimized.
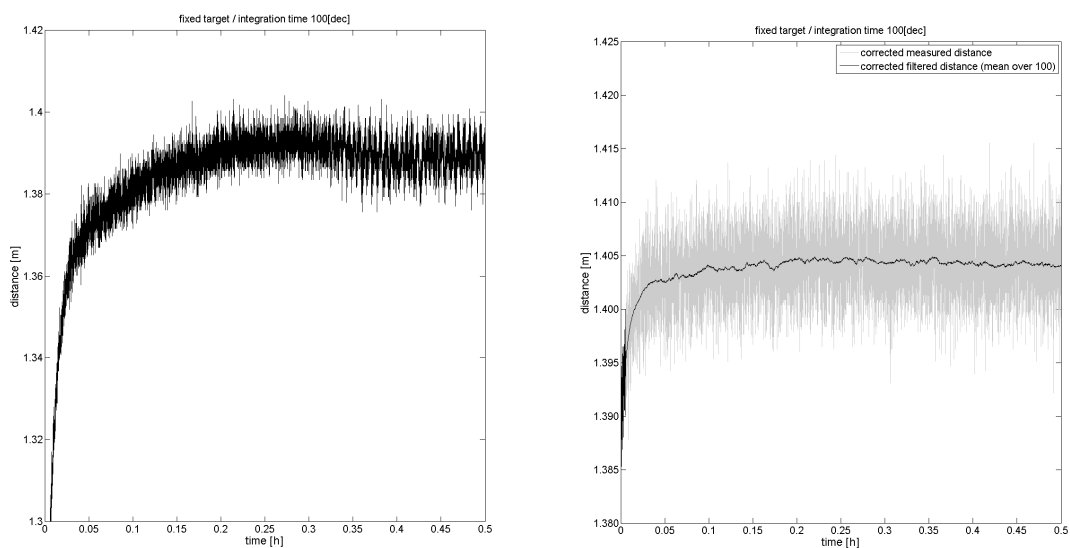
Figure 4.5: *Warm up sequence until distance data stabilization of the SR-3000. The external distance drift of several centimeters (top) is reduced by means of the reference path measurements down to a few millimeters (bottom) and is greatly shortened.*

4.3.2 External Temperature

The main goal is to reduce temperature effects, whether they come from external or internal changes. The verification of the assumed similarity of the reference pixel and the external measuring pixel with respect to their temperature behavior is in focus. The following investigations were done in the climate laboratory of the IGP (compare section 3.3.7). Results of three basic experiments will be shown here. Due to the risk of damaging the sensor, no temperature shock experiments were done. In all cases only one integration time was used: 100 [*dec*].

4.3.2.1 Experiment 1: Temperature Variation and Long-Term Acclimatization
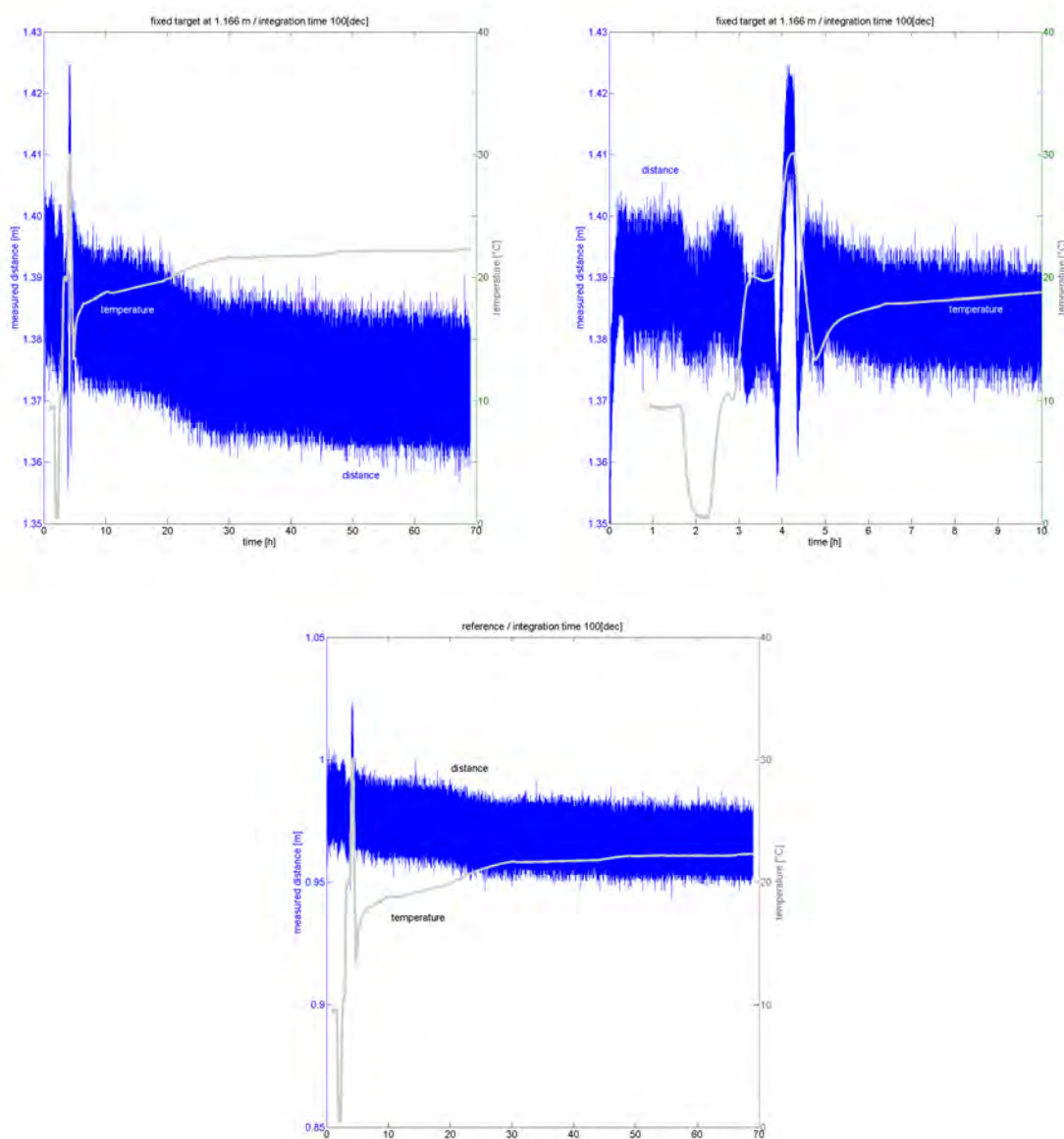
Figure 4.6: *Temperature experiment including reference path. This experiment consists of two parts. First, a temperature sequence (about $10°C$, $0°C$, $10°C$, $20°C$, $30°C$, and back to $10°C$) was performed. Afterwards, the temperature was set back to about $20°C$ in a period of ca. two days. The complete external distance measurement (top left), the extracted first hours of the external distance measurement (top right), and the internal reference distance measurement (bottom) are shown.*

First, the SR-3000 was set up in front of a white target at a distance of about 1.166 m and an angle of incidence of about 10° in order to avoid total reflections on the target in case of the appearance of condensed water on the surface of the target during the temperature experiment. Figure 4.6 displays the measurements. First, the external temperature was set to about 10°C. In the following the temperatures of 0°C, 10°C, 20°C, 30°C, and back to 10°C were realized. Finally, the air condition of the climate laboratory was turned off and the temperature assimilated to about 20°C over more than two days. It clearly can be pointed out that the temperature dependent distance varies several centimeters. The high correlation in distance between both, the external and the reference path distances, is obvious.
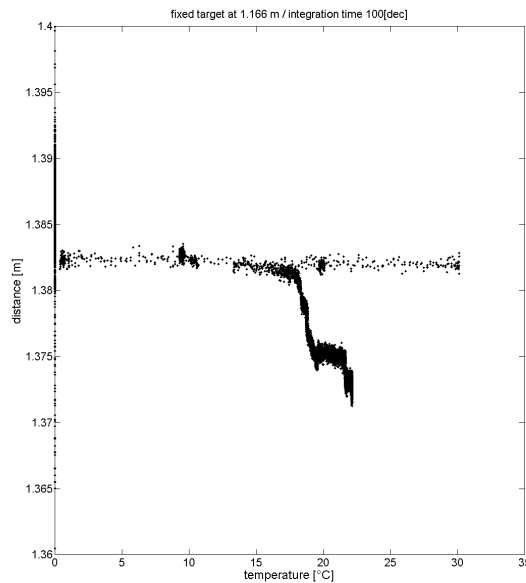
Figure 4.7: *Dependency between external temperature and distance measurements of the SR-3000. The dependency is not clear enough to allow for a correction.*

Figure 4.7 makes clear that the functional dependency between temperature and measured distance does not allow for a reliable correction. No clear dependency is visible. The external distance was corrected by means of the reference measurements with respect to equation 4.4 (cf. figure 4.8). Even though the noise becomes higher (addition of two noisy signals), the filtered data clearly have a lower sensitivity to temperature and varies only about ± 4 mm, whereas the original distance data changes about $\pm 2 - 3$ cm. Additionally, a temperature dependent long-term drift (warm up) is nearly eliminated, too.
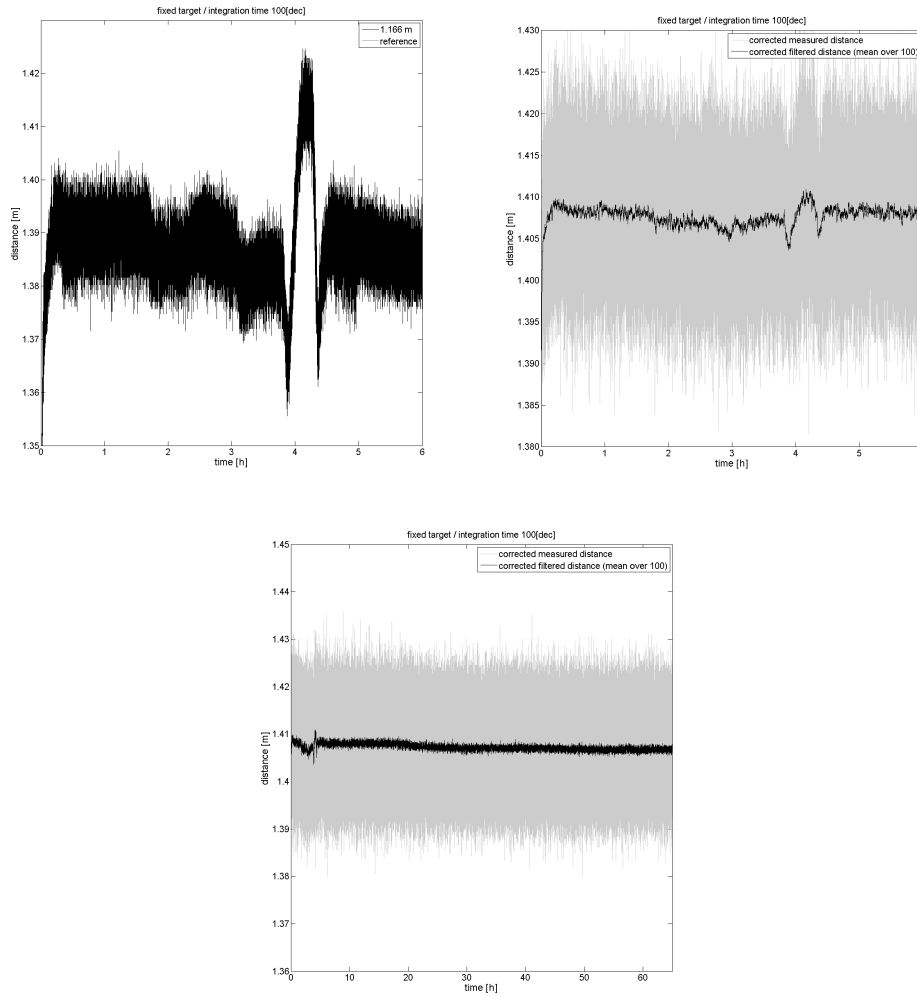
Figure 4.8: *Effectiveness of the reference correction on temperature-induced distance variations. The original distance measurements (top left) have been linearly corrected by means of the reference path measurements (top right). The whole corrected sequence can be seen on the bottom. A reduction of the variations (±2...3 cm) down to about ±4 mm has been achieved.*

4.3.2.2   Experiment 2: Extreme Temperatures

The second investigation was performed with more extreme external temperatures (cf. figure 4.9, left). The climate laboratory was heated from about $20°C$ up to $40°C$. After it was cooled down to approximately $-10°C$, it was heated up again. The distance variation can be seen in figure 4.9 (bottom). In particular, erratic fluctuations of the distance measurement at about $20°C$ make the calibration by means of a functional dependency more or less impossible. But again, the correlation between the internal and the external distance variation is quite high and suggests using the reference path measurement as a correction term (cf. figure 4.10). The reduction is significantly high and reaches a level of about 80% reduction. The remaining influences have to be analyzed in future investigations. Possible solutions are outlined in section 4.4.
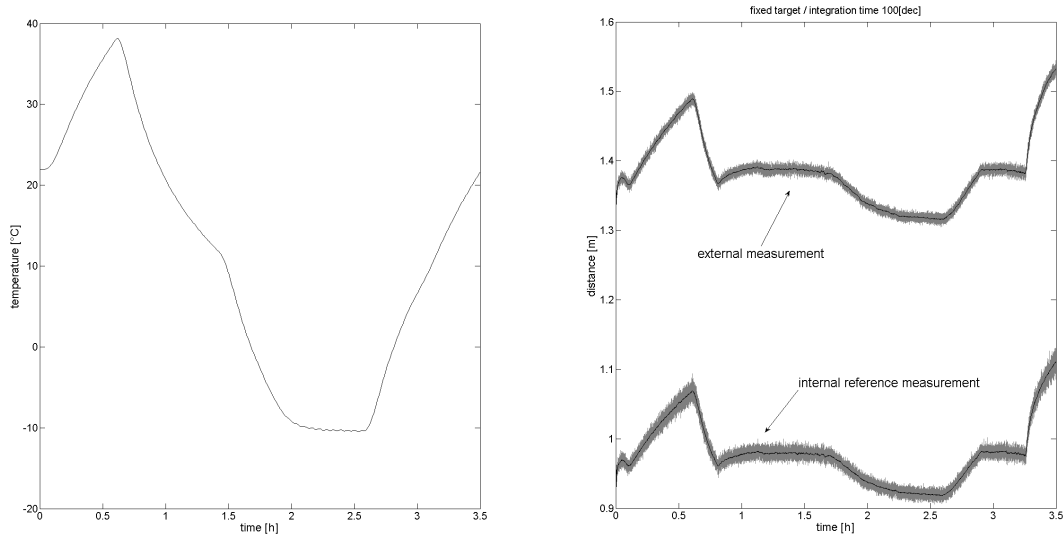
Figure 4.9: *Temperature experiment with internal reference path and extreme temperatures between* $-10°C$ *and* $40°C$ *(top). The distance measurements of the external and the internal paths show high correlation (bottom).*
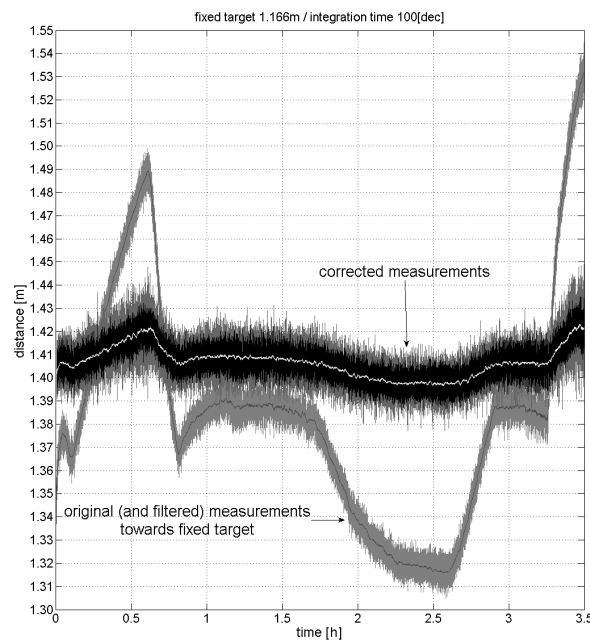
Figure 4.10: *Correction of the external distance measurements by means of reference path measurements. The reduction of the temperature effects lowers the temperature influence down to about* $10-20\%$.

4.3.2.3   Experiment 3: Two External Distances

A third experiment, which is similar to the first one (temperatures between $0°C$ and $30°C$) but which includes two different external distances, a longer distance of about $2.81\ m$ and a shorter one of about $1.79\ m$, brought very similar results. Figure 4.11 gives an overview of the measurements. The variation of the measurements reaches nearly $5\ cm$ for the mean-filtered distance measurements.
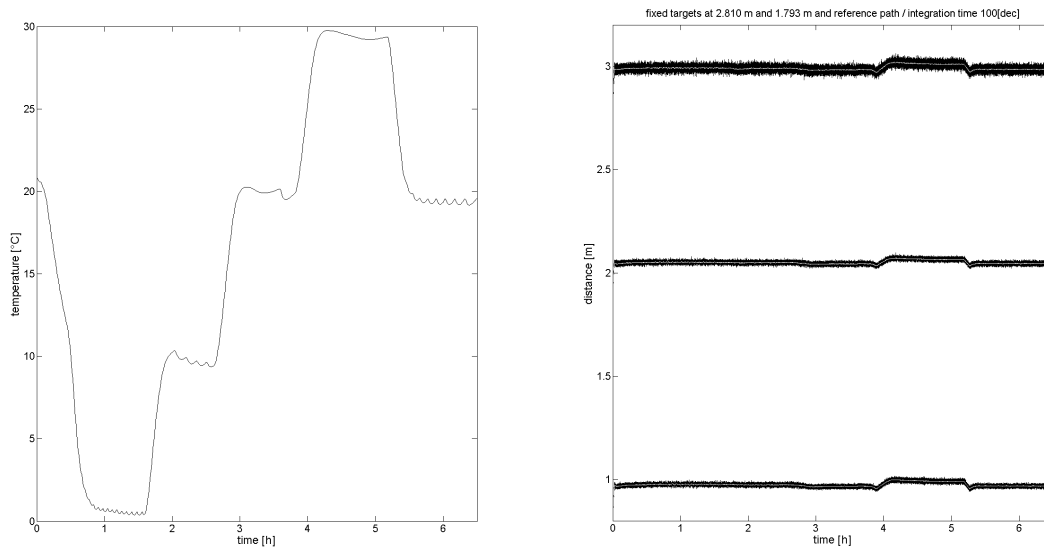
Figure 4.11: *Third temperature experiment with reference path. Temperature (left) and original as well as mean-filtered distance measurements towards two different targets and reference are shown (right).*

Again, a good reduction of the temperature drifts can be achieved, as figure 4.13 shows, after the reference path correction has been adopted (black curve). The introduction of a distance dependent scale for the reference distance allows for a reduction of the temperature-induced distance variation.

The results of the verification process show that the introduction of the internal reference path is quite effective. Ongoing investigations are supposed to reduce the temperature dependencies even to a higher degree. The introduction of a distance dependent scale or the modification of the reference path implementation increases the power of this method even more by:

$$D_{ext\_corr} = D_{ext} + D_{int\_corr} - D_{int} * scale + \epsilon_{ext} \tag{4.5}$$
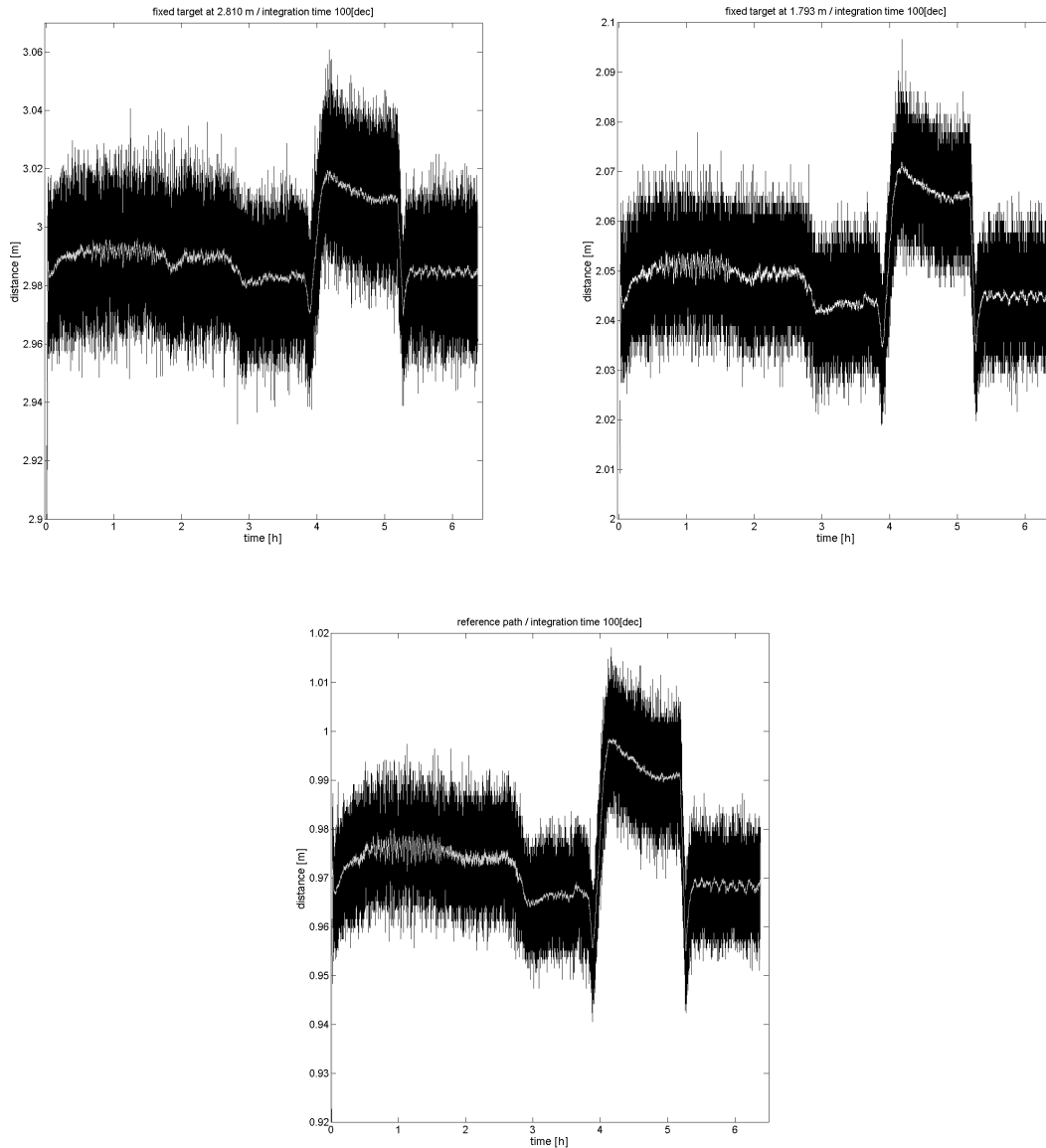
Figure 4.12: *Third temperature experiment with reference path: external path long distance (top left), external path short distance (top right), an internal reference path (bottom). The single measurements (original and mean-filtered) in detail. The variations go up to more than ±2 cm.*

4.4   Conclusion and Outlook

The potential of the internal reference path has been successfully shown. Even though the reduction of temperature driven drift effects by means of an internal reference path is common in geodetic distance measurement systems, the implementation into RIM cameras is new and not finally discussed. Many different ways of implementation are considerable. This thesis deals with one of the first-ever implemented reference path systems in range imaging. The investigations shown here testify to the strong power of this method. They will help to improve the technology and, therefore, utilize it for many applications. In the following, some possible improvements and considerations for future investigations will be given.

The mounting process of the optical fiber on the chip is time consuming. In a production process for mass market, the implementation would necessarily be different. A specialized filter element which contains the light path towards the reference section is recommended. Otherwise, in order to include the
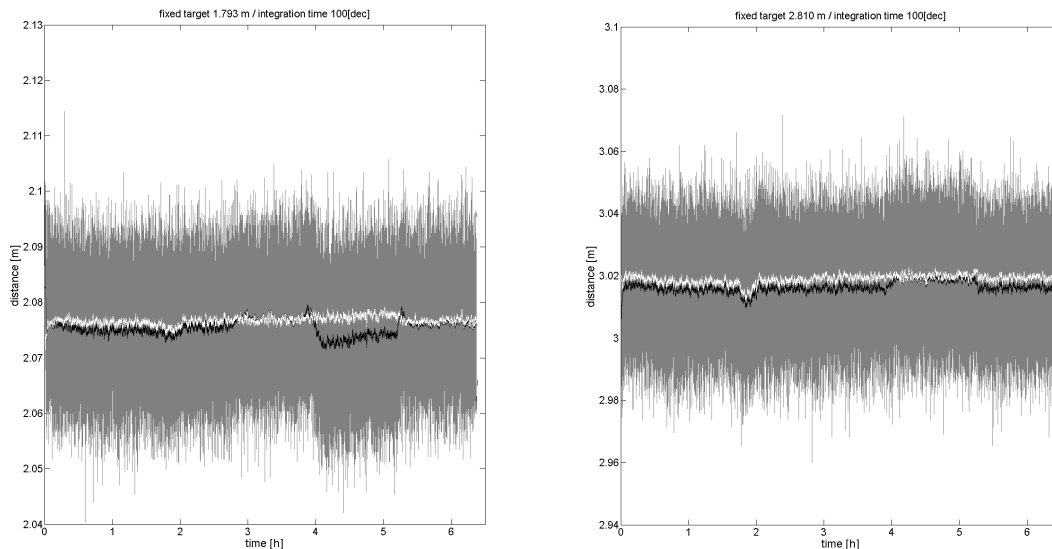
Figure 4.13: *Corrected distance measurements by means of an internal reference path. The straightforward reduction (black) helps to reduce the variation down to several millimeters. If a scale for the reference distance is introduced, the reduction effectiveness increases further (white curve).*

whole sensor array into the reference path setup, the fiber could be mounted to the edge of a glass plate. This glass plate could be mounted in front of the NIR-pass-filter plate. Thus, the reference radiation would impinge on the whole sensor array. In this way the complete array is covered by the reference path radiation. An optical switch could be used in order to turn the reference path on or off, and a change of the integration time could avoid an optical shutter for the exclusion of the external optical energy.

In case of the correction in figure 4.13, different but fixed scales for the whole data series for both distances were used. However, investigations have to follow which clear the influence of such a scale. One of the main suggestions is that the missing correction of the linearity causes these effects. Until now, no calibration data for the correction of the cyclic effect below 1.2 m measured distance are available (compare look-up tables in section 3.3.8). An estimation has provided that the dimension of the correction fits to the acquired data series and that the linearity correction, in combination with the reference path correction, would further help to reduce the temperature effects by:

$$D_{ext\_corr} = D_{ext} + \Delta_{linearity}(D_{ext}) + D_{int\_corr} - D_{int} * \Delta_{linearity}(D_{int}) + \epsilon_{ext} \tag{4.6}$$

Equation 4.6 shows the corrected model. In order to verify this assumption, a distance linearity calibration in the range of the variations of the reference path (about 85 cm) has to be done. Mainly it has to be clarified whether the temperature and clock drifts have an impact on the scale and the linearity of the system or just on the distance offset. Also the amplitude / intensity correction, shown in section 3.3.5, has to be considered.

Chapter 5

Conclusions

Range imaging cameras are relatively new on the commercial, civil market for measuring sensorics. Thus, the knowledge of their potential, as well as their limitations, are barely known. Out of the small number of available RIM cameras, three different models were chosen and investigated. This thesis deals with the newly available RIM technology implemented different camera sensors. After a few publications which are available that describe the basic technology as well as first implementations out came out that the number of investigations on the characteristics of these implementations is poor. Due to the fact that these sensors are of significant interest for the use in geodetic applications, two of the available sensors were bought (SR-2 at the end of 2003 and the SR-3000 in 2006), both provided by CSEM / Mesa Imaging (Switzerland). After first experiences were made with the SR-2, the main focus was laid on the investigations of the SR-3000. This thesis contains results from investigations of three different sensors. Besides the SR-2 and the SR-3000, a sensor from PMDtec (Germany) became available for some time. In the following a brief summary of this thesis as well as an outlook to future advancements of the described RIM technology is given.

5.1 Summary

This thesis introduced the motivation for this work in the first chapter. Besides different application, which will make use of the RIM technology in future, but which demand higher accuracies, the investigation and development of the potential of RIM stood in the foreground. The increase of the knowledge about RIM sensors and their properties, potential and limitations was one of the main aspects. The introduction was followed by the presentation of the theoretical basics of distance measurement as well as imaging techniques in the second chapter. Further on, the second chapter contained the basics of range imaging technology (chapter 2). Besides basically two different implementations, direct and indirect Time-of-Flight, focus was laid on the technology which is used within the SwissRanger and PMD cameras. The theoretical limitations were outlined.

Chapter 3 of this work gave an overview about the different problems of RIM cameras. The first intention for the objectives of this thesis was to simply calibrate one RIM camera in order to use it in applications as a precise 3-D measurement sensor as indicated in sections 1.1.1 and 1.1.2. After the first experiments, it became obvious that the calibration of such a system is much more complex than expected. Because of the deviations between nominal and measured coordinates, a calibration of the different sensors became essential. Accurate and reliable coordinates are fundamental prerequisites for most applications. Thus, the calibration became the main goal of this thesis. The desire for suitable calibration routines is very high, as the international feedback of other researchers and users of RIM sensors evinced. Unfortunately, the measurements of the SR-3000 camera were finally indicated to be dominated by one of the main drawbacks of this sensor technology. The silicon surface partially acts

like a mirror and, thus, produces scattering effects within the sensor. This leads to false data due to the correlations of the diverse pixels. Also temperature-induced drifts of the distance measurements lead to significant errors. In the following, most of the made investigations were influenced by these effects and calibration rules cannot yet be given. Nevertheless, the investigations help to understand the limitations of the technology. Besides the influence of the chosen integration time and the reflectivity of the captured object, the emitting system and the angle of incidence have an impact on the distance measurement precision. Especially the distance linearity investigations of the different sensors were of interest. It has been shown that the precision of the SR-3000 is much higer than the accuracy of the system. Thus a reduction of systematic effects can be performed by means of calibration. However, the numerous experimental results show the high potential of the technology. The importance of a calibration cannot be underestimated. Most of the effects remain strongly linear, or at least stable and continuous. Thus, they can be corrected by means of suitable calibration routines in the future.

One of the main achievements of this work is the introduction of an internal reference path in order to reduce temperature effects. Chapter 4 has shown the significant higher accuracy and increased stability of the distance measurements because of the implemented reference path correction. The simplicity of the method certainly is one of its strengths. Temperature influences as well as other drifts in the distance measurement are increased to a large degree. If and how the internal reference path will be introduced into future camera models depends on investigations about the optimal implementation and economic analysis. The results presented here confirm the need for an internal reference path within RIM cameras. The benefit is a strongly reduced drifting of distance data acquired by RIM cameras with respect to temperature and other influences.

This thesis increases the insight into different aspects regarding precision and accuracy of RIM cameras. It is one step towards the usage of RIM sensors within geodetic applications.

5.2   Outlook

This thesis partially shows the great potential of the emerging range imaging technology, but also limitations of existing systems were indicated. As the investigations and developments, shown in chapter 4, made clear, the internal reference light path will become an important tool for a significant improvement of RIM cameras.

Also the scattering effect, described in section 3.3.1, which until now remains one of the limiting factor for the accuracy of the analyzed camera, is matter of strong investigations. Besides a mechanical coverage of the reflective, non-active parts of the semiconductor, a highly promising proposal by means of mathematical filtering of the data was given by Mure-Dubois & Hügli (2007).

Another aspect is the sensitivity of the conversion of radiation into charges. SPAD sensors are one way to enhance sensitivity. Another approach was introduced by Schwarte (2005a) (cf. figure 5.1). The basic idea is to amplify the incoming radiation by means of a strong electric field (100 V...1000 V). Therefore, even distances up to 1 km could be measured. The proof of the functionality has to be given in the future.

Many small improvements will increase the abilities of RIM cameras in future. However, until now they represent one of the most sophisticated approaches in the world on three-dimensional coordinate measurement systems with respect to the simultaneous capturing of spatial data and online 3-D coordinate generation up to video frame rate. As Hauke & Bömer (2005) and Kohoutek (2006) already have shown, RIM sensors will also provide safety applications in the future. They will be part in everyday life. Also robotics (Kubacki & Pfeiffer 2005) have to be named here. Not only for the safety of workers within a construction process where robots are integrated, but in autonomous robots with diverse tasks as well, RIM technology will increase the possibilities and abilities of such systems. Many applications only will become possible because of RIM sensors.
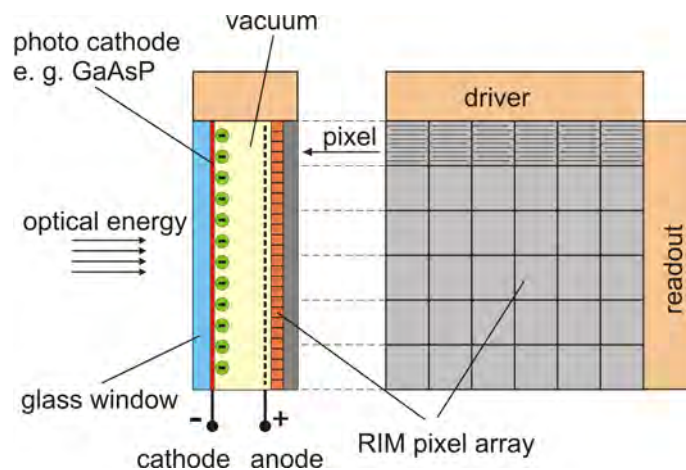
Figure 5.1: *Amplification of the incoming energy for future RIM sensors. This method uses a strong electric field (*100 *V ...*1000 *V) to amplify the photon-generated energy. Thus, longer distances can be measured (*1 *km) (Schwarte 2005*a*).*

While this thesis was written, many improvements in RIM technology were published or were about to be. This clearly reflects the fast development and the high demand for this kind of sensor.

Appendix A

SwissRanger SR-2 Specifications

General Characteristics:

Modulation Frequency	20 MHz
Non-Ambiguous Distance Range	7.5 m
Measured Demodulation Depth	40 %
Pixelfield	6.27 mm (39.2 μm x 160 $pixels$)
	6.80 mm (54.8 μm x 124 $pixels$)
Number of LEDs	48

Characteristics of the Lens:

Lens Manufacturer	Kogaku Universe
Focal Length / F/#	8 mm / 1.4

Characteristics of the Filter:

Filter Manufacturer	MK Photonics
Center Wavelength / Bandwidth	882.5 nm / 65 nm

Characteristics of one LED:

LED Manufacturer	Vishay Semiconductors
Wavelength of LEDs / Spectral Bandwidth	870 nm / 40 nm
Beam Divergence	$\pm22°$
LED Current (Average)	70 mA (average, if duty cycle = 100 %)
Optical Power of one LED @ 70 mA	17 mW (average, if duty cycle = 100 %)

Characteristics of the Illumination Board:

Mean Optical Output Power (CW)	800 mW

Table A.1: *SwissRanger SR-2 specifications (handbook).*

Appendix B

SwissRanger SR-3000 Specifications

General Characteristics:

Modulation Frequency	$20\ MHz$
Non-Ambiguous Distance Range	$7.5\ m$
Pixelfield	$7.04\ mm$ ($40\ \mu m$ x $176\ pixels$)
	$5.76\ mm$ ($40\ \mu m$ x $144\ pixels$)
Number of LEDs	55

Characteristics of the Lens:

Focal Length	$8\ mm$

Characteristics of the Filter:

Center Wavelength / Bandwidth	$870\ nm$ / $80\ nm$

Characteristics of one LED:

LED Manufacturer	Vishay Semiconductors
Wavelength of LEDs / Spectral Bandwidth	$850\ nm$ / $35\ nm$
Beam Divergence	$\pm 25°$

Characteristics of the Illumination Board:

Mean Optical Output Power (CW)	$1\ W$

Table B.1: *SwissRanger SR-3000 specifications (handbook).*

Appendix C

Photogrammetric Calibration Results for the SR-3000 Provided by Australis

```
                  Australis Bundle Adjustment Results: Camera Parameters

                              15 March, 2007    09:03:53

Project:  C:\Documents and Settings\fabio\My Documents\timo\Project.aus

Adjustment: Explicit Object Point Control
Number of Points: 25
Number of Images: 16
RMS of Image coords:    4.01 (um)

Results for Camera 1     Swissi      Lens

Sensor Size         Pixel Size (mm)
  H     176             0.040
  V     144             0.040

  Camera    Initial        Total         Final        Initial         Final
 Variable    Value       Adjustment      Value       Std. Error     Std. Error
    C        8.0331       -0.03755        7.9955       1.0e+003     1.387e-002 (mm)
    XP       0.1021       -0.00241        0.0997       1.0e+003     1.969e-002 (mm)
    YP       0.4743       -0.03481        0.4395       1.0e+003     2.027e-002 (mm)
    K1   2.15486e-003  -4.972e-004   1.65764e-003     1.0e+003     3.884e-004
    K2  -3.09409e-005   6.878e-005   3.78432e-005     1.0e+003     6.179e-005
    K3   7.41115e-007  -3.393e-006  -2.65190e-006     1.0e+003     2.825e-006
    P1   2.54375e-004   6.309e-005   3.17463e-004     1.0e+003     1.172e-004
    P2  -2.33932e-004   9.018e-005  -1.43750e-004     1.0e+003     1.198e-004
    B1  -3.32010e-003   2.761e-003  -5.59513e-004     1.0e+003     4.216e-004
    B2   1.50197e-003  -1.428e-003   7.38923e-005     1.0e+003     3.972e-004

Maximum Observational Radial Distance Encountered:      3.8 mm

Exterior Orientation Summary (Xc, Yc, Zc are in project units, rotations are in decimal degrees)

Station      Image       Xc           Yc           Zc         Alpha       Elev.        Roll
   1       Image001    416.16627    182.12782 -1315.96373    6.640666   84.505662     8.341025
   2       Image002   -388.86091    -41.84421 -1891.11594  -67.945938   66.826742   -84.060386
   3       Image003    190.82251    -29.93357 -1921.42074  -37.077396   79.656124   -10.897168
   4       Image004    865.44640   -184.51380 -1627.21884   47.140451   67.876489    90.704990
   5       Image005    296.97175    489.87467 -1957.28877 -167.808862   84.754061  -166.343241
   6       Image006   -475.46057    341.32632 -1589.38355  -78.153418   57.822774    83.411757
   7       Image007   1208.24439    231.32320 -1364.82084   69.174176   56.302387   -93.480988
   8       Image008    452.90185    137.78341 -2110.66384   19.590228   80.565262  -159.759496
   9       Image009   -279.11942    183.00914 -1334.40886  -75.258588   59.221504   -84.038457
  10       Image010   1065.03249    184.92520 -1321.55941   76.756222   58.903746    81.771119
  11       Image011   1059.65459   -312.64965 -1372.25937   47.797584   56.896573    68.865445
  12       Image012    480.34962   -233.94367 -1522.34142    5.984933   72.853028     4.525133
  13       Image013   -326.81541   -373.52939 -1276.76009  -50.289505   53.813295   -55.467673
  14       Image014   -377.15092   1134.38920  -915.87877 -137.113880   40.662560  -141.682099
  15       Image015    411.16082   1213.69430 -1049.71410  179.892290   52.095176  -178.678089
  16       Image016   1451.58989   1106.47186  -851.97302  129.627284   35.811222   139.515056
```
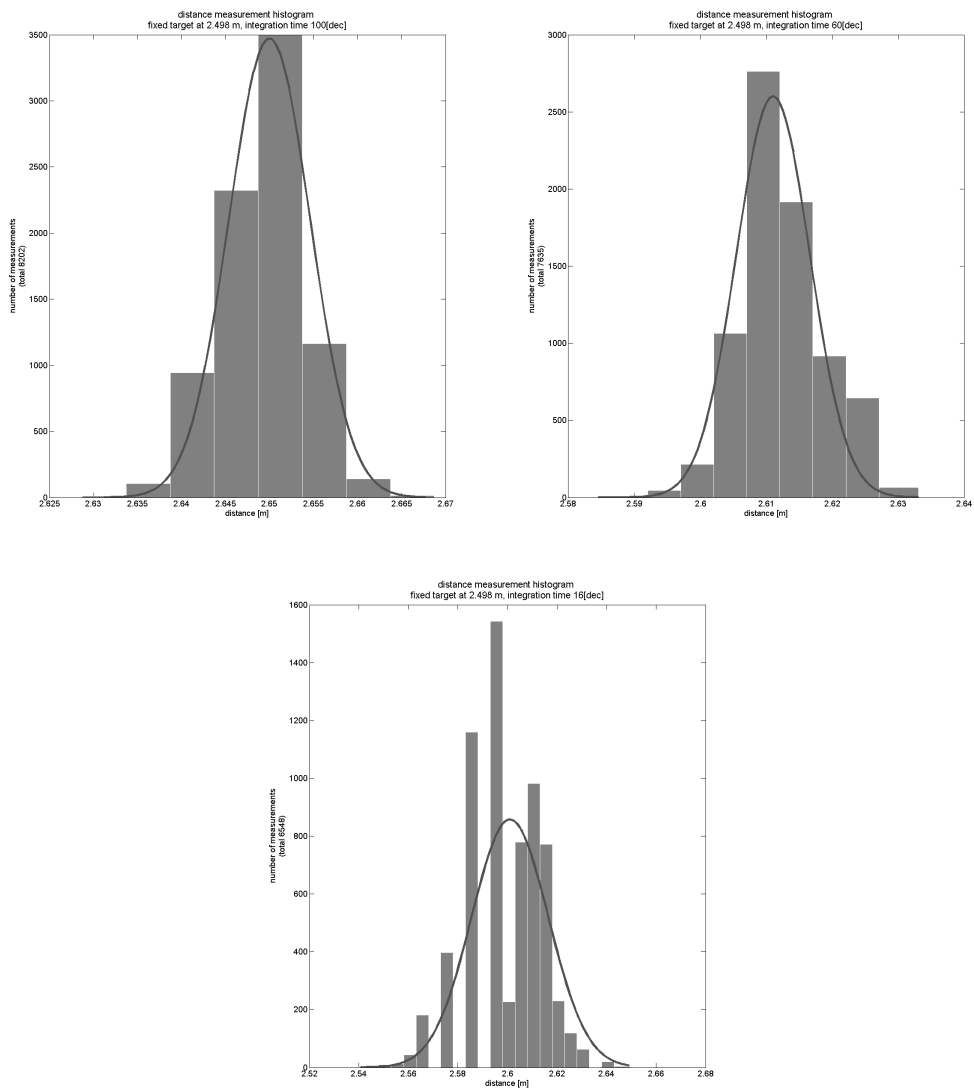
Appendix D

Distance Histograms SR-2 and SR-3000

Figure D.1: *Distance histograms for the SR-2 for different integration times (16, 60, and 100 [dec]).*
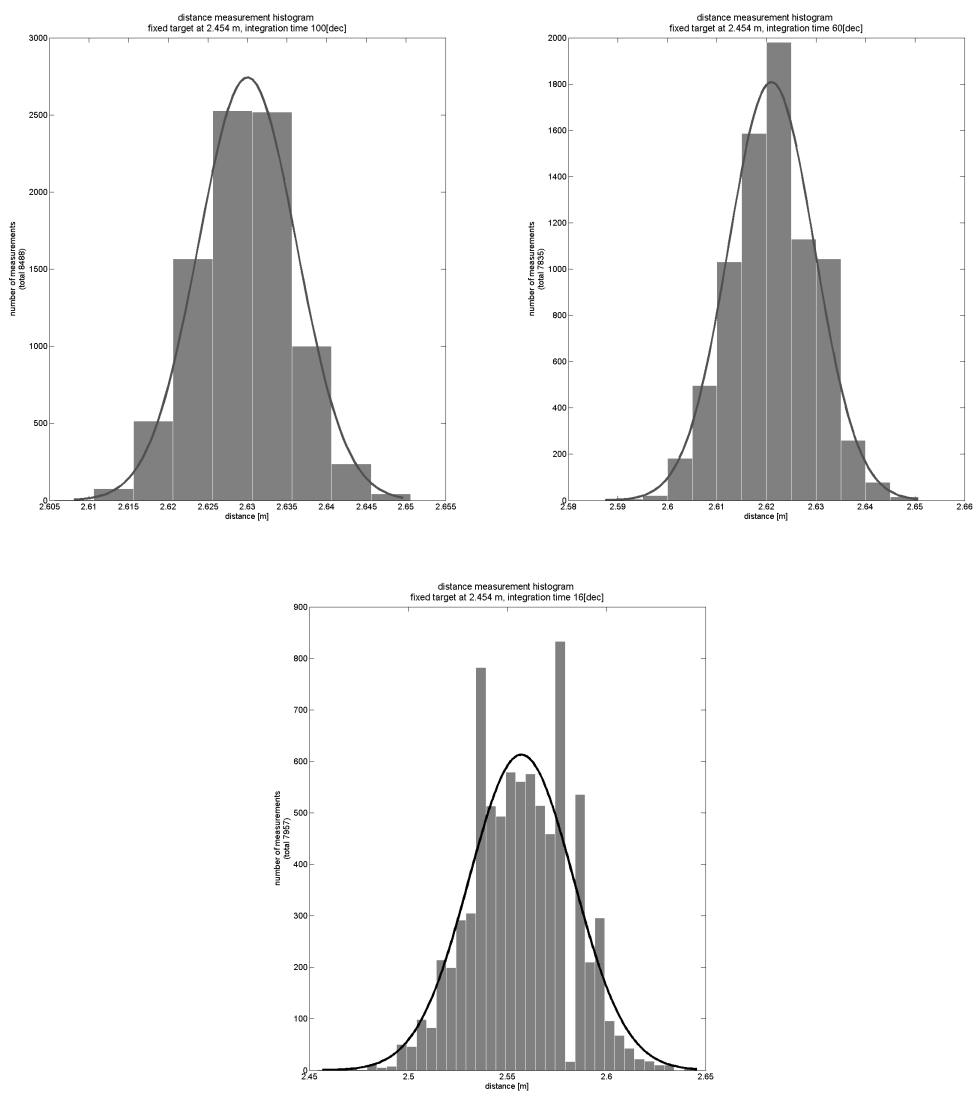
Figure D.2: *Distance histograms for the SR-3000 for different integration times (*16*,* 60*, and* 100 *[dec]).*
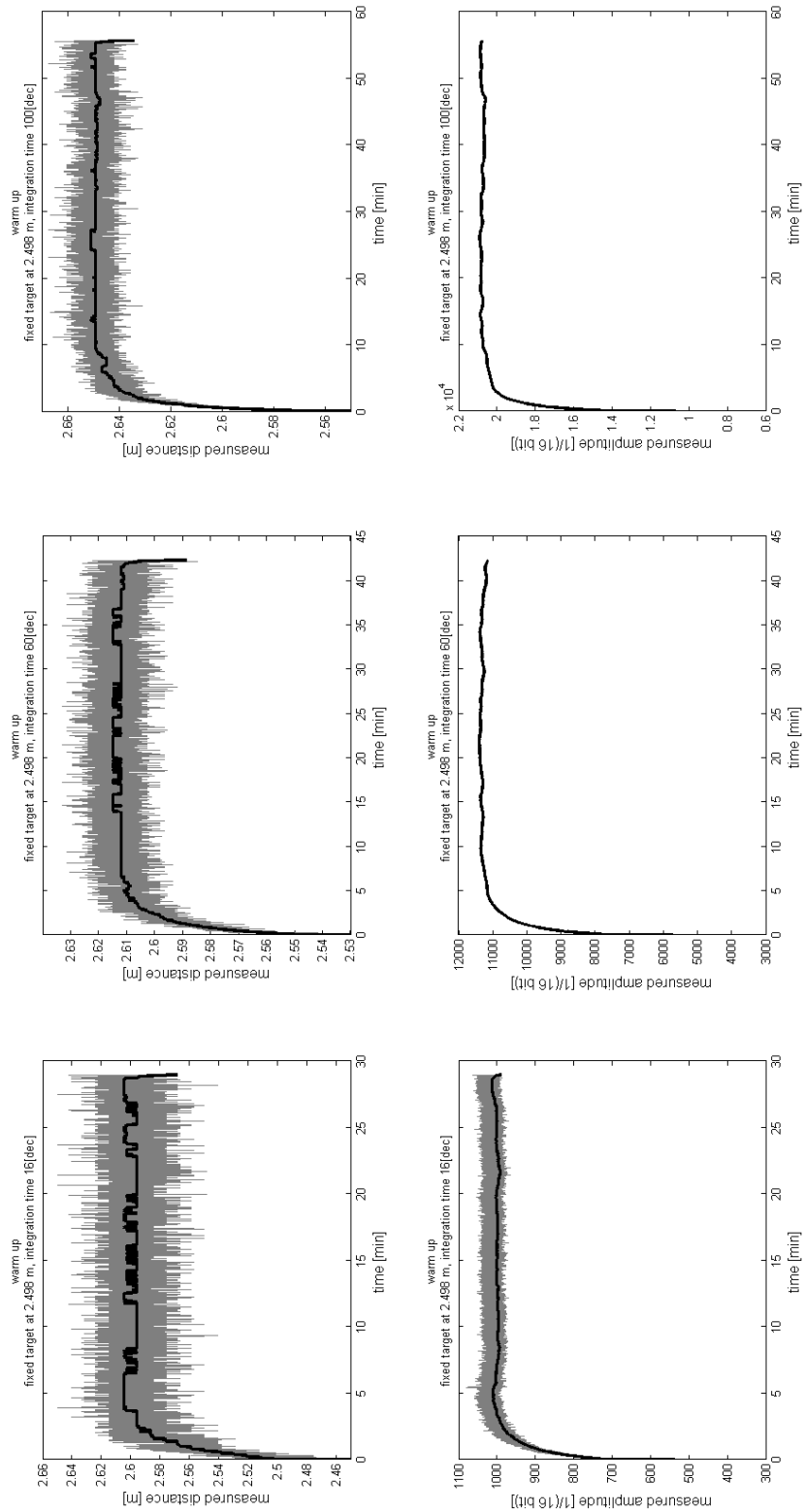
Appendix E

Warmup Sequences SR-2 and SR-3000

Table E.1: *Warm up of the SR-2 RIM camera and the influence on the demodulated distance and amplitude.*
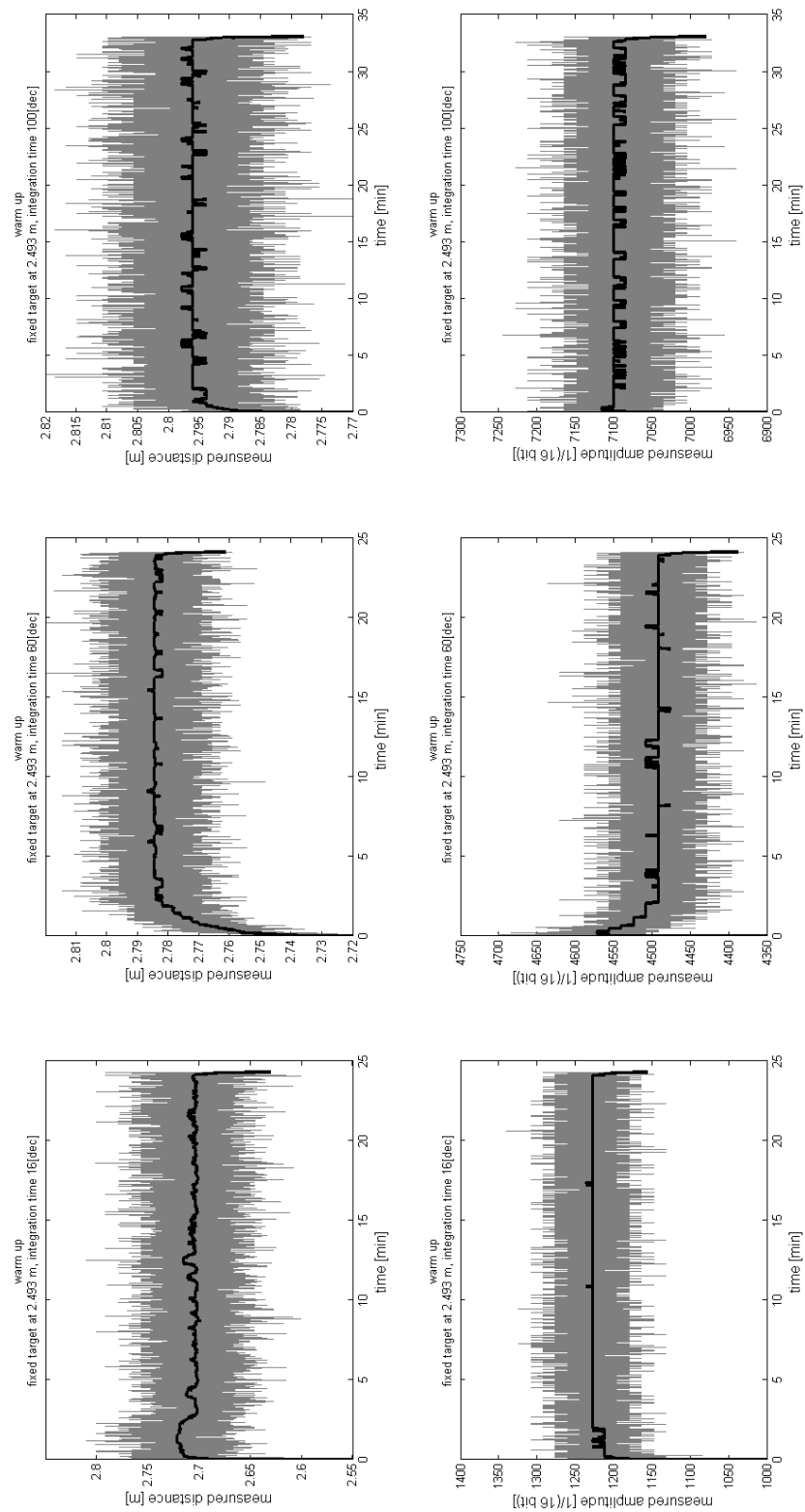
Table E.2: *Warm up of the SR-3000 RIM camera and the influence on the demodulated distance and amplitude.*

Bibliography

Aull, B. F., Loomis, A. H., Young, D. J., Heinrichs, R. M., Felton, B. J., Daniels, P. J. & Landers, D. J. (2002), *Geiger-Mode Avalanche Photodiodes for Three-Dimensional Imaging*, Lincoln Laboratory Journal; Vol. 13, Number 2, pp. 335-350.

Baker, R. J. (2005), *CMOS - Circuit Design, Layout, and Simulation, Second Edition*, IEEE Press Series on Microelectronic Systems, Wiley-Interscience.

Baumann, E. (1998), *Vermessungskunde Band 2*, Ferd. Dümmlers Verlag, ISBN 3-427-79056-8, Bonn, Germany.

Bolsakov, Deumlich, Golubev & Vasilev (1985), *Elektronische Streckenmessung*, Gemeinschaftsauflage VEB Verlag für Bauwesen, Berlin, Germany.

Bosch, T. & Lescure, M. (1995), *Experimental Determination of the Useful Reflection Coefficient of Non-Cooperative Targets for a Time-of-Flight Laser Rangefinder*, published in Optical Review Vol.2, No.4 pp. 289-291.

Brown, D. C. (1971), *Close-range camera calibration*, PE&RS, Vol. 37(8), pp. 855-866.

Büttgen, B., Oggier, T., Kaufmann, R., Seitz, P. & Blanc, N. (2004), *Demonstration of a novel drift field pixel structure for the demodulation of modulated light waves with application in three-dimensional image capture*, SPIE 5302, Three-Dimensional Image Capture and Applications VI, pp. 9–20, Editors: Brian D. Corner and Peng Li and Roy P. Pargas, San Jose, CA, USA.

Büttgen, B., Oggier, T., Lehmann, M., Kaufmann, R. & Lustenberger, F. (2005), *CCD/CMOS Lock-In Pixel for Range Imaging: Challenges, Limitations and State-of-the-Art*, Proceedings of the 1st Range Imaging Research Day at ETH Zurich in Switzerland, Editors: Ingensand, Hilmar and Kahlmann, Timo, ISBN 3-906467-57-0.

Burnside, C. D. (1971), *Electromagnetic distance measurement*, Crosby Lockwoods Staples, ISBN 0-258-96793-5, London, England.

Deumlich, F. & Staiger, R. (2002), *Instrumentenkunde der Vermessungstechnik*, Hertbert Wichmann Verlag, Hüthig, Heidelberg, Germany.

DIN EN ISO 9001:2000 (2000), *Qualitätsmanagementsysteme Anforderungen, trilingual*, DIN Deutsches Institut für Normung, Normensausschuss Qualitätsmanagement, Statistik und Zertifizierungsgrundlagen (NQSZ).

DIN ISO 17123-5:2005 (2005), *Optics and optical instruments – Field procedures for testing geodetic and surveying instruments – Part 5: Electronic tacheometers*, DIN Deutsches Institut für Normung.

Fossum, E. R. (1993), *Active Pixel Sensors: Are CCD's Dinosaurs?*, SPIE Vol. 1900.

Fritzsche, M. (2007), *Einsatz von 3D-Entfernungsbildkameras im Fahrzeug*, Presentation at the PMD[vision] Day – Automotive, Munich, Germany.

Gächter, B. (1996), *Process and Device for the Electro-Optical Measurement of Distance*, United States Patent 5,892,576.

Gächter, S. (2006), *Incremental Object Part Detection with a Range Camera*, Technical Report at ETH Zurich, ETHZ-ASL-2006-12.

Gerthsen, C. & Vogel, H. (1993), *Physik*, Springer-Verlag, Berlin, Germany.

Gruen, A. & Huang, T. S. (2001), *Calibration and Orientation of Cameras in Computer Vision*, Springer-Verlag.

Guillaume, S. (2006), *Identification and Tracking of Moving People in Range Imaging Data*, Seminar Thesis at ETH Zurich, Switzerland.

Gut, O. (2004), *Untersuchungen des 3D-Sensors SwissRanger*, Diploma thesis, ETH Zurich, Switzerland.

Gvili, R., Kaplan, A., Ofek, E. & Yahav, G. (2003), *Depth keying*, SPIE 5006, Stereoscopic Displays and Virtual Reality Systems X, Andrew J. Woods, Mark T. Bolas, John O. Merritt, Stephen A. Benton, Editors, Proceedings of SPIE-IS& T Electronic Imaging.

Hauke, M. & Bömer, T. (2005), *Range imaging and vision based protective devices (VBPDs) A team for safety?*, Proceedings of the 1st Range Imaging Research Day at ETH Zurich in Switzerland, Editors: Ingensand, Hilmar and Kahlmann, Timo, ISBN 3-906467-57-0.

Hebert, M. & Krotkov, E. (1992), *3D Measurements From Imaging Laser Radars: How Good are They?*, Image and Vision Computing, Vol. 10, No. 3, pp. 170–178.

Heinol, H. G. (2001), Untersuchung und Entwicklung von modulationslaufzeitbasierten 3D-Sichtsystemen, PhD thesis, Fachbereich Elektrotechnik und Informatik, University of Siegen.

Hempel, M. (2007), *Validierung der Genauigkeit und des Einsatzpotentials einer distanzmessenden Kamera*, Diploma thesis, Dresden, Germany.

Hennecke, F., Müller, G., Werner, H., Möser, M., Möbius, G., Potthoff, H. & Schulz, H.-U. (1994), *Handbuch Ingenieurvermessung Band 1*, Wichmann Verlag GmbH, ISBN 3-87907-264-7, Heidelberg, Germany.

Hennes, M. & Ingensand, H. (2000), *Komponentenkalibrierung versus Systemkalibrierung*, Proceedings of the XIII. International Course on Engineering Surveying, Munich.

Hinderling, J. (2004), *Distanzmesser, Funktionsprinzipien und Demonstration von EDM*, scriptum Geodätische Sensorik; Institute of Geodesy and Photogrammetry ETH Zurich.

Ingensand, H. (2002), *Einführung in die Geodätische Messtechnik, Band 2*, scriptum ETH Zurich.

Ingensand, H. (2003), *Geodätische Sensorik*, scriptum ETH Zurich.

Intel Corporation (2006), *Open Source Computer Vision Library (OpenCV), http://www.intel.com/technology/computing/opencv/index.htm*.

Isard, M. & Blake, A. (1998), *CONDENSATION – conditional density propagation for visual tracking*, Int. J. Computer Vision, 29, 1, 5-28.

ISO GUM (1995), *Guide to the Expression of Uncertainty in Measurement. ISO, ISBN 92-67-10188-9*, International Organization for Standardization.

ISO VIM (2004), *International vocabulary of basic and gereral terms in metrology (VIM), ISO VIM(DGUIDE 99999), DRAFT*, International Organization for Standardization.

Janesick, J. (2004), *Charge coupled CMOS and hybrid detector arrays*, SPIE Vol. 5167.

Janesick, J. R. (2001), *Scientific Charge-Coupled Devices*, The Society of Photo-Optical Instrumentation Engineers (SPIE), Bellingham, England.

Kahlmann, T. & Ingensand, H. (2006), *Calibration of the fast range imaging camera SwissRanger for use in the surveillance of the environment*, SPIE 6396, Security and Defense, Stockholm, Sweden, Editors: Gary W. Kamerman and David V. Willetts and Ove K. Steinvall.

Kahlmann, T., Remondino, F. & Guillaume, S. (2007), *Range imaging technology: new developments and applications for people identification and tracking*, SPIE 6491, Videometrics IX, San Jose, CA, USA, Editors: J.-Angelo Beraldin and Fabio Remondino and Mark R. Shortis.

Kahlmann, T., Remondino, F. & Ingensand, H. (2006), *Calibration for increased accuracy of the range imaging camera SwissRangerTM*, Proceedings of the ISPRS Commission V Symposium 'Image Engineering and Vision Metrology', Dresden, Germany.

Kahmen, H. (1997), *Vermessungskunde*, Walter de Gruyter, ISBN 3-11-015400-8, Berlin, Germany.

Klein, R. (1993), Ein laseroptisches Entfernungsmeßverfahren mit frequenzvariabler Pseudo-Noise-Modulation, PhD thesis, Institut für Nachrichtenverarbeitung, University of Siegen.

Kohoutek, T. (2006), *Überwachung eines Industrieroboters anhand der Verarbeitung von dreidimensionalen Bilddaten der distanzmessenden Kamera SwissRanger SR-3000*, Diploma thesis, Dresden, Germany.

Koller-Meier, E. (2000), Extending the Condensation Algorithm for Tracking Multiple Object in Range Image Sequences, PhD thesis, ETH Zurich.

Kubacki, J. & Pfeiffer, K. (2005), *Using Range Imaging Sensors with Color Imaging Sensors in Cognitive Robot Companions:a New and Simple Calibration Technique Based on Particle Swarm Optimization*, Proceedings of the 1st Range Imaging Research Day at ETH Zurich in Switzerland, Editors: Ingensand, Hilmar and Kahlmann, Timo, ISBN 3-906467-57-0.

Kutterer, H. & Schön, S. (2004), *Alternativen bei der Modellierung der Unsicherheit beim Messen*, Zeitschrift für das Vermessungswesen (ZfV) 6/2004: pp. 389 - 398.

Lange, R. (2000), 3D Time-of-Flight Distance Measurement with Custom Solid-State Image Sensors in CMOS/CCD-Technology, PhD thesis, Department of Electrical Engeneering and Computer Science at University of Siegen.

Löffler et al., F. (2002), *Handbuch der Ingenieurgeodäsie — Maschinen- und Anlagenbau*, Herbert Wichmann Verlag, ISBN 3-87907-299-X, Heidelberg, Germany.

Lomba, C. R., Valadas, R. T. & de Oliveira Duarte, A. M. (1998), *Experimental characterisation and modelling of the reflection of infrared signals on indoor surfaces*, IEE Proceedings online no. 19982020.

Luhmann, T. (2000), *Nahbereichsphotogrammetrie*, Herbert Wichmann Verlag, Heidelberg, Germany.

Maas, H.-G. (1997), *Mehrbildtechniken in der digitalen Photogrammetrie (Habilitationsschrift)*, Institute of Geodesy and Photogrammetry, ETH Zurich, ISBN 3-9066467-00-7.

Merzinger, G., Mühlbach, G., Wille, D. & Wirth, T. (1996), *Formeln und Hilfen zur Höheren Mathematik*, Binomi Verlag, ISBN 3-923923-35-X, Springe, Germany.

Möller, T., Kraft, H., Frey, J., Albrecht, M. & Lange, R. (2005), *Robust 3D Measurement with PMD Sensors*, Proceedings of the 1st Range Imaging Research Day at ETH Zurich in Switzerland, Editors: Ingensand, Hilmar and Kahlmann, Timo, ISBN 3-906467-57-0.

Mure-Dubois, J. & Hügli, H. (2007), *Optimized scattering compensation for time-of-flight camera*, SPIE 6762-17, Optics East 2007, Boston, MA, USA.

Niclass, C., Besse, P.-A. & Charbon, E. (2005), *Array os Single Photon Avalanche Diodes in CMOS Technology: Picosecond Timing Resolution for Range Imaging*, Proceedings of the 1st Range Imaging Research Day at ETH Zurich in Switzerland, Editors: Ingensand, Hilmar and Kahlmann, Timo, ISBN 3-906467-57-0.

NIST (2001), *NIST Special Publication 330,2001 Edition, The International System of Units (SI), Editor: Taylor, Barry N.*, United States Department of Commerce — National Institute of Standards and Technology (NIST).

Oggier, T., Kaufmann, R., Lehmann, M., Büttgen, B., Neukom, S., Richter, M., Schweizer, M., Metzler, P., Lustenberger, F. & Blanc, N. (2005), *Novel Pixel Architecture with inherent Background Suppression for 3D Time-of-Flight Imaging*, SPIE 5665,Videometrics VIII, San Jose, CA, USA, Editors: Beraldin, J.-Angelo and El-Hakim, Sabry F. and Gruen, Armin and Walton, James S.

Oggier, T., Lehmann, M., Kaufmann, R., Schweizer, M., Richter, M., Metzler, P., Lang, G., Lustenberger, F. & Blanc, N. (2004), *An all-solid-state optical range camera for 3D real-time imaging with sub-centimeter depth resolution (SwissRanger)*, SPIE 5249, Optical Design and Engineering, pp. 534–545, Editors: Laurent Mazuray and Philip J. Rogers and Rolf Wartmann, St. Etienne, France.

Phong, B. T. (1975), *Illumination for Computer Generated Pictures*, Newman, W. (Editor) Association for Computing Machinery.

Rüeger, J. M. (1996), *Electronic Distance Measurement*, Springer-Verlag, Berlin, Germany.

Reimer, M., Wulf, O. & Wagner, B. (2005), *Continuous 360 degree real-time 3D laser scanner*, Proceedings of the 1st Range Imaging Research Day at ETH Zurich in Switzerland, Editors: Ingensand, Hilmar and Kahlmann, Timo, ISBN 3-906467-57-0.

Remondino, F. & Fraser, C. (2006), *Digital Camera Calibration Methods: Considerations and Comparisons*, ISPRS Commission V, WG V/1, Proceedings of the Commission V Symposium: Image Engineering and Vision Metrology, Dresden, Germany.

Rochas, A. (2003), Single Photon Avalanche Diodes in CMOS technology, PhD thesis, EPF-Lausanne.

Saleh, B. E. A. & Teich, M. C. (1991), *Fundamentals of Photonics*, John Wiley and Sons, Inc.

Schulz, T. (2007), Calibration of a Terrestrial Laser Scanner for Engineering Geodesy, PhD thesis, No. 17036, ETH Zurich.

Schwarte, R. (2005*a*), *Personal Notes.*

Schwarte, R. (2005*b*), *Technisches 3D-Sehen auf Basis der PMD-Technologie*, unpublished, Siegen, Germany.

Schwarte, R., Xu, Z., Heinol, H., Olk, J. & Buxbaum, B. (1997), *New optical four-quadrant phase-detector integrated into a photogate array for small and precise 3D-cameras*, SPIE Vol.3023.

Schwarz, W. (1995), *Vermessungsverfahren im Maschinen- und Anlagenbau*, Verlag Konrad Wittwer, Stuttgart.

Seitz, P. (2005), *Unified analysis of the performance of optical range-imaging techniques*, Proceedings of the 1st Range Imaging Research Day at ETH Zurich in Switzerland, Editors: Ingensand, Hilmar and Kahlmann, Timo, ISBN 3-906467-57-0.

Spirig, T. (1997), Smart CCD/CMOS Based Image Sensors with Programmable, Real-time, Temporal and Spatial Convolution for Applications in Machine Vision and Optical Metrology, PhD thesis, ETH Zurich, Switzerland.

Spirig, T., Marley, M. & Seitz, P. (1997), *The Multitap Lock-In CCD with Offset Subtraction*, IEEE Transactions on Electron Devices, Vol. 44, No. 10.

Spirig, T. & Seitz, P. (1996), *Vorrichtung und Verfahren zur Detektion und Modulation eines intensitätsmodulierten Strahlungsfeldes*, Patentschrift Bundesrepublik Deutschland Deutsches Patentamt, Patentinhaber: Leica AG.

Zetsche, H. (1979), *Elektronische Entfernungsmessung*, Vermessungswesen bei Konrad Wittwer, ISBN 3-87919-127-1, Germany.

Zoller + Fröhlich (2007), *Technical Data Imager 5006, Webpage*, http://www.zf-laser.com/Z+F_IMAGER5006_E.pdf, last visited June 04, 2007.

Zywitza, F., Massen, J., Brunn, M., Lang, C. & Görnig, T. (2005), *One-to-Three-dimensional Ranging for Future Automotive Safety Systems*, Proceedings of the 1st Range Imaging Research Day at ETH Zurich in Switzerland, Editors: Ingensand, Hilmar and Kahlmann, Timo, ISBN 3-906467-57-0.

Acknowledgement

This dissertation was carried out at the Institute of Geodesy and Photogrammetry (IGP) of ETH Zurich. I am greatly indebted to all those who contributed to its realization. In particular, I would like to express my sincere thanks to:

Curriculum Vitae

Personal Data

Name	Timo Kahlmann
Date of Birth	May 22, 1977
Nationality	German

Education

1998 - 2003	Study of Geodesy
	University of Hannover, Germany
	Graduation with Diploma in Geodesy ("mit Auszeichnung")
	Diploma Thesis: Untersuchungen zur hochpräzisen Neigungsmessung
	mit elektronischen Pendelsystemen
	Harbert Book Price
1997 - 1998	Study of Physics
	University of Hannover, Germany

Work Experience

2003 - 2007	Research and Teaching Assistant
	Institute of Geodesy and Photogrammetry, ETH Zurich
	Geodetic Metrology and Engineering Geodesy (Prof. Dr. H. Ingensand)
	PhD Thesis:
	Range Imaging Metrology: Investigation, Calibration and Development
2001 - 2003	Student Assistant
	University of Hannover, Germany
	Institut für Erdmessung
	(Prof. Seeber)
1997-1998	Student Employee and Student Apprentice
	ÖbVI Heubner und Rohardt (Hannover, Germany)

Languages

German	native language
English	spoken and written
French	basics
Latin	qualification (small)
Greek	basics
Hebrew	Hebraïcum